2018

Design and Implementation of PV-Firming and Optimization Algorithms For Three-Port Microinverters

Mahmood Alharbi
University of Central Florida

DESIGN AND IMPLEMENTATION OF PV-FIRMING AND OPTIMIZATION ALGORITHMS FOR THREE-PORT MICROINVERTERS

by

MAHMOOD ALI M ALHARBI
B.S. Taibah University, 2010
M.S. University of Colorado Colorado Springs, 2014

A dissertation submitted in partial fulfillment of the requirements
for the degree of Doctor of Philosophy
in the Department of Electrical & Computer Engineering
in the College of Engineering and Computer Science
at the University of Central Florida
Orlando, Florida

Fall Term
2018

Major Professor: Issa Batarseh

ABSTRACT

With the demand increase for electricity, the ever-increasing awareness of environmental issues, coupled with rolling blackouts, the role of renewable energy generation is increasing along with the thirst for electricity and awareness of environmental issues. This dissertation proposes the design and implementation of PV-firming and optimization algorithms for three-port microinverters.

Novel strategies are proposed in Chapters 3 and 4 for harvesting stable solar power in spite of intermittent solar irradiance. PV firming is implemented using a panel-level three-port grid-tied PV microinverter system instead of the traditional high-power energy storage and management system at the utility scale. The microinverter system consists of a flyback converter and an H-bridge inverter/rectifier, with a battery connected to the DC-link. The key to these strategies lies in using static and dynamic algorithms to generate a smooth PV reference power. The outcomes are applied to various control methods to charge/discharge the battery so that a stable power generation profile is obtained. In addition, frequency-based optimization for the inverter stage is presented.

One of the design parameters of grid-tied single-phase H-bridge sinusoidal pulse-width modulation (SPWM) microinverters is switching frequency. The selection of the switching frequency is a tradeoff between improving the power quality by reducing the total harmonic distortion (THD), and improving the efficiency by reducing the switching loss. In Chapter 5, two algorithms are proposed for optimizing both the power quality and the efficiency of the microinverter. They do

this by using a frequency tracking technique that requires no hardware modification. The first algorithm tracks the optimal switching frequency for maximum efficiency at a given THD value. The second maximizes the power quality of the H-bridge micro-inverter by tracking the switching frequency that corresponds to the minimum THD.

Real-time PV intermittency and usable capacity data were evaluated and then further analyzed in MATLAB/SIMULINK to validate the PV firming control. The proposed PV firming and optimization algorithms were experimentally verified, and the results evaluated. Finally, Chapter 6 provides a summary of key conclusions and future work to optimize the presented topology and algorithms.

To My Parents

Safiah & Ali

ACKNOWLEDGMENT

I would like to express my sincere gratitude and appreciation to the government of the Kingdom of Saudi Arabia, Ministry of Education in Saudi Arabia, and Taibah University for their financial support and continuous motivation to my study for the PhD at the University of Central Florida. They have provided all means to create an appropriate learning environment.

I would like to express my sincere appreciation and gratitude to Professor Issa Batarseh, my academic advisor, for his patient guidance, enthusiastic encouragement and useful critiques of this research work throughout my studies and research at University of Central Florida. His guidance helped me in all the time of research and writing of this dissertation. Beside his support and immense knowledge, he has always given me great chances to pursuit my work independently.

Besides my advisor, I would like to thank the rest of my thesis committee: Dr. Nasser Kutkut, Dr. Wasfy B. Mikhael, Dr. Michael Haralambous and Dr. Jiann S. Yuan, for their insightful comments and encouragement.

I would like to thank the team members in the Florida Power Electronics Center (FPEC), and special thanks to Dr. Haibing Hu, Siddhesh Shinde, and Anirudh Pise for their invaluable support and time spent on my research.

I would like to thank the team members in the Florida Solar Energy Center (FSEC) for providing me with invaluable real-time data for the PV intermittency.

I would like to thank the team members in the Advanced Power Electronics Corporation (ApECOR), and special thanks to Chris Hamilton and Michael Pepper for helping me performing the algorithms coding.

I would like to thank the team members in the Advanced Charging Technology (ACT) Engineering Center in Orlando, FL, and special thanks to Dr. Nasser Kutkut and Charles Jourdan for helping me constructing the hardware.

I would like to express my appreciation to Dr. Ala Hussein from Yarmouk University for his guidance and support.

Finally, I would like to thank my parents, Safiah and Ali, and my wife Razan Alahmadi, for supporting me spiritually throughout my study and my life in general.

TABLE OF CONTENTS

LIST OF FIGURES

LIST OF TABLES

CHAPTER 1: INTRODUCTION

1.1 Background

1.1.1 The Nature of PV Energy

The nature of the photovoltaic (PV) energy is based on two factors; the nature of the sunlight (irradiance) and temperature. These two factors depend on the location on the earth. For example, the concentrating solar power resource potential for the United States changes in each state as shown in Figure 1, [1]. In Colorado for instance, the annual average solar resource changes from about 4.5 to 6.5 kWh/m^2/Day. Additionally, due to weather changes such as cloud passing, the PVs deliver power intermittently although the ideal shape of the PV output power is a parabolic curve. Figure 2 illustrates an example of the actual PV power and the ideal PV power measured for one-minute time resolution. The x-axis in the figure represents the time in minutes, where it begins from minute 1 (at midnight, 00:00) to minute 1440 (just before midnight, 23:59). The y-axis represents the power in watt (W), where the maximum power delivered by the PV is about 600W. The fluctuations shown in the actual PV power indicates the times of cloud passing. Similarly, this variation occurs every day. Figure 3 shows an example of the PV out power variations throughout the month of April 2016. These curves are based on real-time data collected for PV intermittency from two 300W PV modular systems including PV panels and a grid-tied microinverter located in a specific region in East Florida [2]. More information about the data

collected is given in Appendix A and B. Moreover, the average, maximum, and minimum PV capacities (Wh) change every month as shown in Figure 4. That concludes that this instability supports the need for energy storage which is the only facility that we can use for this challenge.

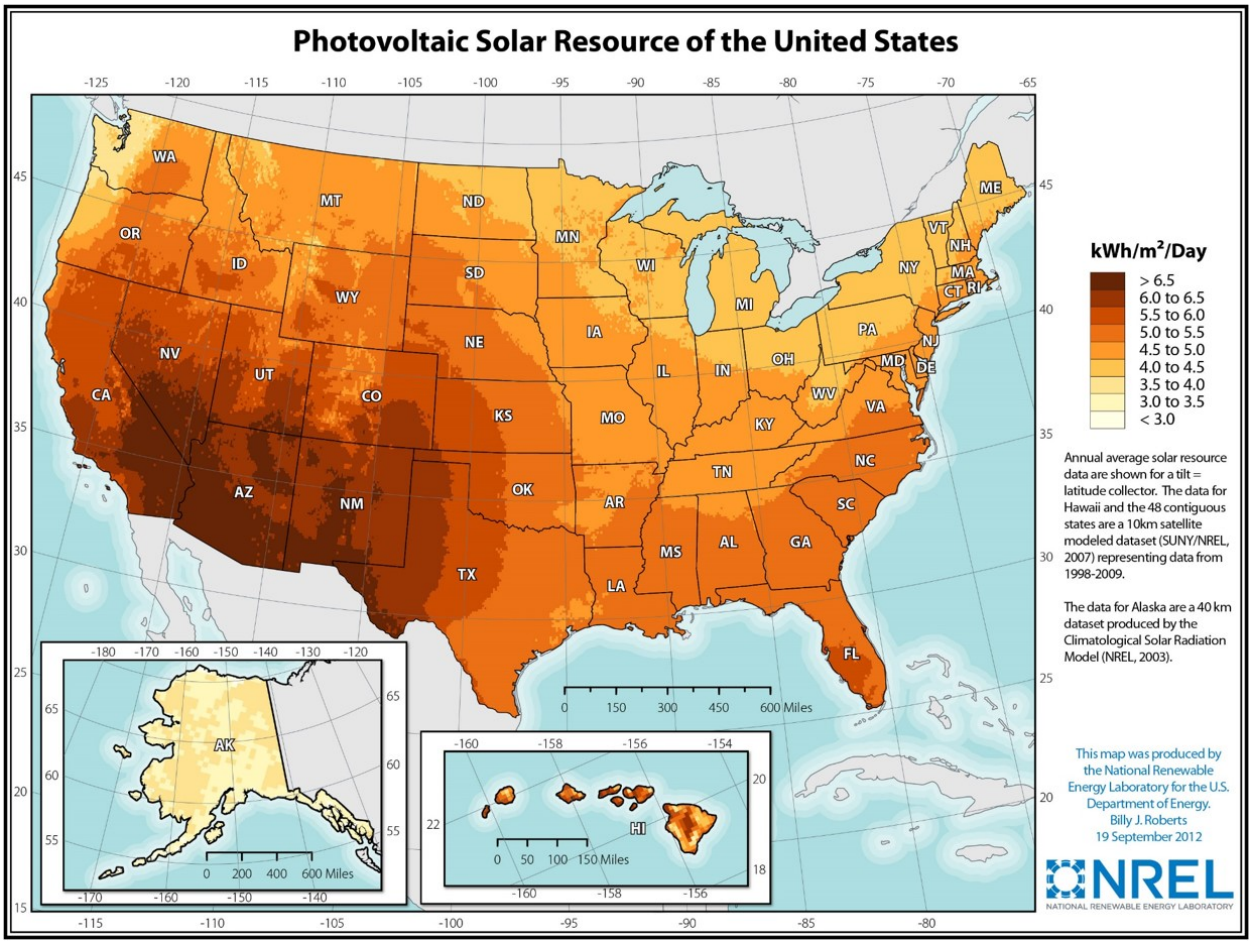

Figure 1: Map of photovoltaics and concentrating solar power source potential for the United States[1].

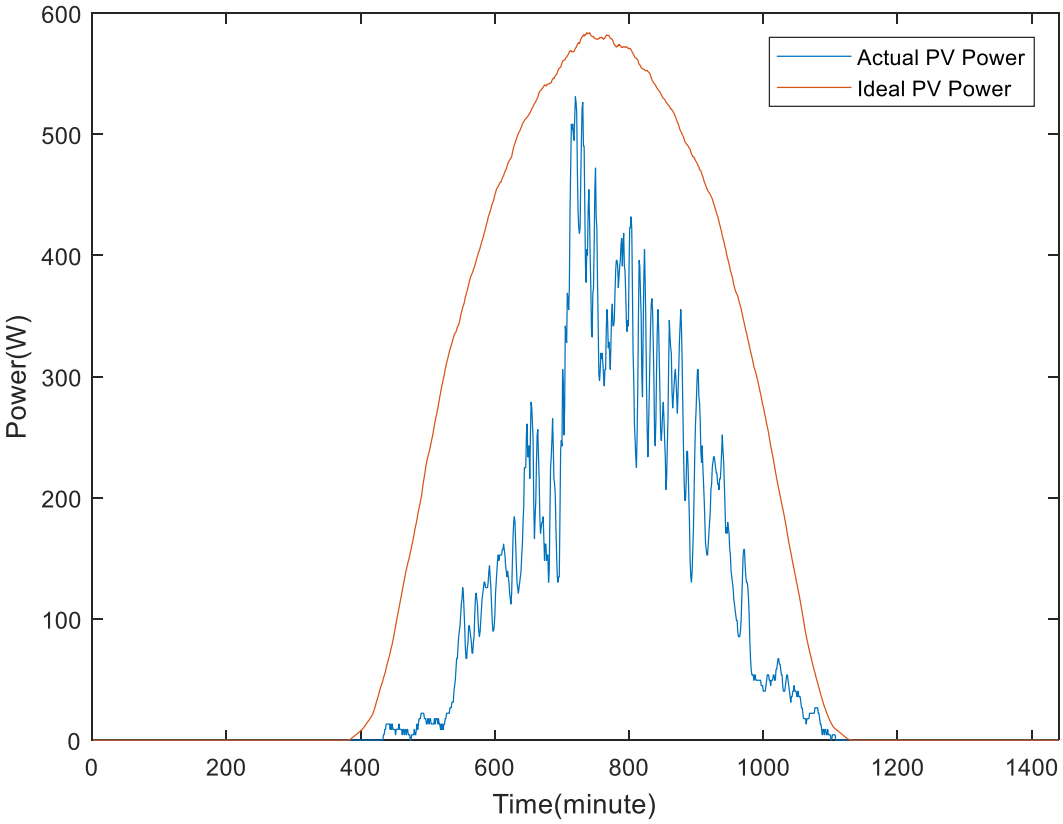

Figure 2: Actual and ideal PV power.

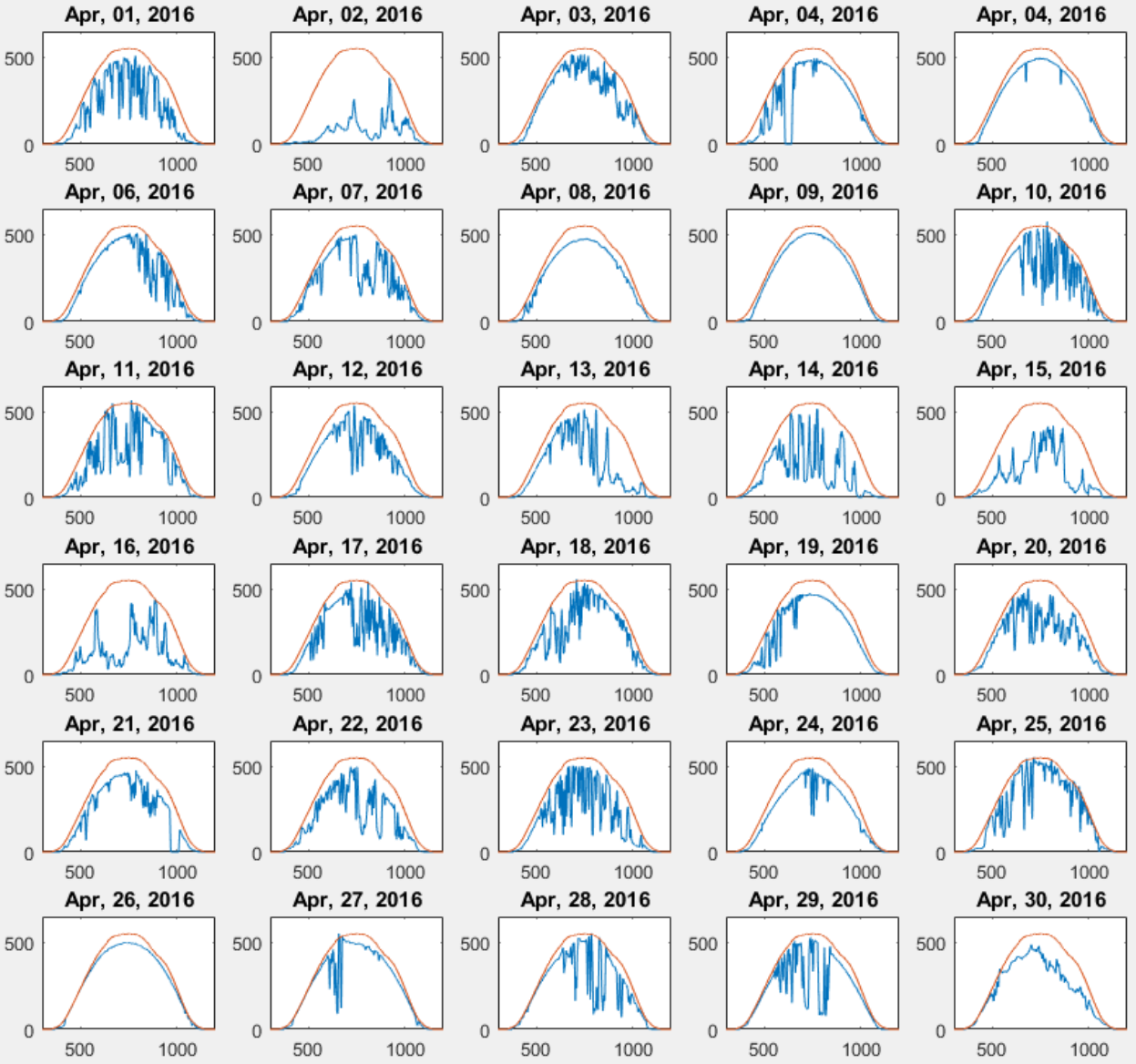

Figure 3: Measured PV power profiles (blue curves) for each day in April 2016 (x-axis: Time (minute), y-axis: Powe (Watt)).

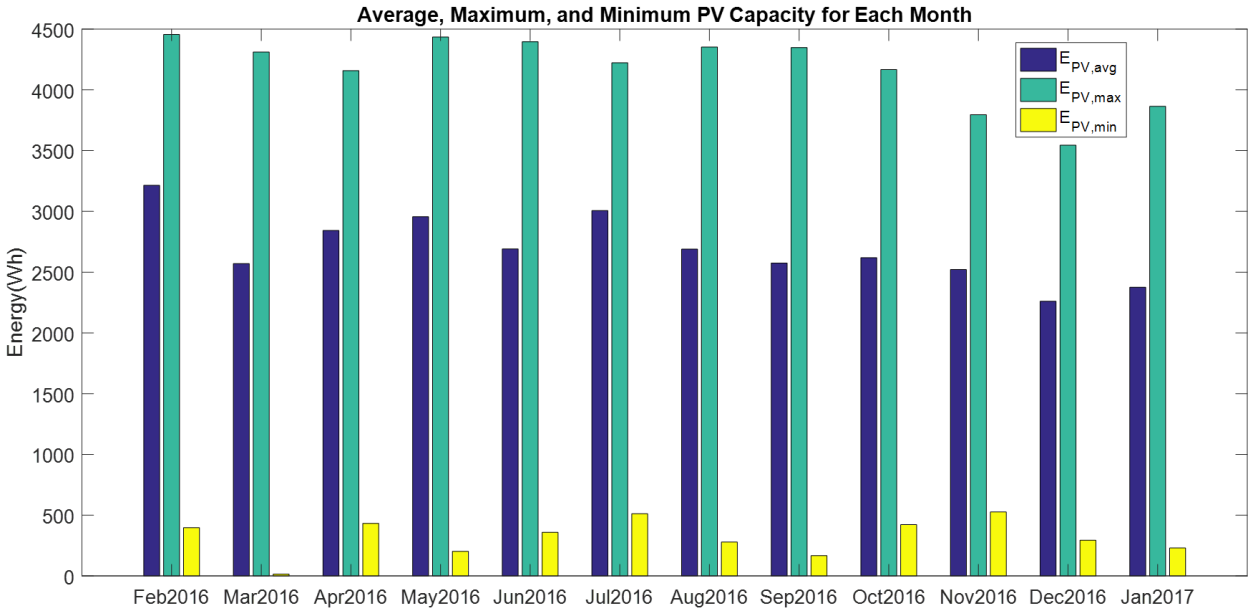

Figure 4: Average, maximum, and minimum PV capacity in Watt-hour based on real-time data in East Florida (Appendix A).

1.1.2 Weather Instability Effects on PV Power

Solar PV power generation is highly unstable due to the irregular changes in the sun irradiance level caused by weather changes and passing clouds. In large utility and auxiliary fuel power generators, the time response can be as long as tens of seconds or more. This is insufficient to compensate for those renewable sources with high variability such as the PV. Cloud passing effects on the PV have been studied for a long time [3], [4], [5], [6], [7]. Some studies address this problem as a contemporaneous issue [8] [9], and focus on the high penetration level of PV generation. Several undesirable effects of the PV variability are voltage fluctuations at the distribution system

level, and frequency instability in small grids. The voltage fluctuations can lead to voltage flicker and excessive Load Tap Changer (LTC) operation. In small grids, the frequency instability can lead to increased damage to conventional voltage regulator equipment. These effects provide more challenges to higher penetration of PV in general and at the distribution levels particularly. Figure 5 summarizes these effects in flowchart.

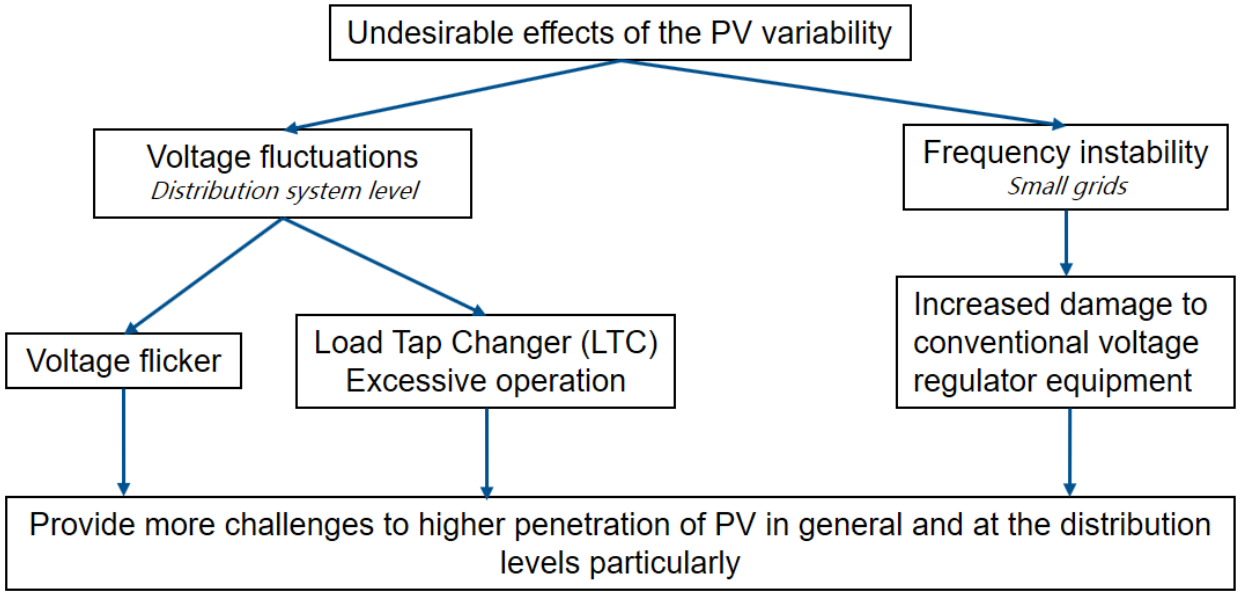

Figure 5: Summery for undesirable effects of the PV variability.

1.1.3 Ramp-Rate and Ramping Frequency of PV Output

Due to the weather instability, the PV output power has considerable changes in magnitude with variable change rates. That instability is called fluctuation with certain ramp-rate and ramping frequency.

The ramp-rate of PV output can be defined as the absolute value of the change rate (increase/decrease) in the PV output power for different time scales as given in (1). The ramping frequency can be defined as the occurrence frequency of the ramp-rate in certain time scale.

$$RampRate = \left|\frac{\Delta P_{PV}}{\Delta t}\right| = \left|\frac{P_{PV}(t) - P_{PV}(t-\Delta t)}{\Delta \mathrm{t}}\right| \quad (1)$$

where;

- ΔP_{PV}: PV output power change (a certain value compared to the rated power
- Δt: change of scaled time

Figure 6 shows the ramping frequencies in the PV output power for two different days in April 2016 in according to real time data in East Florida (Appendix A). On April 1st, 2016, the weather was partly cloudy, where it was overclouded day on April 2nd, 2016. For the partly cloudy day, the ramping frequency of 60W/1min.ramp-rate (10% of 600W rated power) is 27.29% of the total daytime (6:30 AM to 7:00 PM). For same day, the ramping frequency becomes 3% of the total daytime if the ramp-rate is 60W/10min. On the April 2nd, the ramping frequencies for different time scales are much less compared to the April 1st although it was overclouded day.

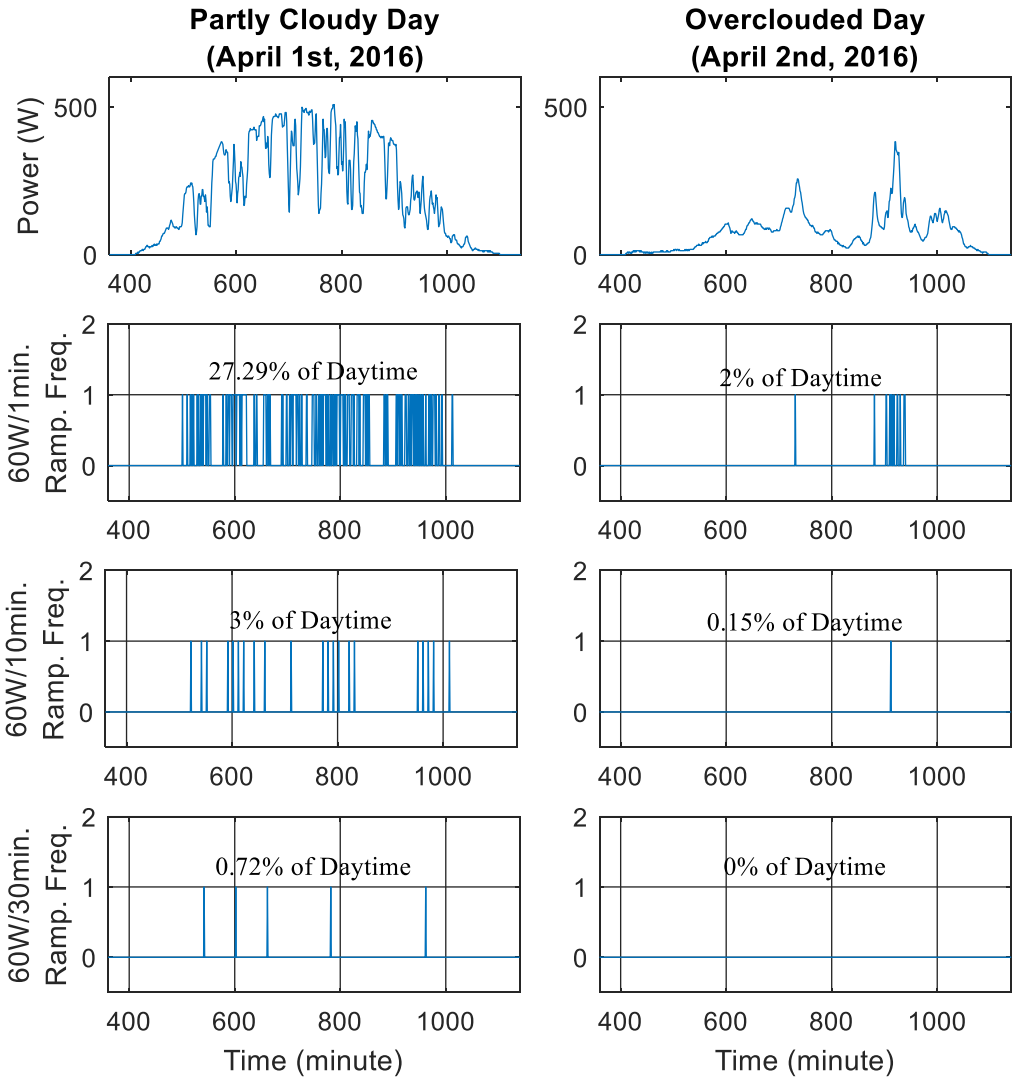

Figure 6: Ramping frequency 60W (10% nominal power) in different time scales for two different days.

Figure 7 shows the daily time (in minute) of ramp-rate higher than 10%/min. of 600W rated PV output power in April 2016. Noticeably, the time of over limited ramp-rate varies from 0 minute up to more than 3 hours. Also, this variability can be explained by analyzing the average daily ramp-rate higher than the limit, where the limit here is considered to be 10%/min of the 600W rated PV output power. This average can be determined for the whole year. Figure 8 shows the average daily high ramp-rate (more than 10%/min.) for each month from February 2016 to January 2017 according to same data collected by [2] (Appendix A).

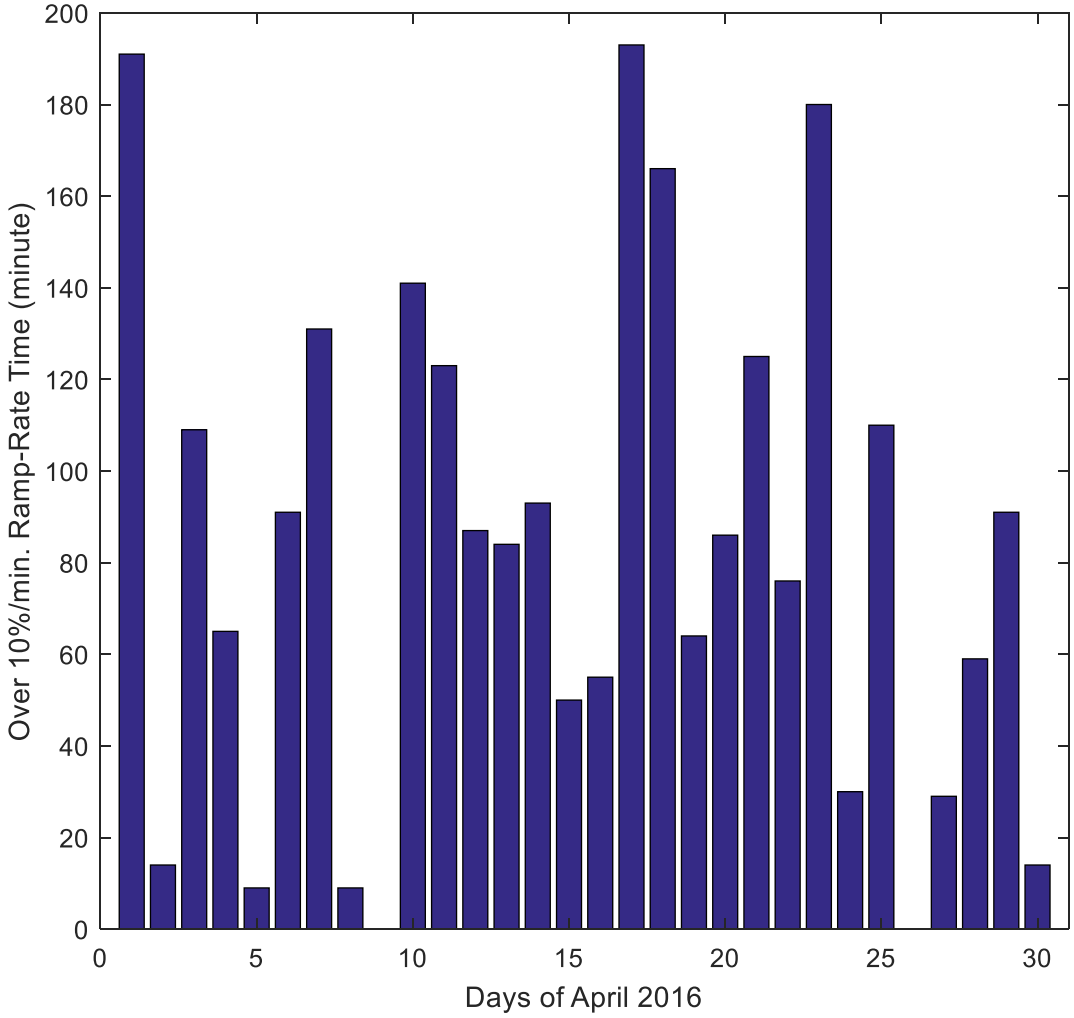

Figure 7: Time of ramp-rate higher than 10%/min. of the rated PV power (600W) for each day in April 2016.

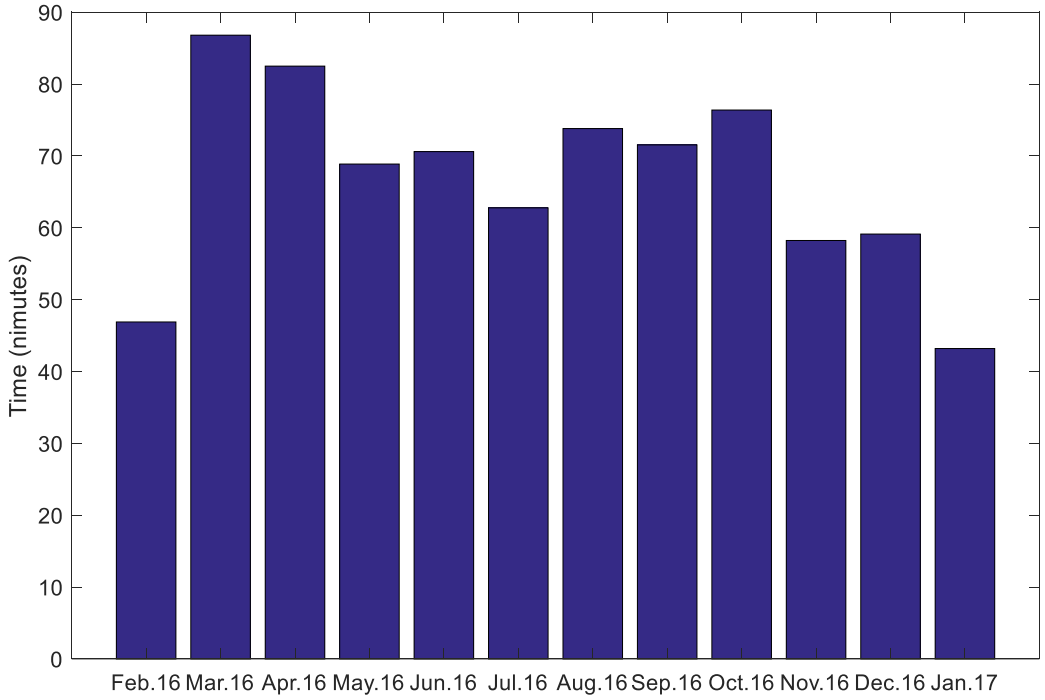

Figure 8: Average daily ramp-rate higher than 10%/min. of 600W rated PV output power for each month from Feb. 2016 to Jan. 2017.

Here, more real examples of fluctuation ramp-rates due to the cloud passing are presented. In [10], an operating experience of a PV plant system in La Ola Island resulted that the PV penetration is limited to 50% of the nominal AC output rating. This limitation was established to avoid negative impacts to the grid voltage and frequency due to the PV high output fluctuations in power. It was observed that the fluctuation ramp-rate of the PV output was above 30% of the rated capacity/minute, and reached as high as 60%. According to online data collected by National

Renewable Energy Lab (NREL) [11] from Oahu Island, the irradiance fluctuations can have more than 50% ramp-rate in two consecutive measurements. In a study presented in Mesa del Sol, New Mexico [12], PV output was found to ramp up more that ±30% of normal operating power by rated capacity per second. A technical report presented by the Commonwealth Scientific and Industrial Research Organization (CSIRO) [13] in Newcastle, Australia has shown that over 31% ramp-rate of the plant rating can occurs up to 120 time in 10 seconds. These and other documented examples demonstrate that the high ramp-rate fluctuations of the PV output can produce considerable voltage variations that need to be managed [14].

PV-firming strategies and algorithms that control ramp-rate to reduce fluctuations in PV outputs are necessary to increase the PV penetration level in networks. Energy storage is the most practical tool to be used to achieve this goal. Since all energy storage devices absorb and deliver DC power, they rely on power electronics systems, like any renewable energy sources, for interfacing with the AC grid. So, novel approaches and algorithms for a PV-firming system integrating an energy storage as a third port is presented in this dissertation.

1.1.4 Energy Storage Technology

Solar and wind are two different sources of renewable energy that delivers high intermittent powers. Generally, these renewables energies are unreliable and often applied concurrently with electrical energy storage systems to enhance their reliability in the network [15]. This enhancement

is by reducing the power fluctuations, improving the power quality, and enhancing the system flexibility.

There are four categories of energy storage technologies mostly used in electric power systems: chemical, electrochemical, electromagnetic, and mechanical [16], [17], [18], [19], [20]. Each technology has distinctive specifications in terms of different characteristics that are taken into account for comparison. These characteristics are energy density, power capacity, discharge time, life and cycling time, response time, and discharge efficiency.

1.1.4.1 Chemical Energy Storage

There are two types of chemical energy storage technology: synthetic natural gas (SNG) energy storage and hydrogen (H_2) energy storage [21]. For the H_2 energy storage technology, H_2 is extracted from the water (H_2O) by decomposition process with electricity. Then, it is stored in high-pressure tanks and delivered to a fuel cell for ionizing and producing electricity. The main advantage of this technology is its capability of long period storage [22]. However, the main drawback is its high cost due to the expense of producing the H_2 and manufacturing the fuel cells. For the other technology of SNG energy storage, the pressure of the SNG tank is lower than the H_2 tank since the SNG has higher density. However, its conversion losses are higher than H_2's [21].

1.1.4.2 Electrochemical Energy Storage

The most common definition for the electrochemical energy storage is battery. There are three main types of battery: lead acid (LA), lithium ion (Li-ion), and vanadium redox battery (VRB). The LA battery is a traditional battery that is widely applied in several applications because of its low costs. However, it has limited life and cycling times, low energy density, and low efficiency [19]. One the contrary, the Li-ion battery has higher life and cycling times, higher energy density, and higher efficiency [17]. As a disadvantage of the Li-ion battery, its cost is still high comparing to the LA battery. The VRB has also high life and cycling times, but its efficiency decreases in the cold temperature.

1.1.4.3 Electromagnetic Energy Storage

In this technology, the energy is stored in either electric fields (supercapacitor (SC) energy storage device) or magnetic fields (superinducting magnetic energy storage (SMES)) [23], [24]. Both technologies have very low energy density that makes them unsuitable for long discharging time applications.

1.1.4.4 Mechanical Energy Storage

When there is surplus power during off-peak time, the electricity is transferred mechanically to a mechanical storage system. The energy can be stored for long time, and it is released once needed.

The energy is stored in the form of gravitational potential energy (pumped hydroelectric energy storage (PHES)), intermolecular potential energy (compressed air energy storage (CAES)), or rotational energy (flywheel energy storage (FES)) [25], [26]. PHES and CAES technologies have very high power capacity cycling times. However, their response time is slow comparatively.

Table 1 summarizes comparison of the energy storage technologies in terms of energy density, power capacity, discharge time, life time, cycling time, response time, and discharge efficiency [16], [17], [18], [19], [20], [23], [24], [25], [26], [22], [21], [27].

Table 1: Technical Characteristics for Different Energy Storage Technologies

		Energy Density (Wh/L)	Power Capacity (W)	Discharge Time	Life Time (years)	Cycling Time (cycles)	Response Time	Discharge Efficiency (%)
Chemical	**SNG**	*800 – 5000*	*1M – 100 M*	*hours*	*15*	*~20000*	*seconds*	*~50*
	H2	*500 – 3000*	*450k – 45M*	*hours*	*15*	*~10000*	*seconds*	*~59*
Electrochemical	**LA**	*50 – 90*	*1k – 10M*	*minutes*	*3*	*~1000*	*milliseconds*	*~85*
	Li-ion	*200 – 500*	*1k – 70k*	*minutes*	*5 – 10*	*~5000*	*milliseconds*	*~85*
	VRB	*12 – 22*	*450k – 45M*	*hours*	*5 – 15*	*~10000*	*milliseconds*	*~85*
Electromagnetic	**SC**	*10 – 30*	*10k – 400k*	*seconds*	*10 – 30*	*~50000*	*milliseconds*	*~95*
	SMES	*1 – 7*	*1M – 10M*	*seconds*	*>20*	*~100000*	*milliseconds*	*~95*
Mechanical	**PHES**	*1 – 2*	*250M – 950M*	*hours*	*40 – 60*	*~30000*	*minutes*	*~87*
	CAES	*2 – 5*	*100M – 980M*	*hours*	*20 – 40*	*~10000*	*minutes*	*~75*
	FES	*20 – 80*	*1k – 75k*	*minutes*	*15*	*~20000*	*seconds*	*~90*

1.1.5 Integration of PV and Energy Storage

Many researches have proposed different power electronics topologies for integrating PV and energy storage systems. Each topology must be under one of main four architectures as shown in Figure 9, where the energy storage is considered as a battery and the power flow described by blue arrows. Since all architectures are grid-tied, it must have at least one inversion (DC/AC) stage. In the first architecture shown in Figure 9 (a), both PV and battery are connected throughout a separate DC/DC stage to the DC side of the DC/AC stage. Second architecture shown in Figure 9 (b) connects the battery to the AC side through another DC/AC stage. Third architecture shown in Figure 9 (c) integrates both PV and battery throughout a three-port DC/DC converter, where the third port is connected to the DC side of the DC/AC stage. Last architecture shown in Figure 9 (d) eliminates one DC/DC stage by connecting the battery to the DC-link directly.

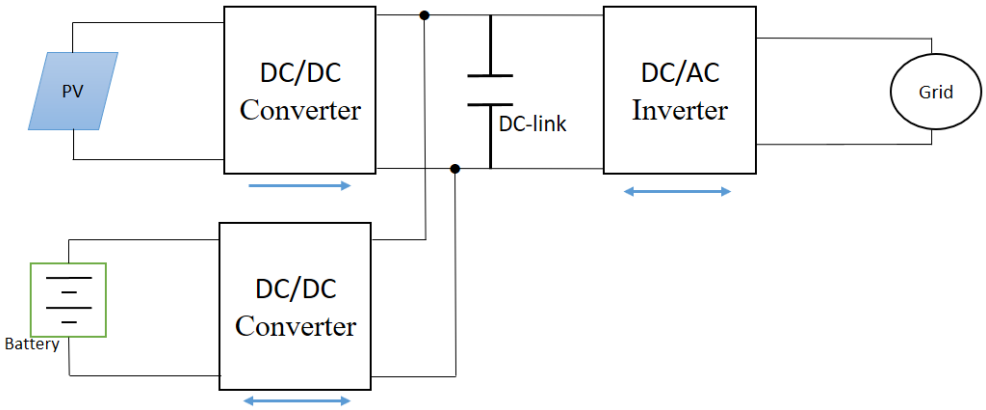
PV
DC/DC
Converter
DC-link
DC/AC
Inverter
Grid
Battery
DC/DC
Converter

(a)

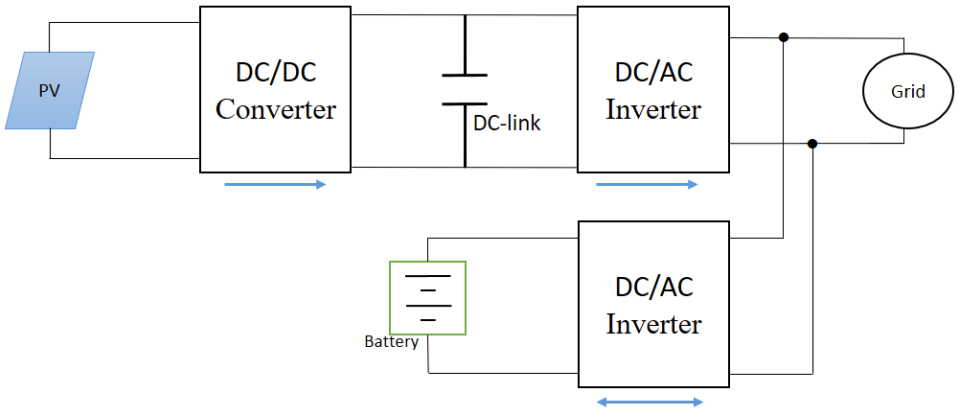
PV
DC/DC
Converter
DC-link
DC/AC
Inverter
Grid
Battery
DC/AC
Inverter

(b)

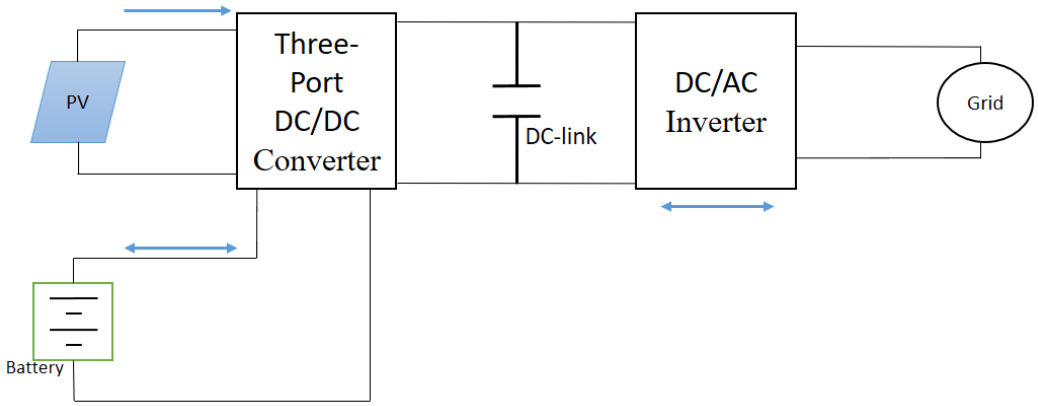

(c)

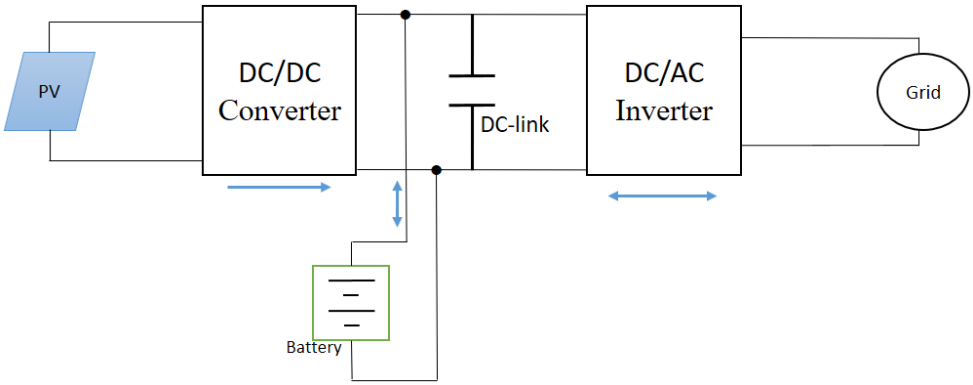

(d)

Figure 9: Architectures of PV and energy storage integration; (a) DC-side battery connection via DC/DC stage, (b) AC-side battery connection via DC/AC stage, (c) PV-battery integrated three-port DC/DC converter, and (d) DC-link battery direct connection.

1.2 Research Motivation and Objective

In recent decades, several researches have paid more attention considerably on the renewable energy worldwide, where electricity generation by photovoltaic (PV) is becoming one of the most common clean and abundance energy sources. Although PV is becoming increasingly cost effective, there are several technical challenges which limit its penetration into the grid. Distributed energy storage seems to hold the key in unlocking the full potential of the renewable energy resources. Recent studies have focused on battery storage at both utility and distributed scale. Many advantages (e.g. energy arbitrage, increased PV self-consumption, transmission congestion relief, VAR support etc.) of such storage across various players ranging from independent system operators to end users are extensively reported in [28],[29],[30],[31],[32],[33], and [34]. As PV penetration increases rapidly while distributed battery systems are expected to become ubiquitous with falling prices [35], incentives lie in integrating batteries, PV panel and advanced power electronics that may provide stable power profiles, and reduced system infrastructure complexity. So, the objectives of this dissertation are to develop an integration of PV, battery, and power electronics in one modular level system with the capability of PV-firming and energy management.

More specifically, the development targets for the integrated system are summarized as follows:

- ✓ To make an integration of PV, battery, and grid in one modular micro-system
- ✓ To minimize the number of conversion stages
- ✓ To employ the capability bidirectional power flow
- ✓ To implement smart functions such as: Grid support, maximum power tracking (MPPT) for the PV

- ✓ To firm the PV output profile to increase its penetration level in the networks

With the above development targets, the research objectives of this dissertation can be summarized as follows:

- ✓ To design and implement a smart integration of the battery into the grid-tied power electronics without additional conversion stage
- ✓ To design and implement all different control methods that can be implemented fully using the digital control, which increase both the power density and reliability and decrease the cost of the micro-system
- ✓ To design and implement a control method that is used for battery charging and discharging
- ✓ To design and implement new algorithms that are used for firming the PV output profile
- ✓ To design and implement new algorithms that are used for optimizing both efficiency and output power quality for the inversion stage of the micro-system

CHAPTER 2: LITERATURE REVIEW

2.1 PV Firming Technologies

Several types of technologies based on energy storage have been proposed for firming the PV output power. Different kinds of storages have been used, such as: battery energy storage [36],[37]; fuel cell energy [38]; superconductive magnetic energy storage [39]; and electric double-layer capacitor (EDLC) [40], [41].

Figure 10 shows , a high-power level system of grid-tied PV firming [36]. This system uses a valve regulated lead-acid (VRLA) battery temporarily to charge and discharge as required for firming the inverter output power. A moving average calculation was used to control the inverter output power by averaging the solar irradiance over the previous one-hour time interval. A similar control method was used in [40]. Here an EDLC is connected in parallel to the DC-link between the DC-DC converter stage and the DC-AC inverter stage as shown in Figure 11.

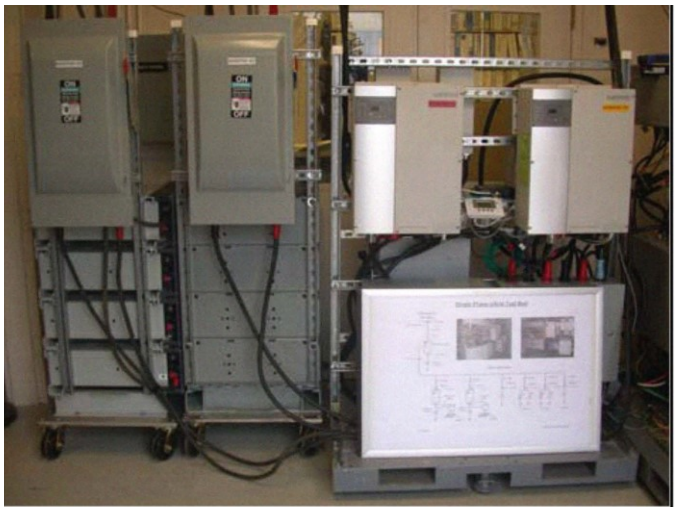

Figure 10: Grid-tied PV firming system[36].

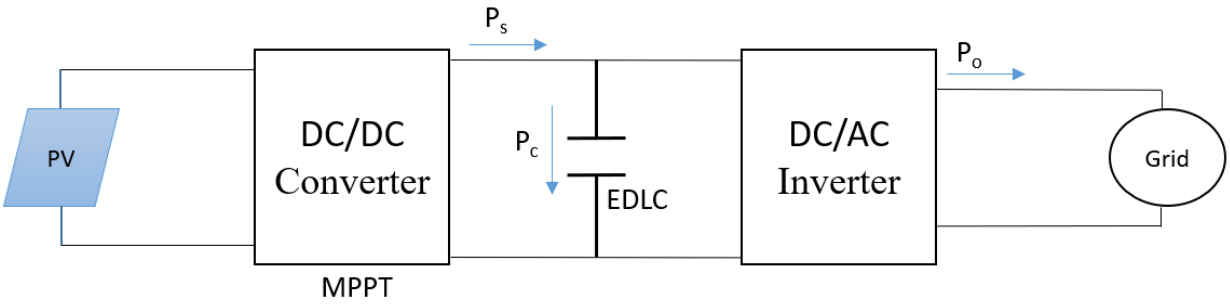

Figure 11: PV-EDLC system for controlling the PV output ramp-rate [40].

Another method to smooth the PV output power is by using a battery energy storage system (BESS) as in [42]. Here a large-scale BESS system was interfacing with PV and wind power

systems through the grid. The firming control was based on storage capacity, where the charging/ discharging scenarios were according to the state of charge (SOC) of the batteries.

PV fluctuation ramp-rate can be assumed as rapid changings with different values of slope. These changes can be compensated for to maintain a minimum value of slope as in [43]. An energy storage has been deployed in this research. Although the control strategy was independent on the previous PV intermittency history like the traditional moving average method, the calculation of the slope that is based on the differentiation of the PV power over time makes delaying to the results practically.

In [44] and [45], a medium voltage scale of BESS is used for PV capacity firming and shifting. The algorithm for firming was based on the maximum and minimum power reference for the PV output. Two bidirectional conversion systems were connected to the BESS for charging and discharging through the grid.

Plug-in hybrid electric vehicle (PHEV) batteries have been utilized in [37] to mitigate the solar irradiance intermittency at short time scales. Here a bidirectional DC-DC (buck-boost) charger is integrated in the PV system as shown in Figure 12, where the communication point was the DC-link. A high-pass filter was used for fluctuation mitigation. The corner frequency (filter characteristic), was used to limit the ramp-rate of the PV inverter.

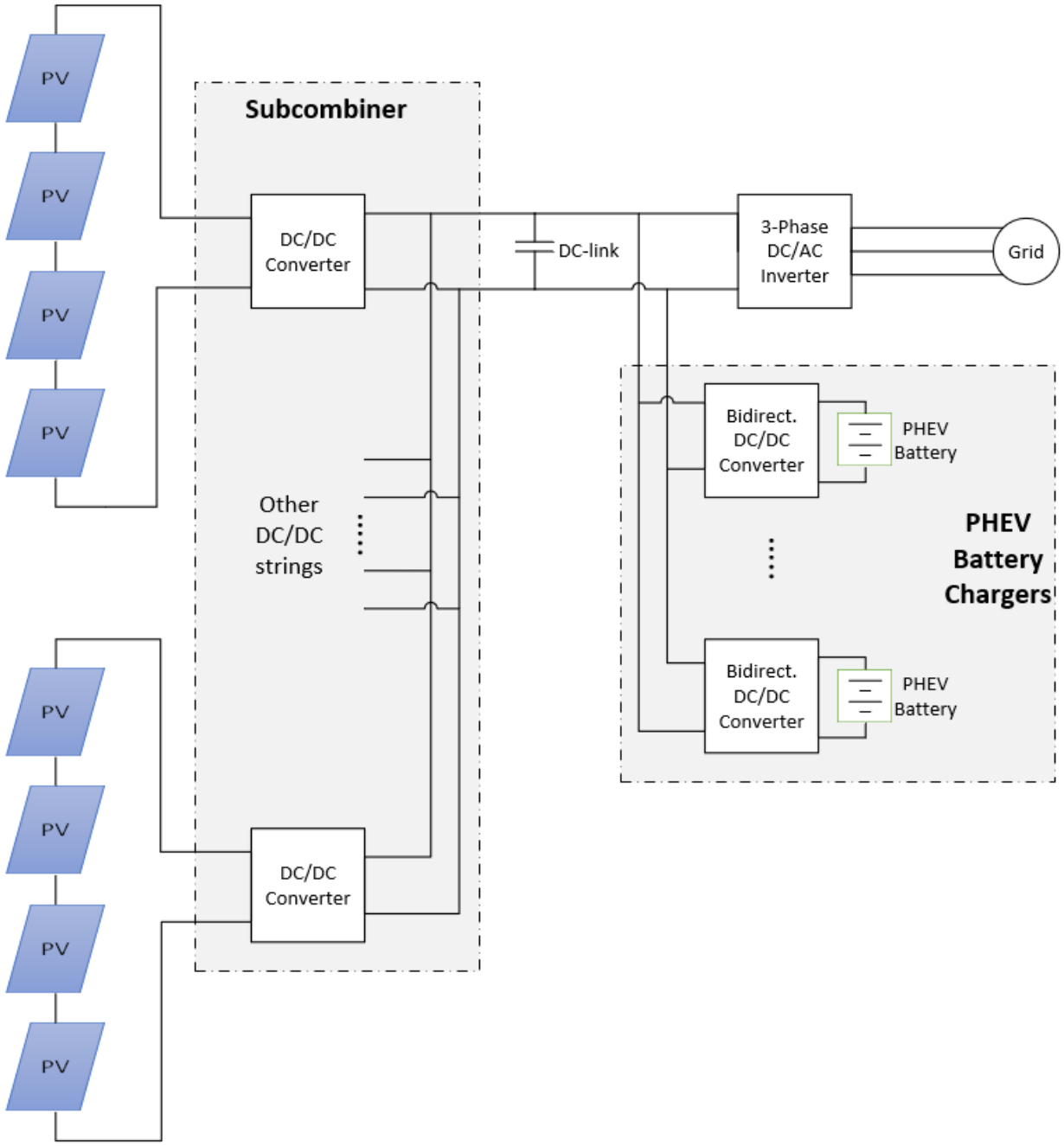

Figure 12: PHEV bidirectional battery charger integrated to a PV system [37]

A simulation study has been done by [38] that integrates a fuel cell to a PV grid-tied and stand-alone system. The charging discharging method was simply to maintain the match between the output power of the system and the load rate. Similarly, in [46], hydrogen energy has been used in a PV system to balance the fluctuation of PV output power. An exponential moving average was used for PV-firming.

Table 2 summarizes the differences between all reviewed PV-firming technologies in terms of energy storage used in the system, the category of the PV-storage integration (Figure 9), firming method applied in the control, and the rated power.

Table 2: Summary for a comparison between different PV-firming technologies.

PV-Firming Technology	Energy Storage	Integration Category	Firming Method	Rated Power(W)
Ref. [36]	*VRLA*	*AC-Side*	*Moving Average*	*3.5 k*
Ref. [37]	*PHEV Battery*	*DC-Side*	*Corner Freq. (Filter)*	*25 k*
Ref. [38]	*Fuel Cell*	*DC-Side*	*Load-based*	*20 M*
Ref. [39]	*SMES*	*AC-Side*	*Load-based*	*40 M*
Ref. [40]	*EDLC*	*DC-Link*	*Moving Average*	*1 k*
Ref. [41]	*EDLC*	*DC-Side*	*Moving Average*	*200 k*
Ref. [42]	*BESS*	*AC-Side*	*Storage Capacity-based*	*1 M*
Ref. [43]	*LA Battery*	*DC-Side*	*Power slope-based*	*400*
Ref. [44],[45]	*BESS*	*AC-Side*	*Limits (max. & min.)-based*	*1 M*
Ref. [46]	*Hydrogen*	*DC-Side*	*Exponential Moving Average*	*3 k*

2.2 Three-Port PV Connected Microinverters

Recent, but limited, studies were found using three-port microinverter that integrates PV and storage. Similar to the two-port microinverter, there are several advantages of the three-port micro-conversion system over the utility scale system as follows as discussed in [47], [48], [49], [50], and [51].

1) Independently Control Optimization: Every individual PV panel conversion system can independently control and optimize the power flow in all directions. Every system can independently and optimally charge and discharge its battery. For each PV, the converter can independently obtain maximum power point tracking (MPPT).
2) Battery Management and Protection: Every battery can be replaced or fixed when it reaches its maximum number of life cycles or needs maintenance. Battery protection can be applied intelligently for each PV panel converter. In other word, based on the state of charge (SOC), for instance, each battery can be protected from damage due to deep discharge.
3) Improved Data Collecting Capability: Every PV-battery-conversion module can have a permanent data collection capability. There can be a control network connection between all modules and converters. This can facilitate the maintenance requirement for each PV panel or battery.
4) Improved Maintenance: If one of the devices doesn't work properly, the system doesn't have to be shut down totally in order to replace or repair.

In [52] and [53], authors proposed multi-port system that interfaces several renewable energy sources such as PV cell, fuel cell, wind turbine, and battery. The topology consists of interleaved boost for DC/DC converter stage and full-bridge for DC/AC inverter stage. Both stages are connected to a common DC-link. Figure 13 illustrates shortcut of the proposed topology in [52] and [53] to become only three-port. As the shown in the figure, the DC-link, which is the output of the DC/DC is stage, powers the grid through the full-bridge inverter and a low frequency transformer.

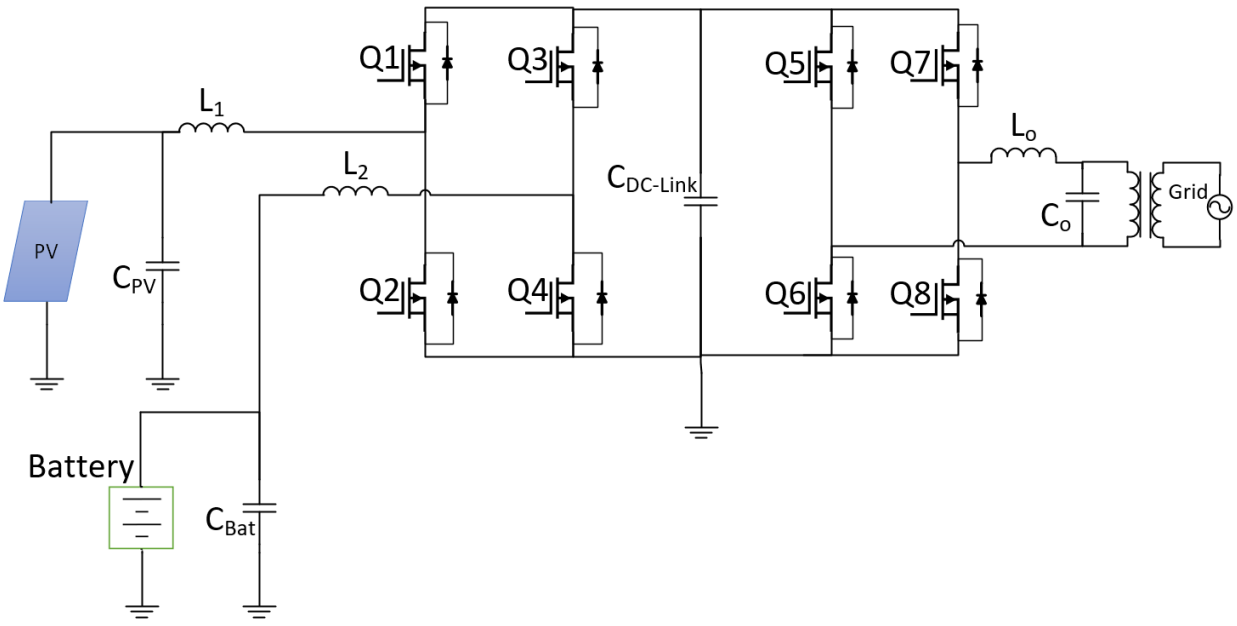

Figure 13: Interleaved boost convert based topology [52], [53]

Figure 14 illustrates a three-port conversion system integrated with battery for PV stand-alone applications presented by [54]. This topology is achieved based on a traditional half-bridge two-port converter, where the middle devices of S3 and D3 are added to integrate a third port (battery) conversion stage. MPPT control is applied at the PV port, while bidirectional charging/ discharging control is implemented at the battery port. Hence, a rectified sinusoid voltage is generated. A low frequency (50/ 60Hz) unfolding circuit is cascaded to perform sinusoid AC voltage.

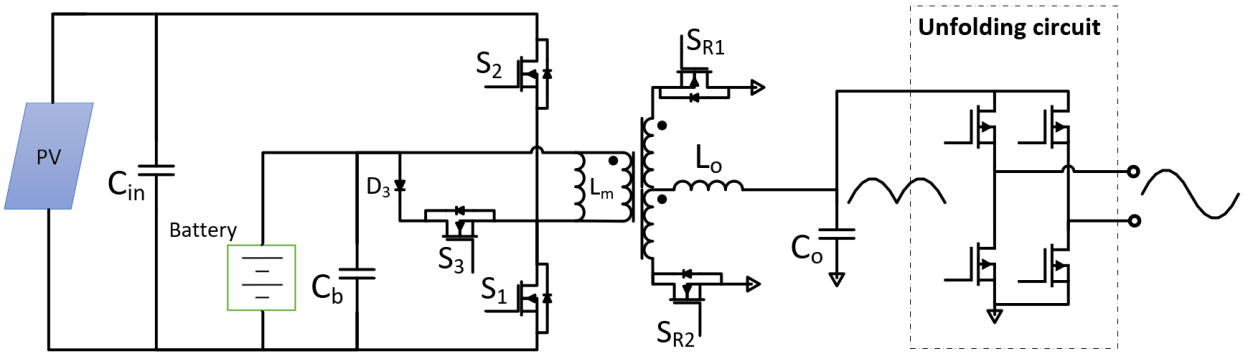

Figure 14: A stand-alone PV/battery system proposed by [54].

Figure 15 displays a non-isolated single-stage three-port microinverter with high-frequency AC link based interfacing [55]. It is multi-input/ multi-output and three-phase inversion topology with power level of 800W. The bridges for battery and grid ports have bidirectional switches to enable bidirectional conversions for charging and discharging the battery. The AC link consists of low reactive parallel LC components which make partial resonance in the conversion system. The main

storage component in this topology is the inductor. The capacitor component helps the inductor facilitate the partial resonance during the operation modes of power conversion. Zero voltage turn on of the switches and higher efficiency are a result of the partial resonance. The difference between this three-port microinverter and the resonant converters is the shortened resonance time.

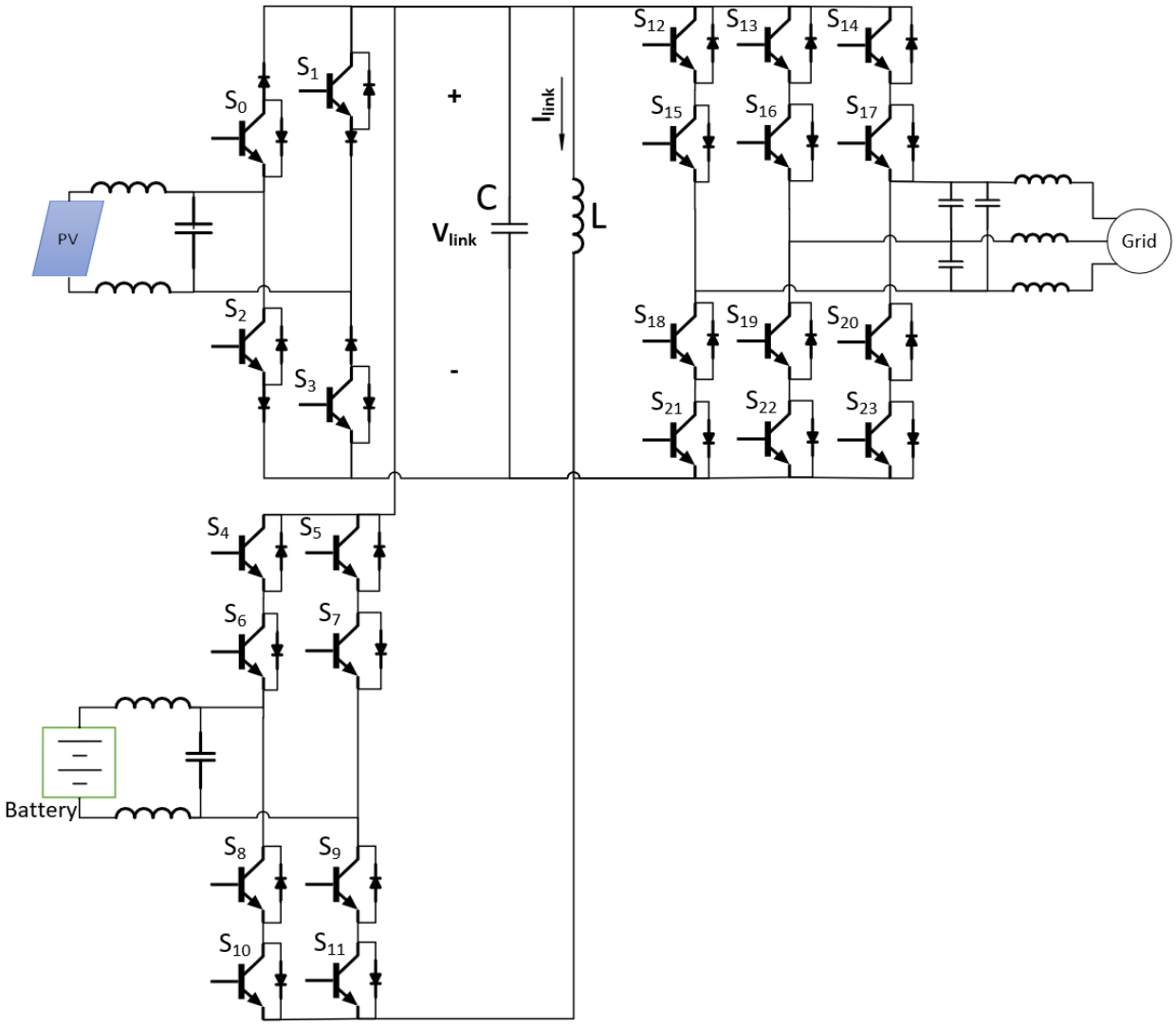

Figure 15: A multiport AC link PV inverter with reduced size and weight for stand-alone application by [55]

Another three-port microinverter has been presented in [56] and [57] in which the third port is intended to achieve the power decoupling function. It is based on the three-port flyback topology,

as shown in Figure 16. It integrates PV and power decoupling capacitor interfacing into the grid. Recognized advantages include: low number of components, compact size, adequate efficiency, and low cost. Compared to the conventional flyback converter, one diode and one switch are added to implement the function of the power decoupling. It should also be noted that the power decoupling capacitor not only acts as a buffer to balance the double-frequency ripple, it also acts as a snubber and recycles leaked energy. A drawback of this topology is that its full load (100W) efficiency is less than 90%. However, only two switches are operating at high frequency to reduce the power losses.

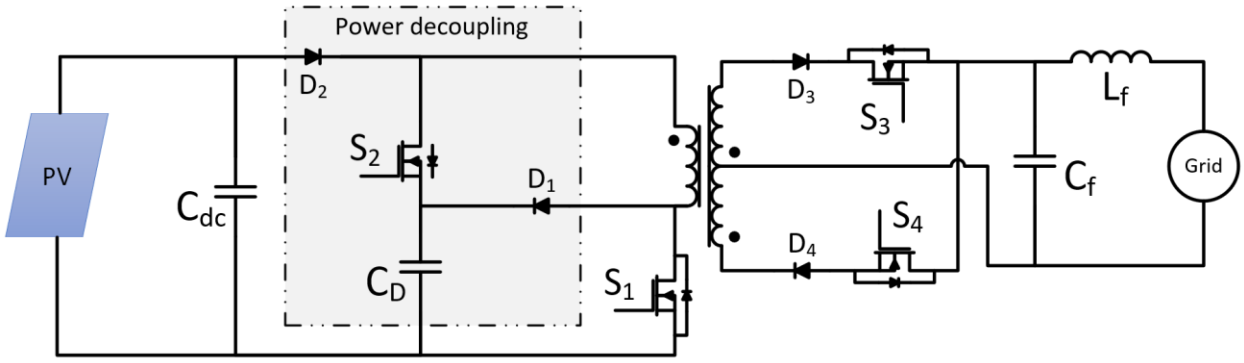

Figure 16: A single-stage microinverter without using electrolytic capacitors by [56].

Figure 17 shows a system where a soft-switched isolated three-port single-phase microinverter provides power management for a PV system interfacing with battery and AC load [58]. The power delivered to the AC load can be supplied by either PV or battery or both simultaneously. Unlike

the three-port single-phase microinverter in [56], the switches connected on the primary side of the transformer are switched on under zero voltage switching (ZVS) status. This presented topology has advantages over the existent soft-switched multiport AC link inverter in [55] including size reduction and fewer active components.

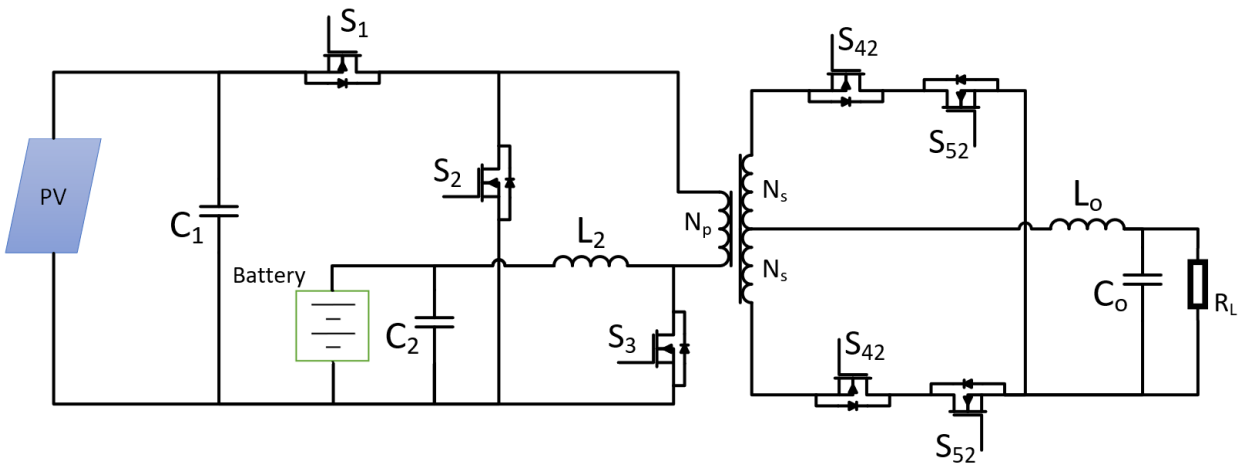

Figure 17: A soft-switched three-port single-phase microinverter topology by [58].

For more clarification on how those presented topologies differ from each other and to gain more understanding, Table 3 shows comparison for most important key characteristics of the PV-battery microinverter. These characteristics are rated power, PV and battery voltages, AC line (grid) voltage, switching frequency, number of active and passive components, value of DC-link capacitor (if any) and filter inductor, and efficiency.

Table 3: Key characteristics of presented topologies

Topology	Rated Power (W)	PV Voltage (V)	Battery Voltage (V)	AC Voltage (V)	Switching Frequency	Active Devices	Passive Components	DC-link Capacitor (uF)	Filter Inductor (mH)	Maximum Efficiency (%)
Figure 10	*1200*	*-*	*120*	*120*	*20*	*8*	*8*	*880*	*1*	*< 90*
Figure 11	*60*	*60*	*28*	*120*	*-*	*10*	*6*	*-*	*-*	*-*
Figure 12	*800*	*150*	*200*	*208*	*4*	*28*	*10*	*0.4*	*-*	*91*
Figure 13	*100*	*60*	*60*	*110*	*50*	*8*	*5*	*-*	*1*	*90.23*
Figure 14	*120*	*43.2*	*24*	*120*	*200*	*7*	*7*	*-*	*0.018*	*-*

2.3 Merits Comparison between Reviewed and Proposed Technologies

The proposed technologies are presented in chapter 3 and 4 which are static and dynamic PV-firming technologies. Table 4 summarizes the merits of the proposed PV-firming technologies compared to the previous reviewed technologies. It is realized from Table 4 that the applied PV-firming methods can be classified into four main methods; traditional/exponential moving average method, corner frequency filtering, load (demand)-based firming, storage capacity-based firming, power slope-based firming, limits (maximum & minimum)-based firming, and the proposed PV-firming algorithms (static and dynamic). The majority of the reviewed technologies for the PV-firming are applied for high power level (PV arrays and energy storage stations). However, modular level systems (PV panel with micro-inverter and integrated storage) will be a future focus for solar PV deployment because of several remarkable merits as discussed in section 2.2. The speed response of the PV-firming method defers if the method is calculation-based or comparison-

based. In [38], [39], [44], [45], and proposed algorithms in this dissertation, the PV output power is compared to a specified reference and then the output firmed profile is deployed. This result in high speed response that takes micro-seconds. In contrast, other methods depend on mathematical calculations such as applying traditional/ exponential moving average method. Another important merit is to not depend on the previous PV power measurements. Unlike the proposed strategy for PV firming, the traditional/ exponential moving average method have a memory effect and therefore the energy storage devices must be controlled with being influenced by the PV output power at the previous times requirements and effecting on the future compensating power. For the rest technologies including the proposed algorithms, the energy storage devices can be controlled (charged/ discharged) according to the instant time requirements only. The ability of smoothing the high fluctuations by including a ramp-rate control in the system is very valuable merit. This capability is not available in every technology such as in [38], [39], [44], and [45]. Also, not all the technologies have the strategy of charging the batteries (storage devices) by the PV all the daytime. In [37], [38], [39], [44], and [45], the energy storage are mostly charged during the night by the utility. Moreover, although most of the technologies are applied for high power level, some of them can be applicable to PV panel level system. In conclusion, unlike the reviewed technologies of PV-firming, the proposed strategy aims to function all the addressed merits.

Table 4: Merits comparison between PV-firming technologies.

PV-Firming Technology	Ref. [36]	Ref. [40]	Ref. [41]	Ref. [46]	Ref. [37]	Ref. [38]	Ref. [39]	Ref. [42]	Ref. [43]	Ref. [44],[45]	Ch. 3, 4
Firming Method	*Tranditional/Exponential Moving Average*				*Corner Freq. (Filter)*	*Load-based*		*Storage Capacity-based*	*Power slope-based*	*Limits (max. & min.)-based*	*Proposed Algorithms*
Rated Power(W)	*3.5 k*	*1 k*	*200 k*	*1 M*	*25 k*	*20 M*	*40 M*	*1 M*	*400*	*1 M*	200
High Speed Response (μ-sec.)						✓				✓	✓
No memory effects					✓	✓		✓	✓	✓	✓
Ramp-rate control capability			✓		✓			✓	✓		✓
PV-to-Bat. all daytime			✓					✓	✓		✓
μ-system applicability			✓		✓				✓		✓

CHAPTER 3: PROPOSED TOPOLOGY AND STATIC PV FIRMING ALGORITHM

3.1 Introduction

In this chapter, a new approach to PV firming is presented. The batteries are integrated directly on the DC-link of a PV-microinverter (H-bridge) with a flyback converter forming the first power conversion stage. This results in a three-port microinverter. The major focus of this chapter lies in the static PV firming and the control algorithms to charge/discharge the batteries. This leads to a firmed power profile being generated through the inverter stage. In Section 3.2, the proposed topology and controls without firming algorithms are discussed. The static PV firming algorithm is added and proposed in Section 3.3. In Section 3.4, MATLAB/SIMULINK simulations are performed, and the relevant waveforms are shown. Experimental validation of the proposed schemes is presented in Section 3.5. An analysis of the storage capacity for the static algorithm in the previous chapter is discussed in Section 3.6.

3.2 Proposed Topology and Operational Principle

3.2.1 The Topology

The proposed grid-tied three-port bidirectional microinverter is given in Figure 18. This microinverter can interface battery, PV panel, and the grid. It has the capability to convert from single-input to single-output (SISO), single-input to dual-output (SIDO), and dual-input to single-output (DISO). SISO occurs when power transfers from PV or battery to the grid, or when power transfers from the grid to the battery. SIDO occurs when power transfers from PV to both the battery and the grid. DISO occurs when power transfers from both PV and battery to the grid. This two-stage converter is directly obtained from well-known flyback converter and H-bridge inverter topologies. The proposed topology is composed of six active components (one diode and five devices (MOSFETs)) and four passive components (two capacitors, a transformer, and an inductor). Moreover, in order to disconnect the battery, a relay switch is required. The active components and the relay are controlled to interface with the three different ports and regulate their power flows, voltages, and currents.

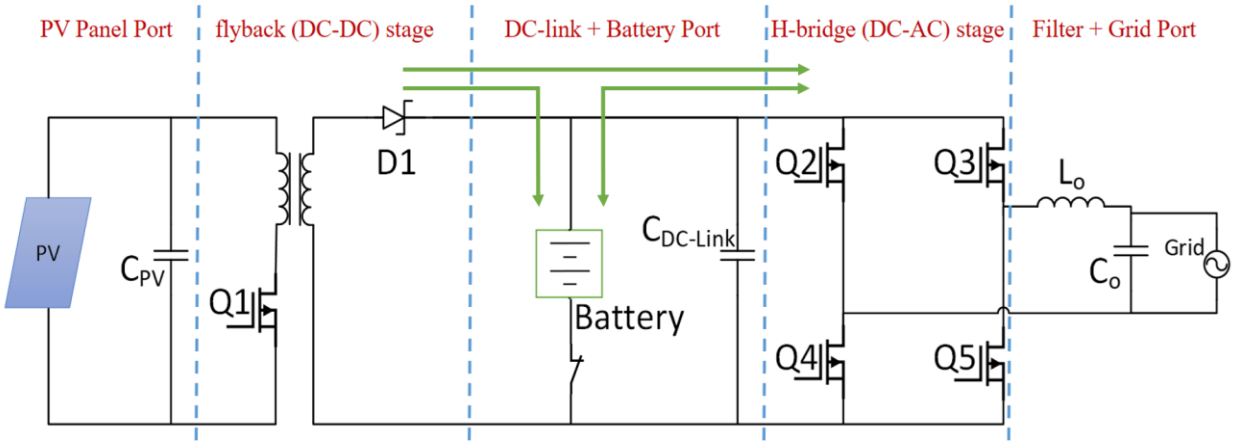

Figure 18: The proposed grid-tie three-port PV microinverter.

The flyback (DC-DC) stage is used to step up the PV voltage to produce a nominal DC-link voltage of 225V. The H-bridge (DC-AC) stage is used for inverting the DC-link voltage to the AC voltage (grid) of 120V RMS. The third port of battery is connected in parallel to the DC-link. Because of the battery flexibility in voltage with respect to its size, it is designed to make the battery voltage the same as the DC-link voltage without having to use an additional stage for battery power conversion. The proposed topology has the capability to operate in six different scenarios, PV to Grid, PV to Grid/Battery (charging), PV/Battery to Grid (discharging), PV/Grid to Battery (charging), Battery to Grid (discharging), and Grid to Battery (charging).

3.2.2 Implemented Controls Regardless of the Proposed Algorithms

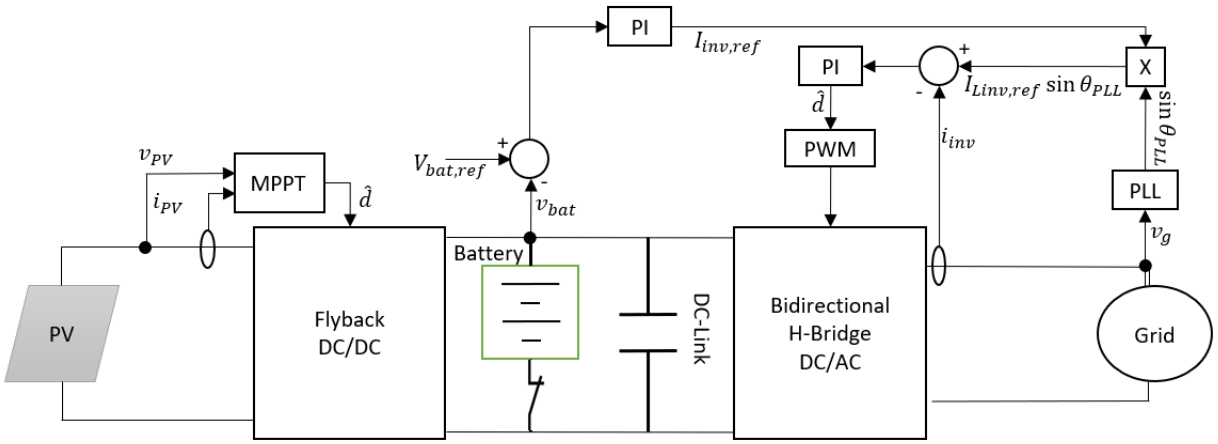

Figure 19: Block diagram for the proposed three-port system with the implemented controls without firming algorithms.

Figure 19 represents a full overview of the proposed system with the implemented controls that can be used regardless of the PV-firming and optimization algorithms. For the DC/DC stage, a maximum power point tracking (MPPT) algorithm is used. Other controls are used through the DC/AC stage. These controls are phase locked loop (PLL), DC-link voltage regulation control (DCVR), and output current regulation control (OCR) [59]. The proposed algorithms will be discussed in later sections.

Starting with the PV source, a maximum power point tracking (MPPT) algorithm is used to control the flyback DC/DC converter. It does this according to the maximum power delivered from the PV. In this topology, the author has used the Perturbation and Observation (P&O) technique. The objective of the P&O algorithm is to track the PV voltage and current to maintain the maximum power. Then, the duty value for the flyback is set according the reference PV voltage chosen by the algorithm when the power is maximized. Figure 20 shows the flowchart of the MPPT algorithm.

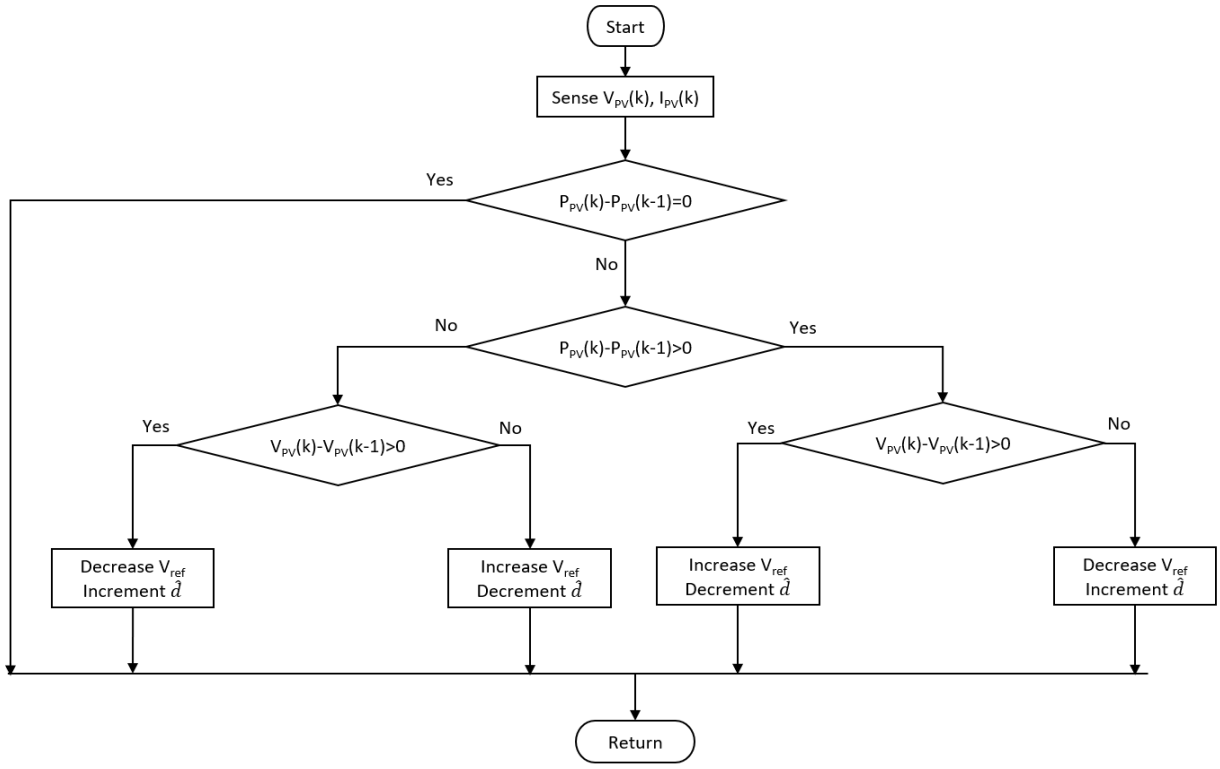

Figure 20: Perturbation and observation (P&O) algorithm.

A phase-locked loop (PLL) controller is required when the grid is one of the ports in this system. Basically, the PLL functions to track the phase and frequency of the fundamental grid voltage. This results in a pure sine wave, which matches the grid's characteristics with a unit amplitude.

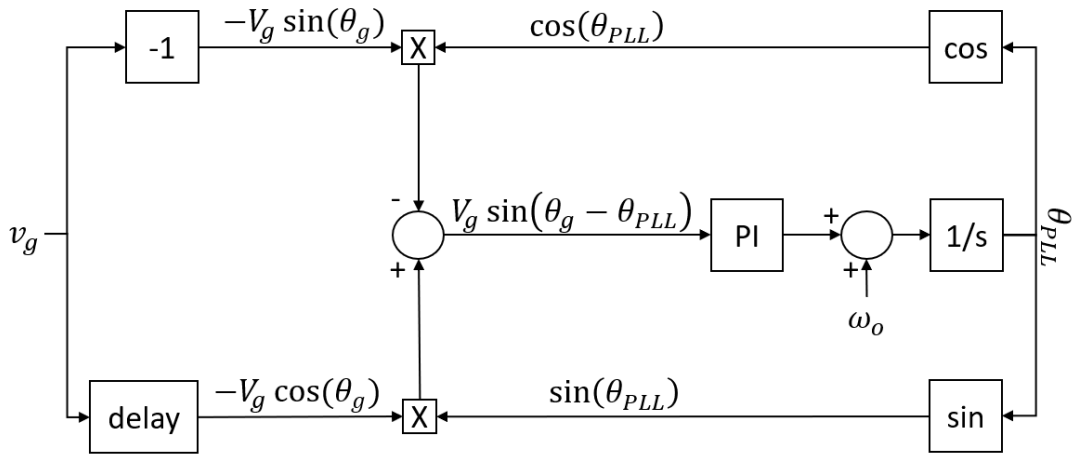

Figure 21: Block diagram of the used PLL controller.

As shown in Figure 21, the *Error* optimized by the PI controller included in the PLL is expressed as follows.

$$Error = V_g \sin(\theta_g)\cos(\theta_{PLL}) - V_g \cos(\theta_g)\sin(\theta_{PLL}) = V_g \sin(\theta_g - \theta_{PLL}) \quad (2)$$

where θ_g and θ_{PLL} are the phase of the utility grid and the PLL output, respectively, and V_g is the amplitude of the grid voltage. At steady state operation, the error that goes into the PI controller $(\theta_g - \theta_{PLL})$ will be equal to zero. So, it will be linearized. By using Taylor series, the error will be a function of grid phase as follows.

$$error(\theta_g) \approx V_g \sin(\theta_g - \theta_{PLL,0}) + \frac{d}{d\theta_g} error(0) \approx V_g(\theta_g - \theta_{PLL}) \quad (3)$$

As a result, the closed-loop transfer function of the PLL is

$$H_{PLL}(s) = \frac{V_g \cdot PI(s) \cdot \frac{1}{s}}{1 + V_g \cdot PI(s) \cdot \frac{1}{s}} = \frac{V_g \cdot PI(s)}{s + V_g \cdot PI(s)} = \frac{\frac{V_g \cdot K_p}{T_i} \cdot (T_i \cdot s + 1)}{s^2 + V_g \cdot K_p \cdot s + \frac{V_g \cdot K_p}{T_i}} \quad (4)$$

The two conversion stages in the proposed systems are interfaced through a DC-link. They must be maintained with a regulated voltage. Therefore, a DC-link voltage regulation control (DCVR) must be implemented. Figure 22 represents the block diagram of the DCVR control.

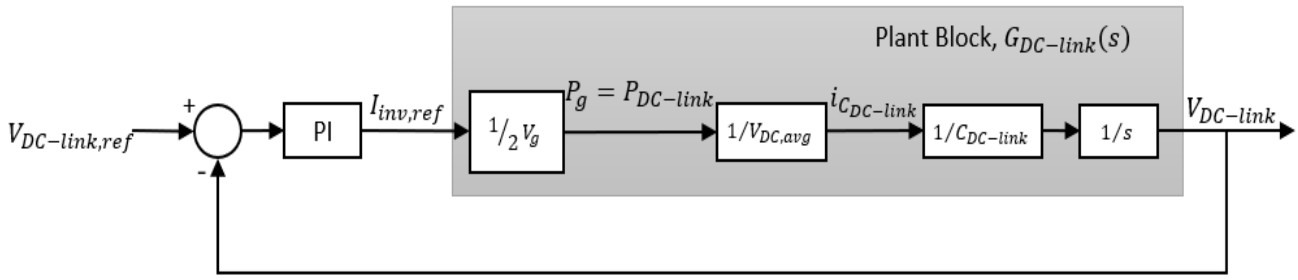

Figure 22: Block diagram for the DC-link voltage regulation control (DCVR).

The purpose of the DCVR is to balance the power into and out of the DC-link. In addition, a reference current amplitude is generated for the inverter stage ($I_{inv,ref}$). This reference value is multiplied by the sine wave generated by the PLL. This produces a reference current for the inverter output current regulation (OCR) control loop, which is discussed later. When this current amplitude is multiplied by half of the grid voltage amplitude, it results in the grid average power. Using this information, the DC-link power ($P_{DC-link}$) is computed. Dividing the DC-link power by its average voltage ($V_{DC-link,0}$) produces its current ($i_{DC-link}$). Finally, the actual DC-link voltage is computed by dividing the integral of the DC-link current by its capacitor.

The plant transfer function (voltage-to-current) for DCVR is:

$$G_{DC-link}(s) = \frac{V_{DC-link}}{I_{inv,ref}} = \frac{V_g}{s^2 C_{DC-link} V_{DC-link,0}} \quad (5)$$

After multiplying the reference amplitude of the inverter output current ($I_{inv,ref}$) by the unity sinusoidal function ($\sin(\theta_{PLL})$) generated by the PLL, the OCR will be operated. The loop structure of the OCR is shown in Figure 23.

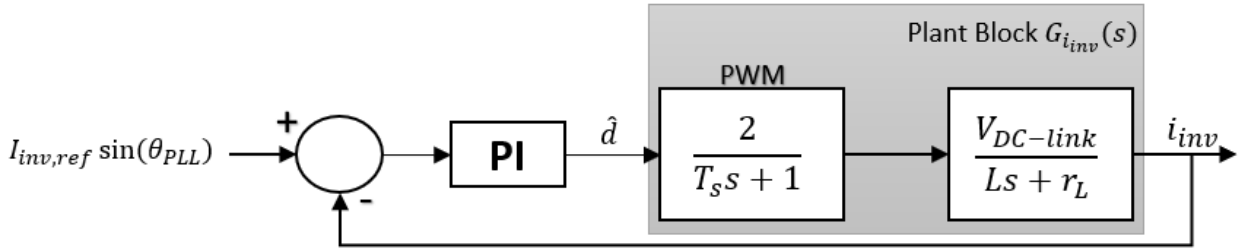

Figure 23: Block diagram for the output current regulation control (OCR).

The plant transfer function (current-to-duty) for the OCR control is

$$G_{i_{inv}}(s) = \frac{2}{T_s s+1} \cdot \frac{V_{DC-link}}{Ls+r_L} \quad (6)$$

where;

- T_s: Switching period.
- $V_{DC-link}$: DC-link average voltage.
- L: Inverter filter inductor.

- r_L: Series inductor resistance.

In the next section, a proposed algorithm to be integrated to the previous controls, which is necessary to interface with a third port for the energy storage.

3.3 Proposed Static PV Firming Algorithm

In order to interface with a third source of power such as a battery, an additional control algorithm must be implemented. In this research, the proposed algorithm controlling the battery power and operation [charging/discharging] depends on the reference output power profile. The static PV reference generation method and the battery charging/discharging algorithm are discussed in this section.

3.3.1 Static PV Reference Generation Method

The static PV reference generation method is based on the historical PV intermittency data for a specific region or area. East Florida is the region selected for this research. The data is collected online by the Florida Solar Energy Center at the University of Central Florida, Cocoa campus [2]. Data is collected from a combination of two 300W PV modular systems consisting of PV panel and grid-tied microinverter.

The East Florida region static PV reference power ($P_{PV,ref}$) is calculated by averaging the daily data for each month with a resolution of a minute [60]. Each month is assumed to have specific average PV reference power ($P_{ref,avg}$), which is calculated using equations (7) and (8).

$$P_{ref,avg}(t) = \left\{P_{ref,avg}^{m_1}, P_{ref,avg}^{m_2}, \dots, P_{ref,avg}^{m_k}\right\} \quad (7)$$

$$P_{ref,avg}^{m_n} = \frac{\sum_{d_1}^{d_l}\left(P_{ref,avg}^{m_n}(d_n)\right)}{l} \quad (8)$$

where,

- $m_1, m_2, m_3 \dots m_k$: correspond to the minutes over a day.
- k: is equal to 1440, which is the total minutes in each day.
- $d_1, d_2, d_3 \dots d_l$: correspond to the days in each month.
- l: is the total number of days in each month.
- $P_{PV,avg}^{m_n}$: is the nth minute's average value of PV power in a month.

A similar method is applied for the calculating the maximum PV reference power ($P_{ref,max}$) using equations (9) and (10). This maximum reference will be used and discussed in the next chapter for performing the dynamic method. Figure 24 shows examples of energy reference power profiles for three different days in 2016 (Feb. 19th, May 14th, and Aug. 17th).

$$P_{ref,max}(t) = \left\{P_{ref,max}^{m_1}, P_{ref,max}^{m_2}, \dots, P_{ref,max}^{m_k}\right\} \quad (9)$$

$$P_{ref,max}^{m_n} = Max_{d_1}^{d_l}\{P_{ref,max}^{m_n}(d_n)\} \quad (10)$$

where,

- $P_{ref,max}^{m_n}$: is the nth minute's maximum value of PV power in a month.

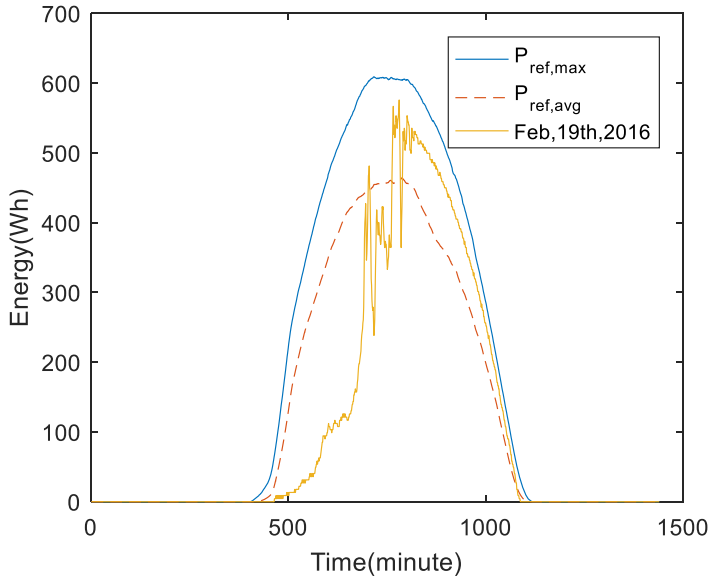

(a)

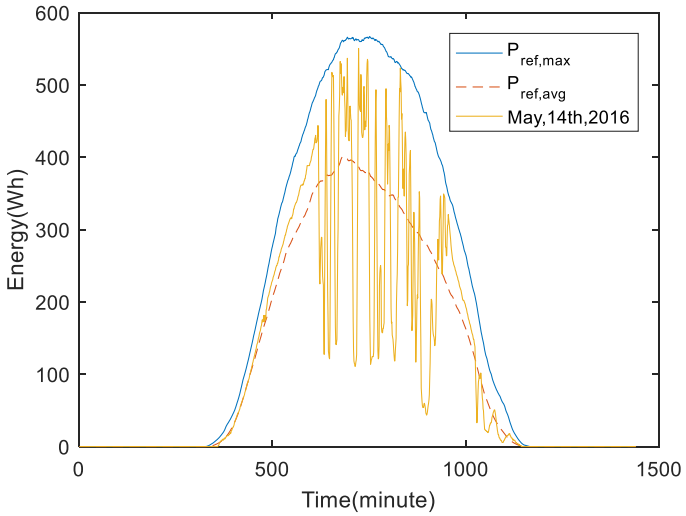

(b)

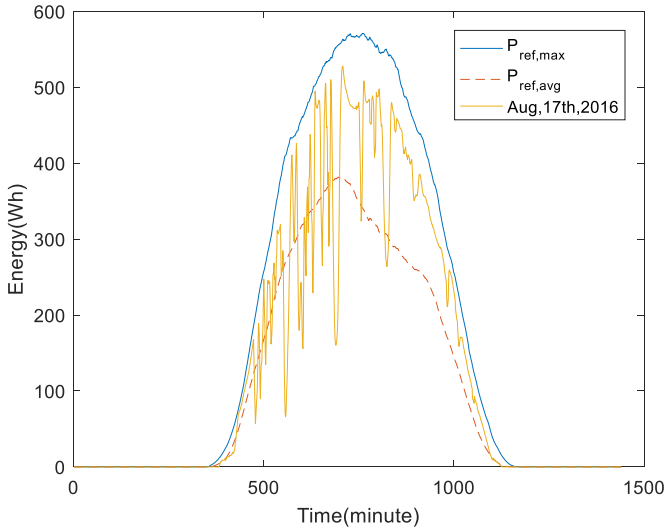

(c)

Figure 24: Maximum and average PV reference power compared to PV actual power on different days in 2016, where (a) is on Feb, 19th, (b) is on May, 14th, and (c) is on Aug, 17th.

In the next step, the generated static PV reference profile is used in the PV firming battery charge/discharge control algorithm, which is presented in the next section, to produce the final power profile through the three-port microinverter.

3.3.2 Battery Charging/ Discharging Algorithm

Once the desired profile of the PV reference curve is generated, it is fed into the power electronics design through the microcontroller. It does this in order to control the battery charging discharging scenarios. An algorithm for charging/ discharging decisions is proposed in this research. Figure 25 illustrates the proposed architecture of the PV firming system with this algorithm added to the other controls mentioned in Section 3.2.

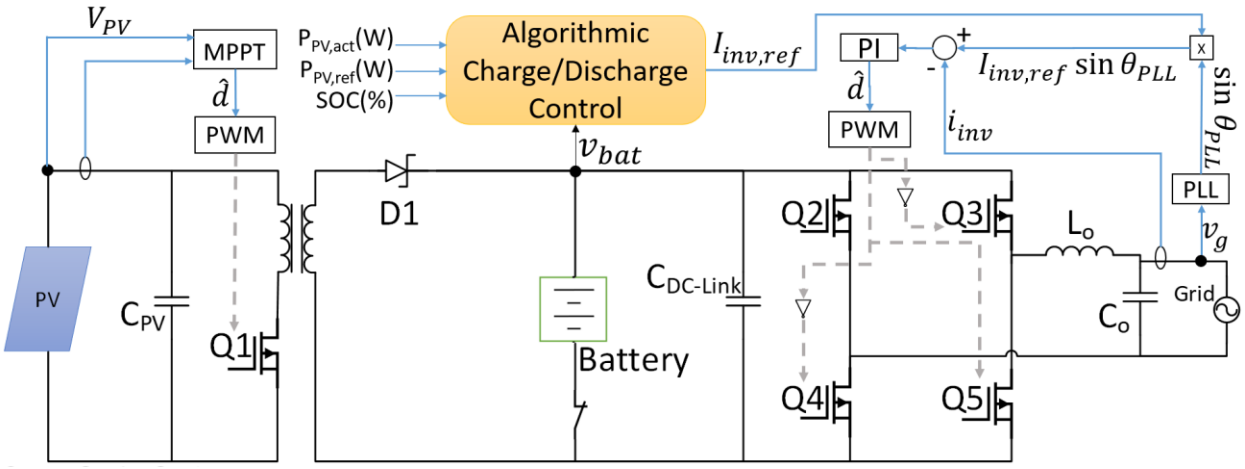

Figure 25: Architecture of the proposed PV firming system.

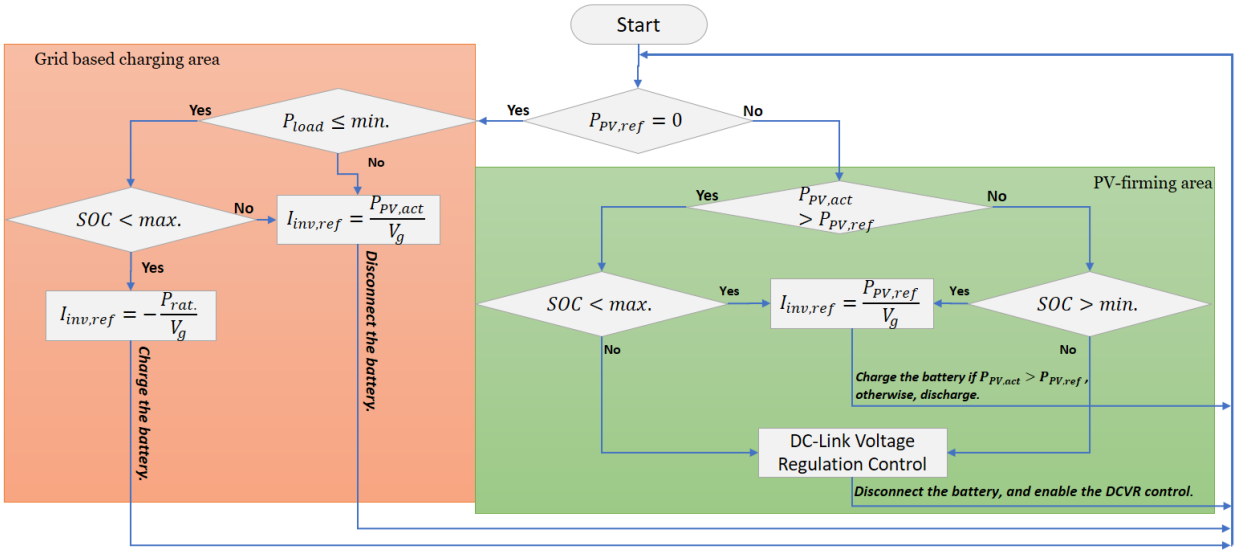

Figure 26: The algorithm flowchart for the PV firming battery charge/discharge control.

Figure 26 represents the proposed algorithm flowchart for the PV firming battery charge/discharge control. The green section displays the PV-firming process scenario, while the red section displays the grid based charging scenario. This research focuses on the PV-firming section. A brief discussion for the grid based charging section is also presented.

In the battery charge/discharge control algorithm of the PV-firming section in Figure 26, each process of the proposed algorithm will end up with two decisions. First, the generated value of the inverter reference current ($I_{inv,ref}$) is decided. This controls the battery current value (I_{bat}) simultaneously. Second, the decision of either charging, discharging, or disconnecting the battery occurs. Both decisions are based on four factors: the actual PV output power ($P_{PV,act}$), the generated PV reference power ($P_{PV,ref}$), the state of charge (SOC) of the battery energy, and the battery voltage (V_{bat}). The objective of the algorithm in Figure 26 (PV-firming section) is to make the $P_{PV,act}$ matched with the $P_{PV,ref}$ by charging/discharging the battery.

The algorithm begins by comparing the generated PV reference power ($P_{PV,ref}$) to the actual PV power ($P_{PV,act}$) in real time. After each comparison, the state of charge (SOC) will be determined. When the $P_{PV,act}$ is greater than the $P_{PV,ref}$ and the SOC is less than its maximum percentage of energy, the battery is charged. The inverter reference current ($I_{inv,ref}$) is then calculated using equation (10). Whenever the $P_{PV,}$ is less than or equal to the $P_{PV,ref}$ and the SOC is greater than its minimum percentage of energy, the battery will be discharged. The $I_{inv,ref}$ is then again determined using equation (10). Equations (11) and (12) represent the ideal case of the battery

current (I_{bat}) when it is being charged and discharged, respectively. This value for I_{bat} is determined simultaneously with the inverter current value (I_{inv}).

$$I_{inv,ref} = \frac{P_{PV,ref}}{V_g} \quad (11)$$

$$I_{bat} = -\frac{P_{bat}}{v_{bat}} = I_{PV} - I_{inv} \quad (12)$$

$$I_{bat} = \frac{P_{bat}}{v_{bat}} = I_{inv} - I_{PV} \quad (13)$$

Since the DC-link has a constant voltage from the battery, there will not be a need to regulate control of the DC-link voltage. However, once the SOC is equal to its minimum or maximum percentage of energy, the battery is disconnected and the $I_{inv,ref}$ is generated by the DC-link voltage regulation control (DCVR) which is addressed previously in Section 3.2.2. This situation of disconnecting the battery is considered as rarely occurrence compared to being charged or discharged because of the instability of the PV power levels. Therefore, a power relay can be a suitable device to be implemented for disconnecting the battery. As shown in Figure 27, there are two different scenarios that provide the $I_{inv,ref}$: the charging/discharging scenario and the DCVR scenario.

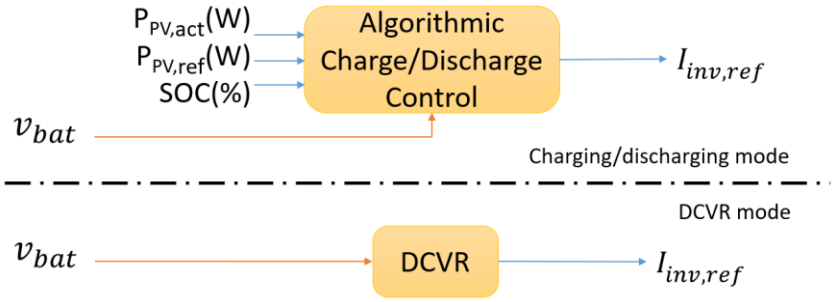

Figure 27: Scenarios configuration for the inverter reference current generation.

In the grid-based charging section, the algorithm begins by evaluating the load power (P_{load}) since the $P_{PV,ref}$ is constantly zero. If P_{load} is at minimum or below (low peak), the system will take advantage of the low-price power to charge the battery from the grid. Meanwhile, the *SOC* is assured to not exceed the maximum percent. If so, the $I_{inv,ref}$ is calculated based on the rated power (P_{rat}) as in (14). If P_{load} is greater than minimum or the *SOC* is in maximum percent, the battery will be disconnected and the $I_{inv,ref}$ will be generated by the DC-link voltage regulation control.

$$I_{inv,ref} = -\frac{P_{rat}}{V_g} \qquad (14)$$

3.4 Simulation Results

Simulations are carried out using MATLAB/Simulink to validate the proposed static PV-firming algorithm on the grid-tied two-stage battery-integrated topology shown earlier in Figure 18. Power waveforms for the generated PV reference power ($P_{PV,ref}$), the PV actual power ($P_{PV,act}$), the inverter stage output power (P_{inv}), and the battery power (P_{bat}) for the static PV firming microsystem are shown in Figure 28. Since the MATLAB/Simulink simulations take a long time to perform the calculations, the timeline for the waveforms is scaled down to 24 seconds. This removes the rate fluctuations from consideration. The battery power (P_{bat}) is either positive indicating that the battery is discharging power to the grid, or negative indicating that the battery is being charged from the PV. The DC-link voltage ($V_{dc-link}$), inverter output current (I_{inv}), and inverter reference RMS current ($I_{inv,ref}$) are as shown in Figure 29. The $V_{dc-link}$ is between 210V to 245V, which is the battery voltage. The $I_{inv,ref}$ is equal to the RMS value of the sinusoidal I_{inv}.

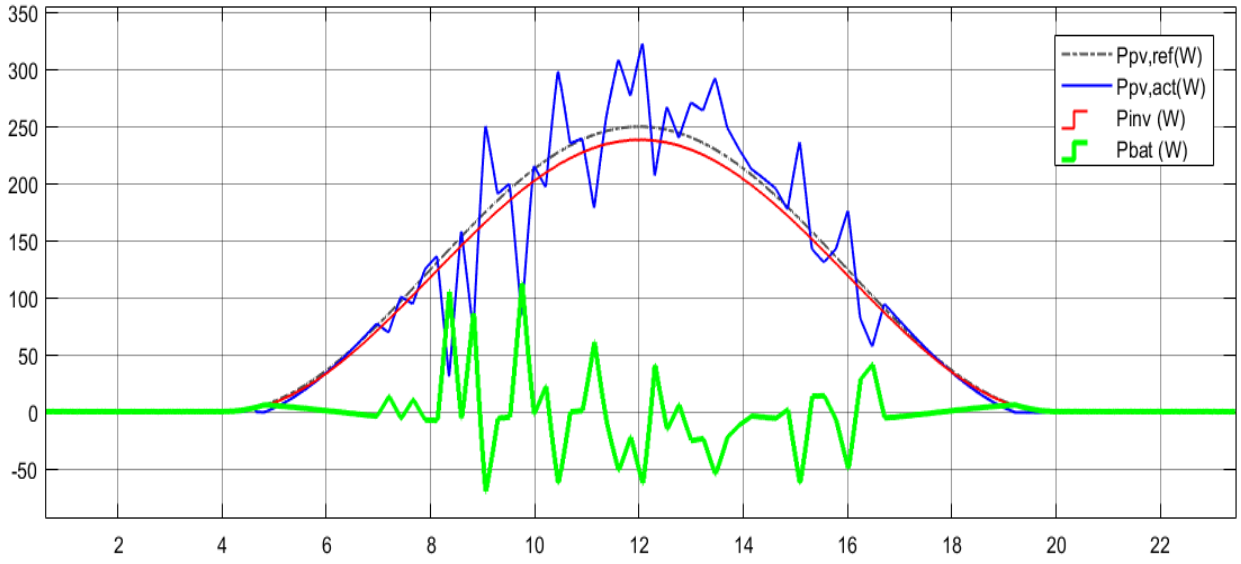

Figure 28: Power waveforms for PV reference (scatter black), PV actual (blue), firmed inverter output (red), and battery (green) for the static firming microsystem.

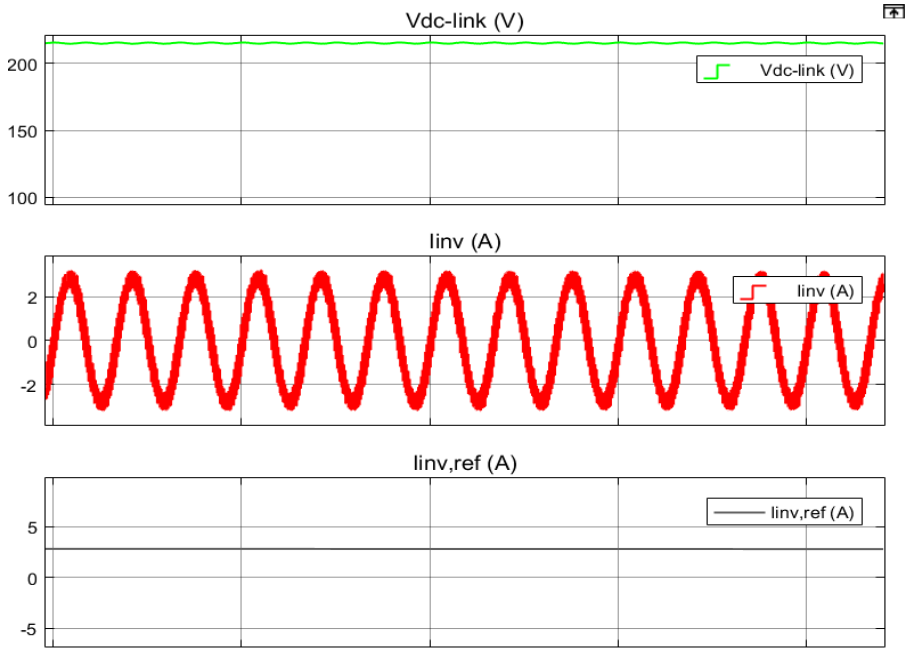

Figure 29: DC-link voltage (Vdc-link), inverter output current (Iinv), and inverter reference RMS current (Iinv,ref) waveforms.

3.5 Experimental Results

To verify the proposed static PV-firming control algorithm experimentally, a 200W prototype is built with specifications as shown in Table 5. The prototype test set-up consists of Solar Array Simulator (Agilent - E4350B) interfaced with AC Power Source/ Analyzer (Agilent - 6812B) to represent the grid voltage and loaded with AC Electronic Load (PCZ1000A). The power waveforms are monitored by a Digital Power Analyzer (YOKOGAWA: PZ4000), and the currents

and voltages waveforms are monitored by a Digital Phosphor Oscilloscope (Tektronix: DPO 3034).

Table 5: Prototype specifications

Category	**Value**
Output Power	200W
PV Voltage	24~45V
Grid Voltage/ Frequency	~120V/ 60Hz
Battery Voltage	210~245V (Typically:225V)
Nominal Bus Voltage	225V

For experimental verification purpose, 18 counts of 12-volt lead acid battery (AJC-D1.3S) manufactured by AJC® Battery are connected in series. More specifications for the storage device that is used in the experimental set-up are shown in Table 6.

Table 6: Technical Specifications of the Battery Used in the Experiment.

Specifications		**Description**
Voltage	Nominal	12V
	Cycle	14.5~14.9V
	Float	13.6~13.8V
Rated Capacity 77°F(25°C)		1.3Ah
Chemistry		Sealed Lead Acid (AGM - Absorbent Glass Mat)
Dimensions (mm/inch)	Length	97 (3.82)
	Wedth	43 (1.69)
	Height	52 (2.05)
	Total Height	58 (2.28)
Approx. Weight (kg/lbs)		0.6 (1.32)
Terminal		T1-A

Figure 30 shows the experimental waveforms of the PV output power, the inverter output power (firmed), and the battery power, while charging and discharging for the static PV firming system. The timeline for the waveforms is scaled down to around half an hour. So, the rates of fluctuations have been taken out of consideration. Since the $P_{PV,act}$ (blue curve) has been changed manually using the Solar Array Simulator, the PV output power curve does not display as much fluctuation as real-time power. However, the charging/discharging control algorithm is verified, since the P_{inv} (yellow) is following the generated PV reference power. The P_{bat} is either positive indicating that the battery is discharging power to the grid ($P_{PV,act}$ is greater than the generated PV reference), or negative indicating that the battery is being charged from the PV ($P_{PV,act}$ is less than the generated PV reference). Figure 31 shows experimental waveforms of the grid voltage (V_g), DC-link (battery)

voltage ($V_{dc-link}$) along with inverter output current (I_{inv}) and battery current (I_{bat}) while the battery is being charged. Figure 32 shows the same waveforms while the battery is being discharged. Note that the positive battery current (I_{bat}) implies that the battery is being charged, while the negative implies that battery is being discharged. The average value of $V_{dc-link}$ is about 236V in Figure 31 and 234V in Figure 32, which are in the specified range of the battery voltage. The V_g and I_{inv} are pure sinusoidal as expected.

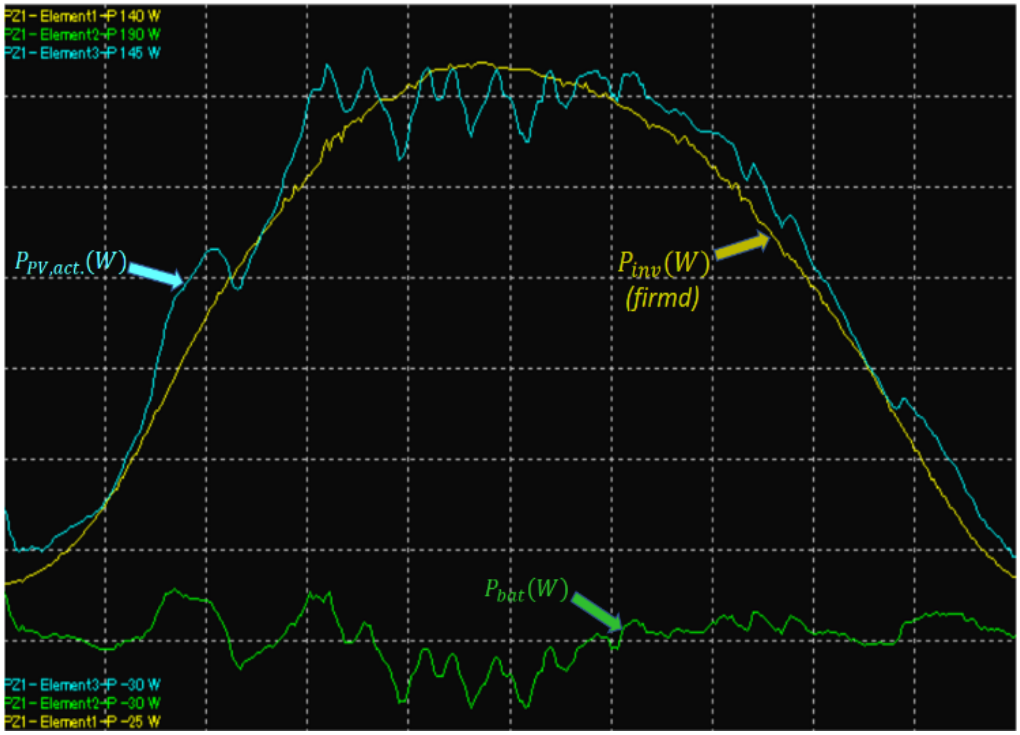

Figure 30: Power waveforms for PV actual, inverter output (firmed), and battery for static firming.

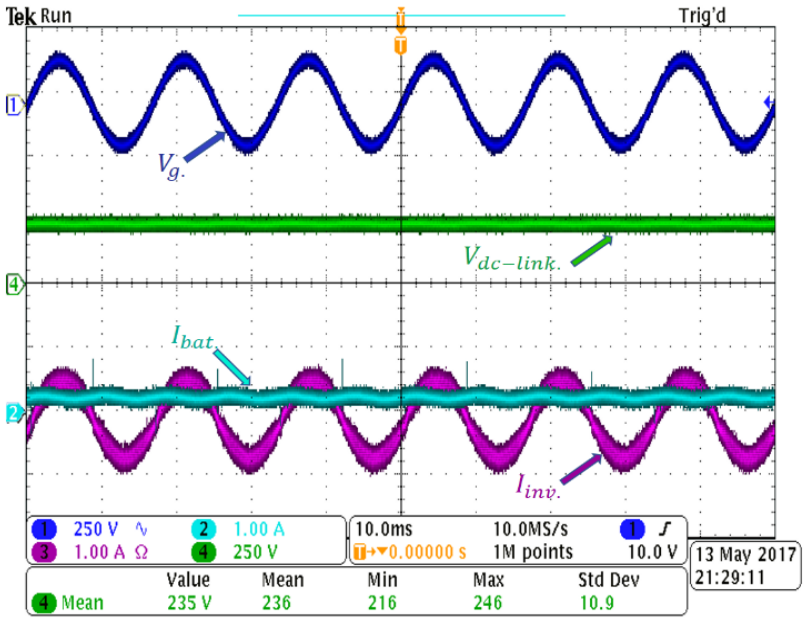

Figure 31: Grid voltage (V_g), DC-link voltage ($V_{dc\text{-}link}$), inverter output current (I_{inv}), and battery current (I_{bat}) waveforms while the battery is being charged.

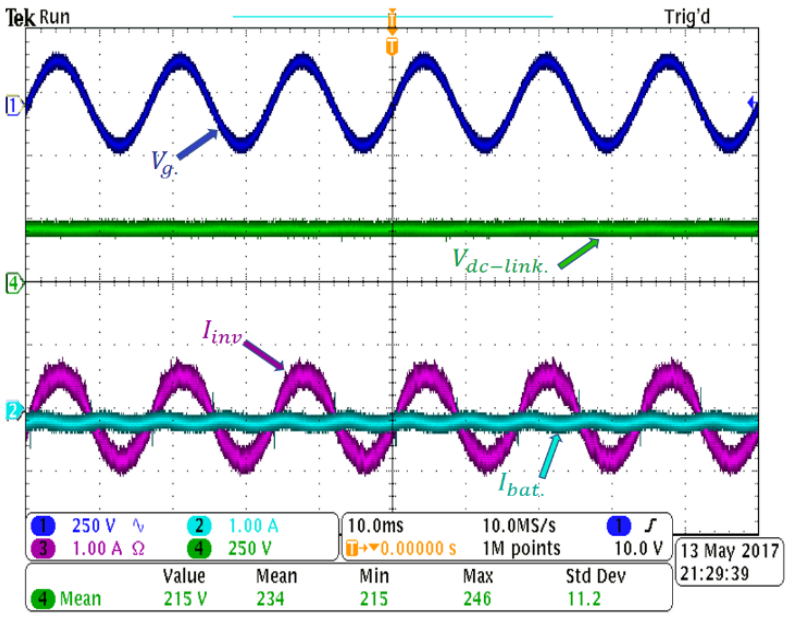

Figure 32: Grid voltage (V_g), DC-link voltage ($V_{dc\text{-}link}$), inverter output current (I_{inv}), and battery current (I_{bat}) waveforms while the battery is being discharged.

3.6 Storage Capacity Sizing Analysis for the Static PV Reference

Energy data was collected for two PV modular systems with 600W total power in [60], where each system consists of a PV panel and grid-tied microinverter. A monthly average PV reference power is generated and passed through another algorithm of charging/discharging control where the static PV firming algorithm is assumed to be applied. Based on this assumption, the PV energy is calculated and analyzed for each month to conclude with an average usable storage capacity.

First, since the data collected is for PV power, energy must be calculated as follows.

$$E_{PV} = P_{PV} \cdot t \quad (15)$$

where,

- E_{PV}: PV energy in watt-hour.
- P_{PV}: PV power in watt.
- t: time in hour.

In order to determine the average battery capacity for each month, the average PV energy ($\boldsymbol{E}_{PV,avg}$), maximum PV energy ($\boldsymbol{E}_{PV,max}$), and minimum PV energy ($\boldsymbol{E}_{PV,min}$) are calculated using equations (16) through (24).

Equation (16) defines the total average PV energy which is calculated by integrating the average energy for every minute ($E_{PV,avg}^{m_n}$) given in (17) and (18). $E_{PV,avg}^{m_n}$ is calculated by averaging the energy at that moment over one complete month.

$$\boldsymbol{E}_{PV,avg} = \int E_{PV,avg}(t)dt \quad (16)$$

$$E_{PV,avg}(t) = \left\{E_{avg}^{m_1}, E_{avg}^{m_2}, \dots, E_{avg}^{m_k}\right\} \quad (17)$$

$$E_{PV,avg}^{m_n} = \frac{\sum_{d_1}^{d_l}\left(E_{avg}^{m_n}(d_n)\right)}{l} \quad (18)$$

where,

- m_1, m_2, m_3 ... m_k: correspond to the minutes over a day.
- k: is equal to 1440, which is the total minutes in each day.
- d_1, d_2, d_3 ... d_l: correspond to the days over each month.
- l: is the last day of each month.
- $E_{PV,avg}^{m_n}$: is the PV energy at the nth minute averaged correspondingly over a month.

Similar method is applied for the maximum PV energy ($\boldsymbol{E}_{PV,max}$) and the minimum PV energy ($\boldsymbol{E}_{PV,min}$), as follows.

$$\boldsymbol{E}_{PV,max} = \int E_{PV,max}(t)dt \quad (19)$$

$$E_{PV,max}(t) = \left\{E_{PV,max}^{m_1}, E_{PV,max}^{m_2}, \dots, E_{PV,max}^{m_k}\right\} \quad (20)$$

$$E_{PV,max}^{m_n} = Max_{d_1}^{d_l}\left\{E_{PV,max}^{m_n}(d_n)\right\} \quad (21)$$

$$\boldsymbol{E}_{PV,min} = \int E_{PV,min}(t)dt \quad (22)$$

$$E_{PV,min}(t) = \left\{E_{PV,min}^{m_1}, E_{PV,min}^{m_2}, \dots, E_{PV,min}^{m_k}\right\} \quad (23)$$

$$E_{PV,min}^{m_n} = Min_{d_1}^{d_l}\left\{E_{PV,min}^{m_n}(d_n)\right\} \quad (24)$$

Examples are plotted in Figure 33 for two different months in 2016. The total average PV energy is around 3.2kWh in Feb, and around 2.7kWh in June. The rest of months are given in Appendix B.

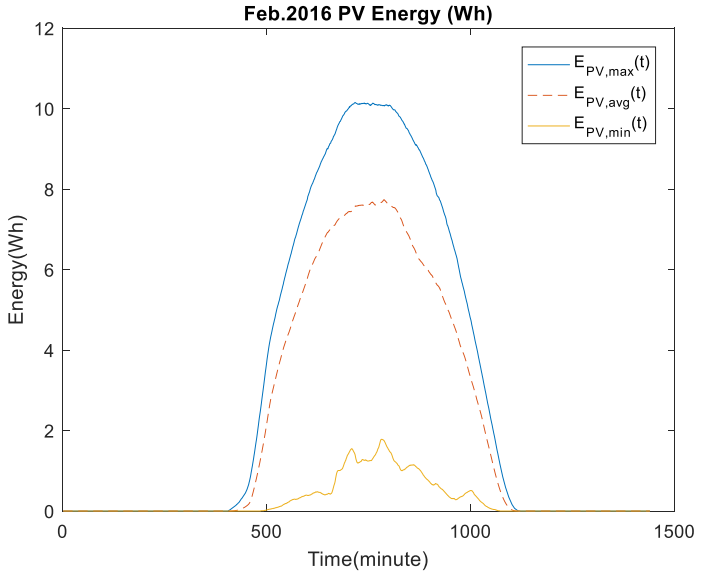

(a)

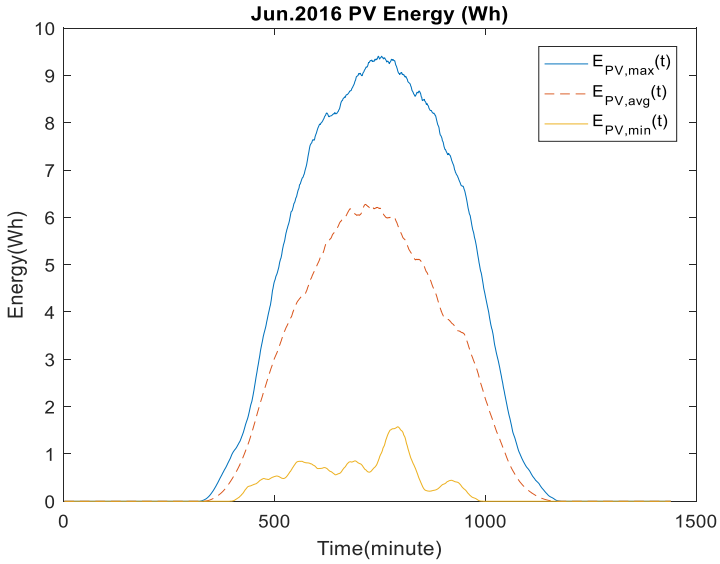

(b)

Figure 33: Average, maximum, and minimum PV energy for month of (a) Feb. 2016 and (b) Jun. 2016.

Now, the average usable storage capacity can be calculated where the PV output profile is statistically assumed to be firmed on the average PV power. Also, it is assumed to have both maximum and minimum energy on same day. So, the average PV energy curve ($E_{PV,avg}(t)$) as shown in Figure 33, is considered to be the PV firming reference power. The area between the maximum PV energy curve ($E_{PV,max}(t)$) and the $E_{PV,avg}(t)$ is considered to be the average surplus PV energy stored in the storage ($E_{PV,surplus}$). However, the area between the $E_{PV,avg}(t)$ and the minimum PV energy curve ($E_{PV,min}(t)$) is considered to be the average deficient PV energy taken from the storage ($E_{PV,deficient}$). The difference between $E_{PV,surplus}$ and $E_{PV,deficient}$ is defined to be the average usable storage (battery) capacity ($E_{bat,cap}$) needed to maintain the static PV firming output profile, which is given in (25).

$$E_{bat,cap} = \left|E_{PV,surplus} - E_{PV,deficient}\right| \quad (25)$$

where,

$$E_{PV,surplus} = \int E_{PV,max}(t)dt - \int E_{PV,avg}(t)dt = E_{PV,max} - E_{PV,avg} \quad (26)$$

$$E_{PV,deficient} = \int E_{PV,avg}(t)dt - \int E_{PV,min}(t)dt = E_{PV,avg} - E_{PV,min} \quad (27)$$

Figure 34 represents a summary for the analyzed average storage capacity that is assumed to be needed according to the data collected for each month.

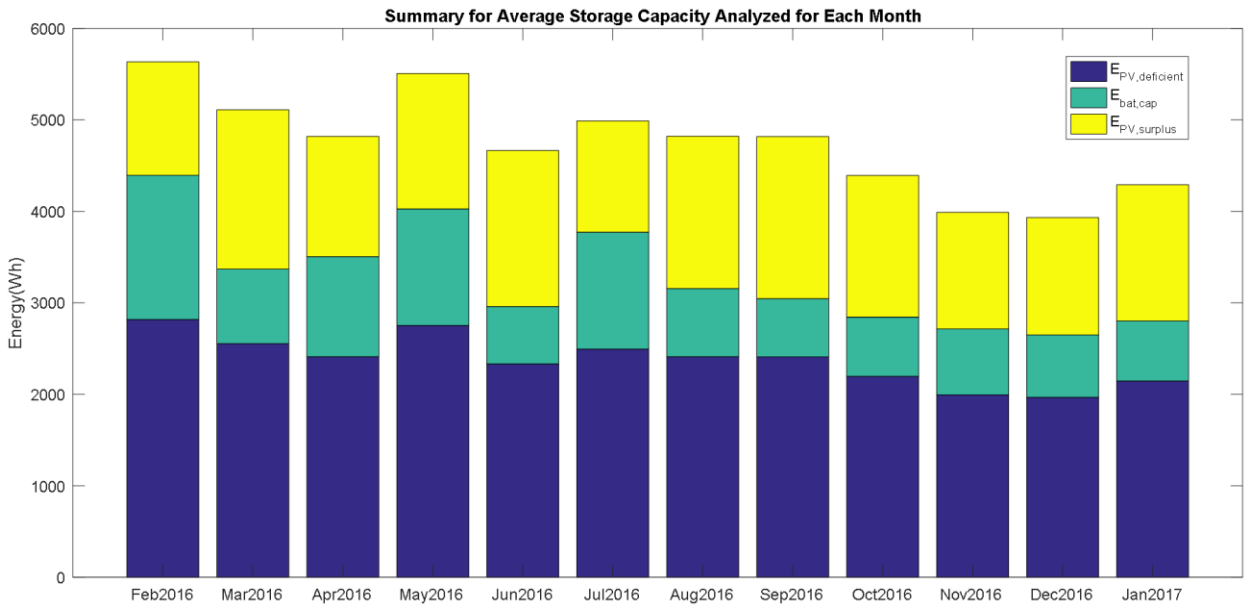

Figure 34: Analysis of PV and average storage capacities when the system is assumed to be firmed statically.

As a result of this analysis, the average usable storage capacity ranges between 628Wh (Jun. 2016) and 1.6kWh (Feb. 2016). If the static algorithm is implemented in reality, the average capacity of usable storage that would be integrated to a 600W system is around 1.6kWh. Therefore, the average nominal storage capacity would be up to 3.2kWh. However, under the worst case where only minimum PV energy is available, the actual usable storage capacity would be much larger than average, possibly as high as 3kWh (up to 6kWh nominal capacity of battery). This is an

obvious drawback of the static algorithm. Therefore, the dynamic PV firming algorithm is being proposed due to its many advantages.

3.7 Conclusions

A three-port microinverter topology and a static PV firming algorithm are proposed in this chapter. Batteries are seamlessly integrated with the flyback converter and H-bridge as a third port in the microinverter. All implemented controls regardless of the PV firming algorithms are discussed. A static PV reference power is generated first by the proposed method. Then, a charging/ discharging algorithm and other controls are implemented and discussed. A firmed power profile is generated in MATLAB/SIMULINK using the proposed algorithms. These algorithms are consequently validated experimentally. The experimental results show that the PV firming system can operate in charging and discharging modes while firming output power. The experimental results have some errors compared to the simulation results. The error is based on the power rates. It ranges between about 4.5% (around 200W power rate) and 13.7% (around 12W power rate). The DC-link (battery) voltage and current, and the inverter output current and voltage are as expected. The energy storage sizing is analyzed for the system when it depends on static PV reference for firming. This results in a nominal storage capacity reaching up to 6kWh for 600W system.

CHAPTER 4: DYNAMIC PV FIRMING ALGORITHM

4.1 Introduction

This chapter proposes a new dynamic PV firming algorithm using the same topology proposed in previous chapter. The main reason that this algorithm was developed is to optimize the storage capacity sizing. The results support the need for the dynamic PV firming algorithm. Section 4.2 presents the proposed dynamic PV firming system that consists of an algorithm for generating dynamic PV reference power and an algorithm for battery charging/discharging control. MATLAB/SIMULINK simulations are presented in Section 4.3, along with relevant waveforms. Section 4.4 shows an experimental validation of the proposed schemes.

4.2 Proposed Dynamic PV Firming System

4.2.1 Dynamic PV Reference Generation Algorithm

In the proposed dynamic PV reference generation algorithms, one static reference must be computed and coded. Several power levels are generated accordingly. By comparing the actual PV power to the power levels, the PV reference power is generated dynamically.

The dynamic reference generation algorithm depends on three main factors. The first factor is the maximum PV reference curve ($P_{ref,max}$) formulated in (9) and (10) which generates several power levels. It can be assumed as a map for the final generated reference power. It changes monthly based on the analysis of collected data at Central Florida (example) location [60]. The second factor is the fluctuation factor (*ls*). It controls the smoothness of the generated reference curve and determines the number of comparable power levels (No. of power levels = 1/ *ls*) as shown in Figure 35. In other words, the *ls* is indicative of the fluctuations/ smoothness rate. The lower the *ls,* the higher the number of comparing power levels. By increasing the number of power levels, the generated PV reference will have more rapid changes. This is because there are more power levels (references) needing to be tracked which results in decreased smoothness. Since the power level curves are generated by the $P_{ref,max}$, the only data saved in the memory is $P_{ref,max}$. The third factor is the slew rate factor (σ_f). It dampens the ramp rate of the PV actual power ($P_{PV,act}$) against abrupt changes, as well as contributing to the smoothness. In other words, the σ_f determines where the generated PV reference is located according to either the PV actual power change difference ($d(i)$) or the difference between the current $P_{PV,act}$ and the previous $P_{PV,ref}$ ($df(i)$). The σ_f is defined as a factor of a slope equation as in (28) or (29) for either the $d(i)$ or the $df(i)$, respectively.

$$\sigma_f P_{ref,max}(i) = \frac{d(i)}{\Delta t} \quad (28)$$

$$\sigma_f P_{ref,max}(i) = \frac{df(i)}{\Delta t} \quad (29)$$

$$d(i) = P_{PV,act}(i) - P_{PV,act}(i-1) \quad (30)$$

$$df(i) = P_{PV,act}(i) - P_{PV,ref}(i-1) \quad (31)$$

where,

- $d(i)$ is the PV actual power change difference as defined in (30).
- $df(i)$ is the difference between the current $P_{PV,act}$ and the previous $P_{PV,ref}$ as given in (31).
- Δt is the time difference and is assumed to be 1 minute since data changes every minute.
- $P_{PV,act}(i)$ is the current value of the actual PV power.
- $P_{PV,act}(i-1)$ is the previous value of the actual PV power.
- $P_{PV,ref}(i-1)$ is the previous value of the generated PV reference power.

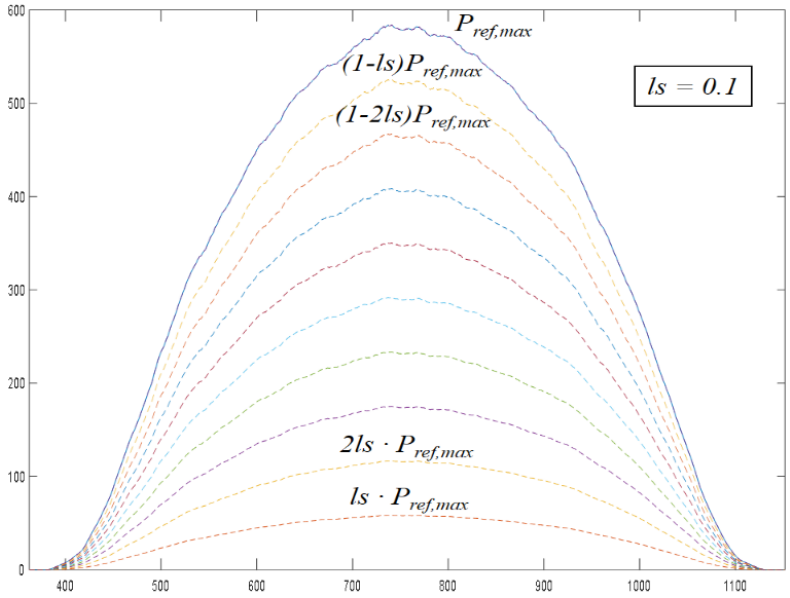

Figure 35: The maximum PV reference power with generated power levels.

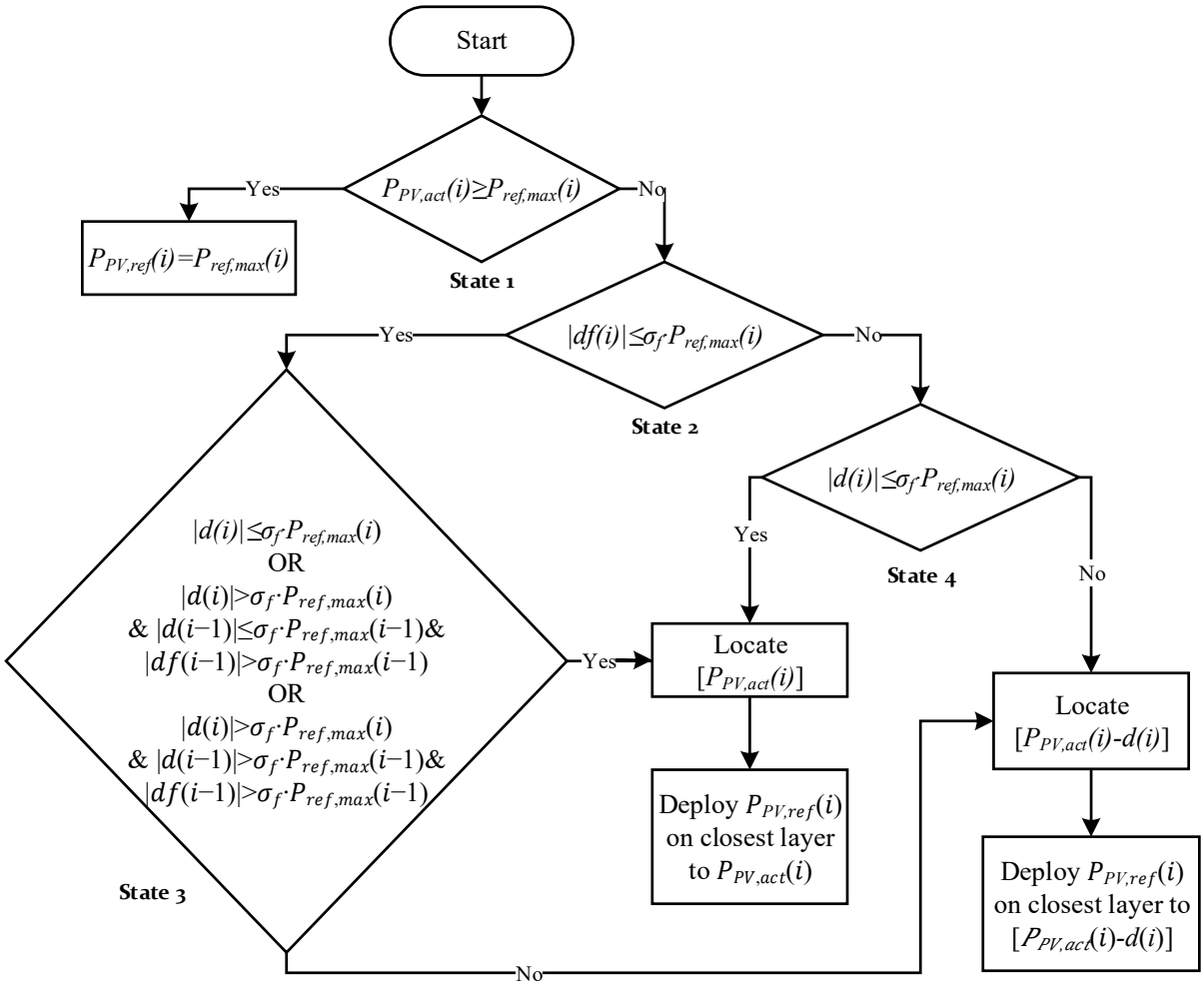

Figure 36: Proposed algorithm for dynamic PV reference power generation.

Figure 36 illustrates the flowchart for the dynamic $P_{PV,ref}$ generation algorithm. The algorithm begins by comparing the current value of the $P_{PV,act}(i)$ with $P_{ref,max}$, designated as state 1. If $P_{PV,act}(i)$ is greater than or equal to $P_{ref,max}$, the generated $P_{PV,ref}$ will be maintained to $P_{ref,max}$. State 2, state 3, and state 4 depend on two variables: the PV actual power change difference ($d(i)$)

in (29); and, the difference between the current $P_{PV,act}$ and the previous $P_{PV,ref}$, which is $df(i)$ in (30). First variable of $d(i)$ determines the ramp rate of the current PV actual power ($P_{PV,act}(i)$) compared to the previous PV actual power value ($P_{PV,act}(i-1)$). This is the actual power change per minute. It is named actual-actual ramp rate. The second variable of $df(i)$ determines the ramp rate of the $P_{PV,act}(i)$ compared to the previous PV generated reference power ($P_{PV,ref}(i-1)$). It is named actual-reference ramp rate. If $P_{PV,act}(i)$ is below $P_{ref,max}$, state 2 evaluates the fluctuation by comparing the absolute value of $df(i)$ to the maximum fluctuating value in the current time ($\sigma_f \cdot P_{ref,max}$). This process determines how the current PV power is ramped up/down compared to the previous PV firmed value. This shows how the actual-reference ramp rate is changing currently. If $|df(i)|$ is less than or equal to ($\sigma_f \cdot P_{ref,max}$), it means that it has low ramp rate. State 3 assures that the $P_{PV,act}$ is not fluctuating, by comparing $d(i)$ and $df(i)$ to ($\sigma_f \cdot P_{ref,max}(i)$) or ($\sigma_f \cdot P_{ref,max}(i-1)$). State 3 is used to ascertain that the $P_{PV,act}(i)$ is consistent. If state 2 is false, another comparison between *d(i)* and ($\sigma_f \cdot P_{ref,max}(i)$) is calculated to assure that the $P_{PV,act}(i)$ is not fluctuating as in state 4. If either state 3 or state 4 is true, the location of the $P_{PV,act}(i)$ is defined. Then, the generated $P_{PV,ref}$ is deployed on the closest power level to the current value of $P_{PV,act}$. If either state 3 or state 4 is false, which implies that the $P_{PV,act}$ has abrupt change (high slew rate), the location of the $[P_{PV,act}(i) - d(i)]$ is defined. Then, the generated $P_{PV,ref}$ is deployed on the closest power level to the current value of $[P_{PV,act}(i) - d(i)]$.

Figure 37 illustrates two examples of dynamic PV firming reference generation. They are intermittencies for two different days. In Figure 37 (a), the slew rate factor (σ_f) is equal to 0.03 which means that the generated PV reference power ($P_{PV,ref}$) ramps by 3% of the maximum PV reference power ($P_{ref,max}$) curve or less. The fluctuation factor (ls) is equal to 0.25 implying that there are 4 comparable power levels, where the output is as smooth as each power level. In Figure 37 (b), the $P_{PV,ref}$ ramps by 7% of the $P_{ref,max}$ curve or less. The PV actual power ($P_{PV,act}$) is being compared to 5 different power levels.

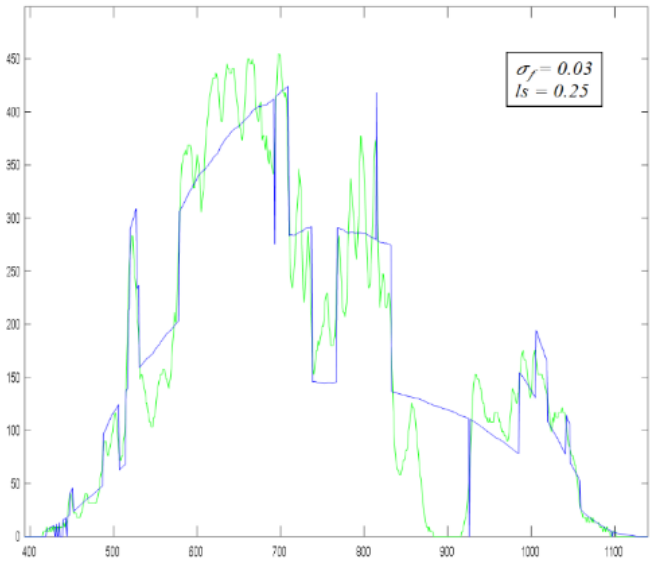

(a)

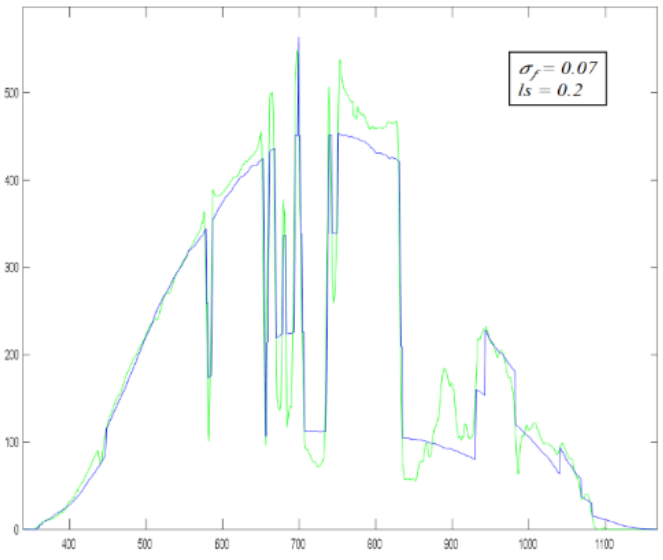

(b)

Figure 37: Generated PV firming reference for two different days.

4.2.2 Battery Charging/ Discharging Algorithm

As a second step in the PV firming process, the generated dynamic PV reference profile is used in another algorithm of PV firming battery charge/discharge control (see Figure 38) to produce the final power profile. This algorithm is identical to the PV-firming section in Figure 26 presented in Chapter 3.

ccc

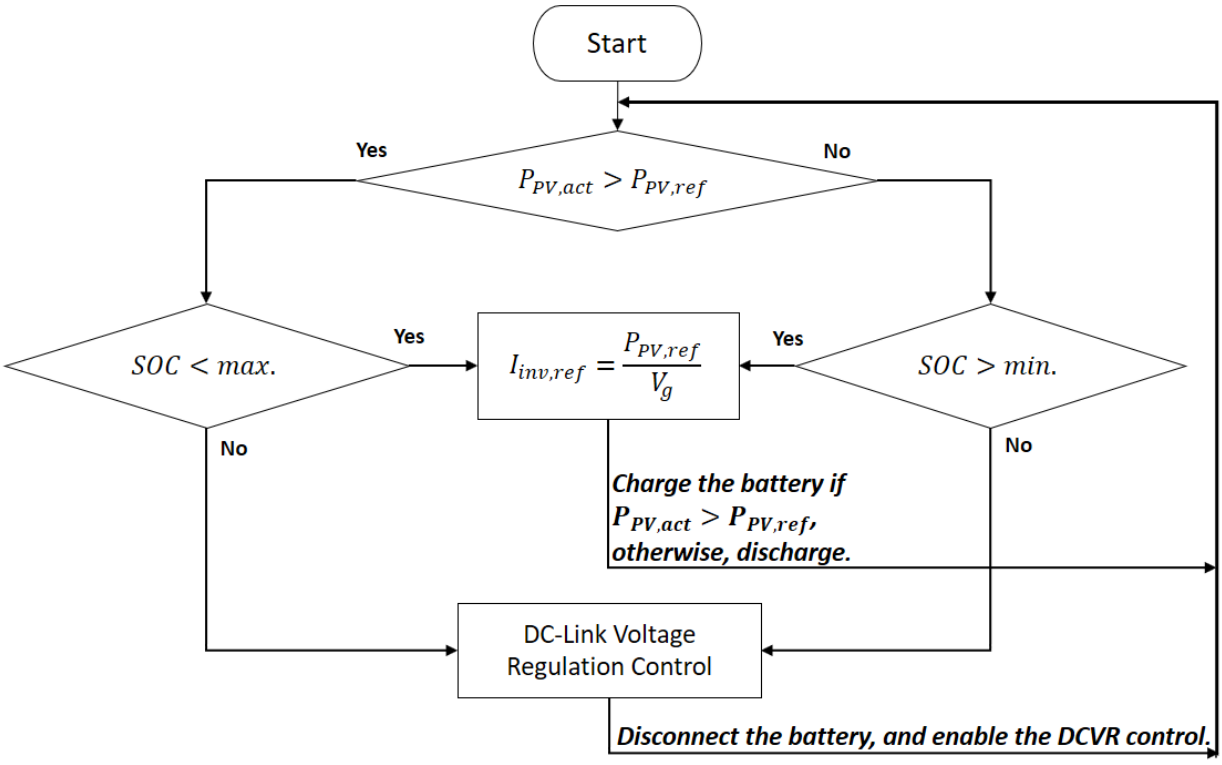

Figure 38: The algorithm flowchart for the PV firming battery charge/discharge control

4.3 Simulation Results

Simulations are carried out in MATLAB/Simulink to validate the proposed static PV-firming algorithm on the grid-tied two-stage battery-integrated topology shown earlier in Figure 18. Power waveforms for the PV actual power ($P_{PV,act}$), the inverter stage output power (P_{inv}), and the battery power (P_{bat}) for the dynamic PV firming microsystem are shown in Figure 39. While the simulation in MATLAB/Simulink takes a long time to perform the calculations, the timeline for

the waveforms is scaled down to 24 seconds. Thus, the rates of fluctuations are taken out of consideration. The battery power (P_{bat}) is either positive indicating that the battery is discharging power to the grid, or negative indicating that the battery is being charged from the PV. The DC-link voltage ($V_{dc-link}$), inverter output current (I_{inv}), and inverter reference RMS current ($I_{inv,ref}$) are as shown in Figure 40. The $V_{dc-link}$ is between 210V to 245V, which is the battery voltage. The $I_{inv,ref}$ is equal to the RMS value of the sinusoidal I_{inv}.

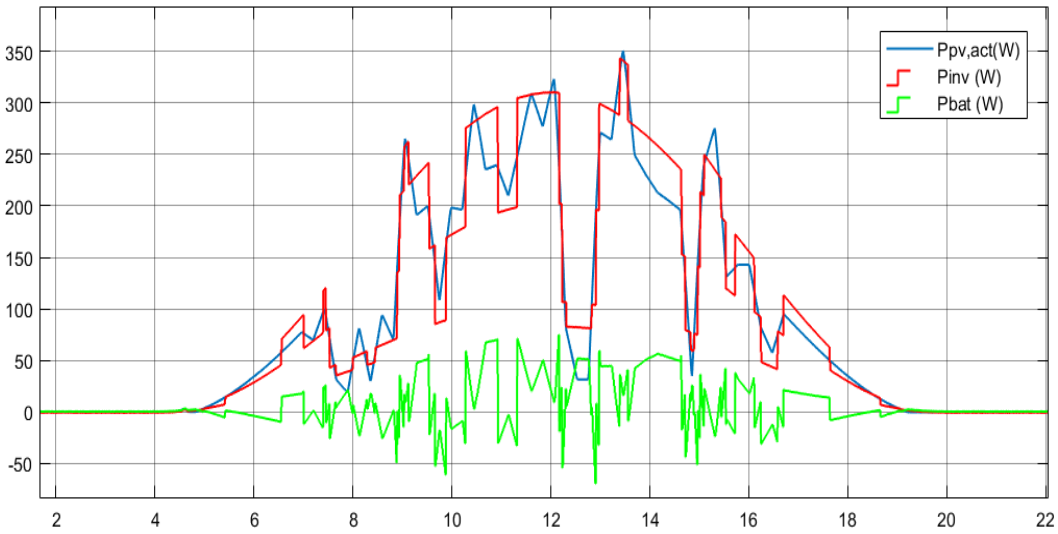

Figure 39: Power waveforms for PV actual (blue), firmed inverter output (red), and battery (green) for the dynamic firming microsystem.

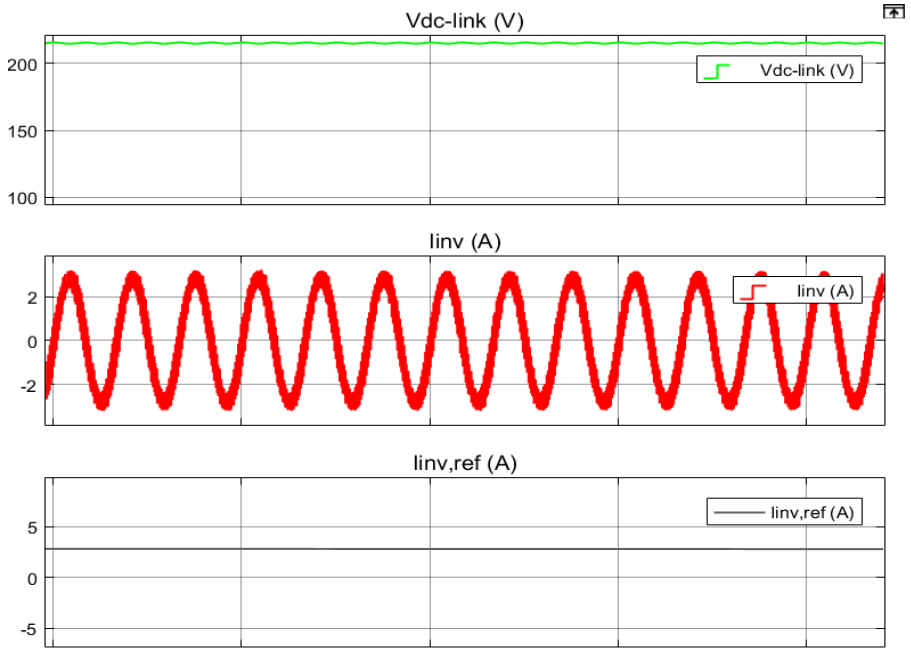

Figure 40: DC-link voltage (Vdc-link), inverter output current (Iinv), and inverter reference RMS current (Iinv,ref) waveforms.

4.4 Experimental Results

To experimentally verify the proposed static PV-firming control algorithm, a 200W prototype is built with specifications as shown in Table 5 in Section 3.5. The same prototype test set-up as in the static algorithm experiment is applied.

Figure 41 shows the experimental voltage and current waveforms for the PV output power, inverter output power (firmed), and the battery power while charging and discharging for the dynamic PV firming system. The timeline for the waveforms is scaled down to around half an hour. So, the

rates of fluctuations have been out of consideration. Since the $P_{PV,act}$ (blue curve) has been changed manually using the Solar Array Simulator, the PV output power curve does not demonstrate as many fluctuations as it would with real-time power. However, the charging/discharging control algorithm is verified since the P_{inv} (yellow) is following the generated PV reference power. The P_{bat} is positive when the battery is discharging power to the grid and the $P_{PV,act}$ is greater than the generated PV reference. The P_{bat} is negative when the battery is being charged from the PV and the $P_{PV,act}$ is less than the generated PV reference. Figure 42 shows experimental waveforms of the grid voltage (V_g), DC-link (battery) voltage ($V_{dc-link}$) along with inverter output current (I_{inv}) and battery current (I_{bat}) while the battery is being charged. Figure 43 shows the same waveforms while the battery is being discharged. Note that the positive battery current (I_{bat}) implies that the battery is being charged and similarly negative implies that battery is being discharged. The average value of $V_{dc-link}$ is about 236V in Figure 42 and 234V in Figure 43, which are in the target range of the battery voltage. The V_g and I_{inv} are sinusoidal as expected.

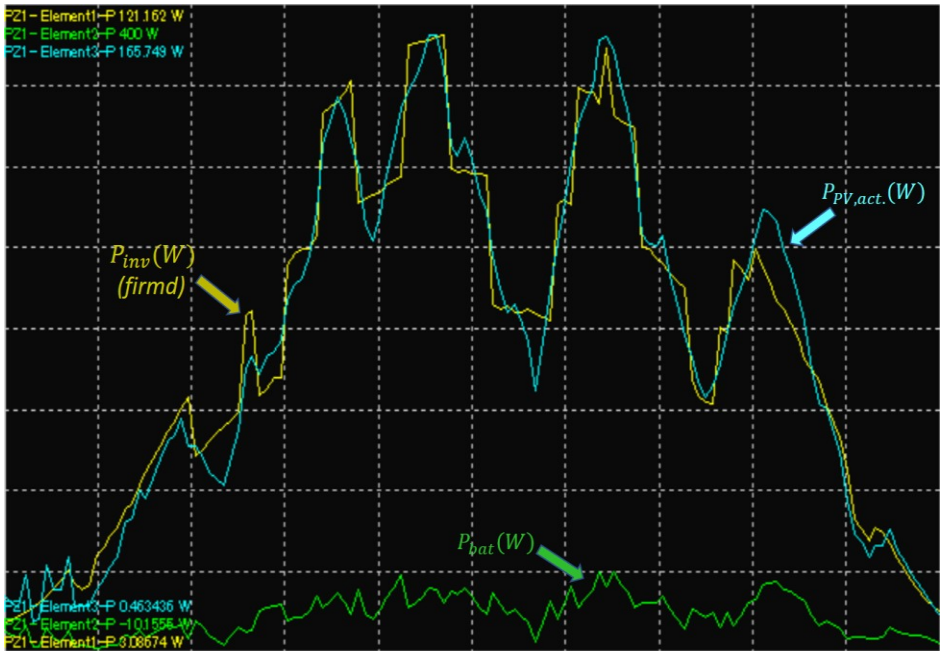

Figure 41: Power waveforms for PV actual, inverter output (firmed), and battery for static firming.

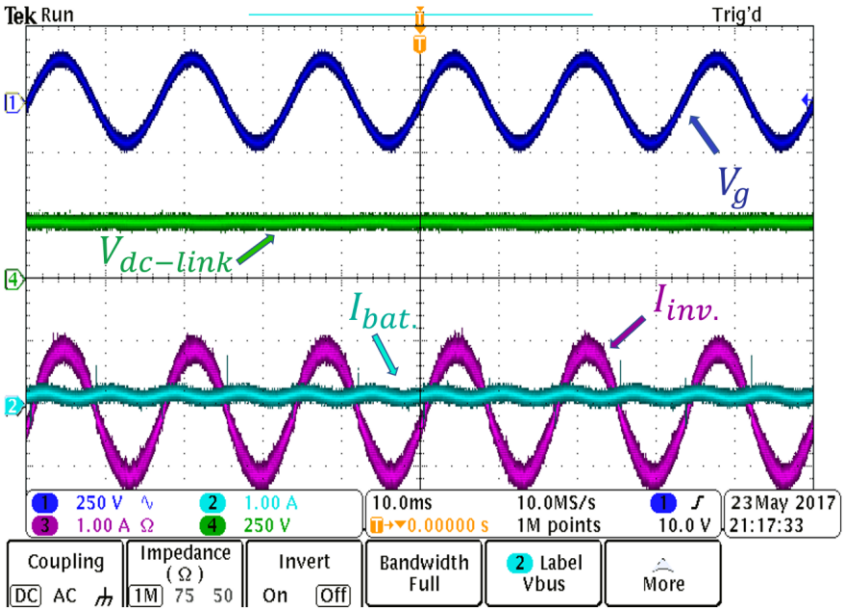

Figure 42: Grid voltage (V_g), DC-link voltage ($V_{dc\text{-}link}$), inverter output current (I_{inv}), and battery current (I_{bat}) waveforms while the battery is being charged.

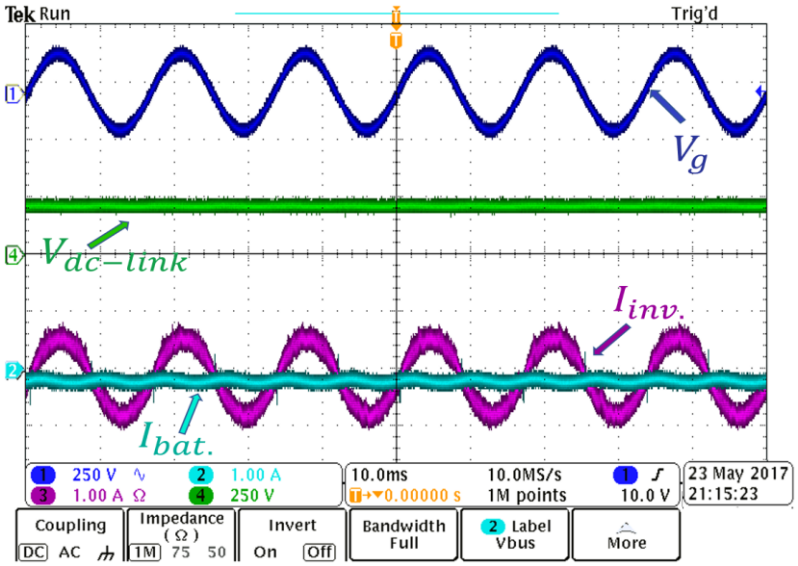

Figure 43: Grid voltage (V_g), DC-link voltage ($V_{dc\text{-}link}$), inverter output current (I_{inv}), and battery current (I_{bat}) waveforms while the battery is being discharged.

4.5 Storage Capacity Sizing Analysis for the Dynamic PV Reference

For the dynamic PV firming, the main factor that can determine the storage capacity sizing is the fluctuation factor (ls). Therefore, in addition to controlling the smoothness of the output power profile, there are other relationships between the number of power levels or the fluctuation factor (ls) and the usable storage capacity ($E_{bat,cap}$), the surplus PV energy to be stored in the storage ($E_{PV,surplus}$), and the deficient PV energy ($E_{PV,deficient}$). An example for analysis and discussion is presented in Figure 44.

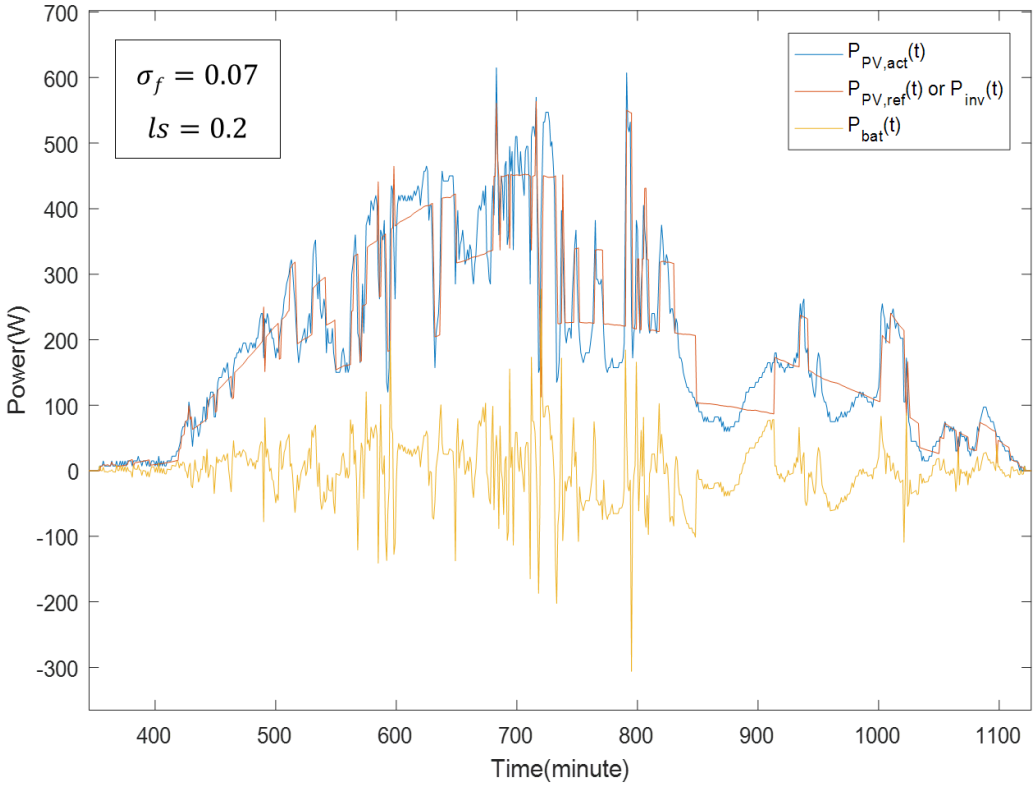

Figure 44: Power waveforms of PV actual (blue), PV reference/ firmed inverter output (red), and battery (orange), such an example for a day in May 2016.

Initially, the slew rate factor (σ_f) must be fixed while the ls is being changed. Then, for every adjustment of ls, the $E_{bat,cap}$, the $E_{PV,surplus}$, and the $E_{PV,deficient}$ need to be calculated. There are two different methods for calculating these energies.

The first method is to determine the difference between the PV actual power ($P_{PV,act}$) and the generated PV reference power ($P_{PV,ref}$) for every minute that $P_{PV,act}$ is greater/ less than $P_{PV,ref}$.

The results are calculated in total to determine the energy. When $P_{PV,act}$ is greater than $P_{PV,ref}$, the $E_{PV,surplus}$ is resulted. Otherwise, it results the $E_{PV,deficient}$. The following equations represent the calculations for this method.

$$E_{PV,surplus} = \left[\sum_t P_{PV,act}(t)\,\delta t - \sum_t P_{PV,ref}(t)\,\delta t\right], \qquad P_{PV,act} > P_{PV,ref} \qquad (32)$$

$$E_{PV,deficient} = \left[\sum_t P_{PV,ref}(t)\,\delta t - \sum_t P_{PV,act}(t)\,\delta t\right], \quad P_{PV,ref} > P_{PV,act} \qquad (33)$$

The $E_{bat,cap}$ is determined in (24).

The other method is to calculate the total positive and negative values for the battery power (P_{bat}), where P_{bat} is the difference between $P_{PV,act}$ and $P_{PV,ref}$.

$$E_{PV,surplus} = \sum_t P_{bat}(t)\,\delta t, \qquad P_{bat} > 0 \qquad (34)$$

$$E_{PV,deficient} = -\sum_t P_{bat}(t)\,\delta t, \qquad P_{bat} < 0 \qquad (35)$$

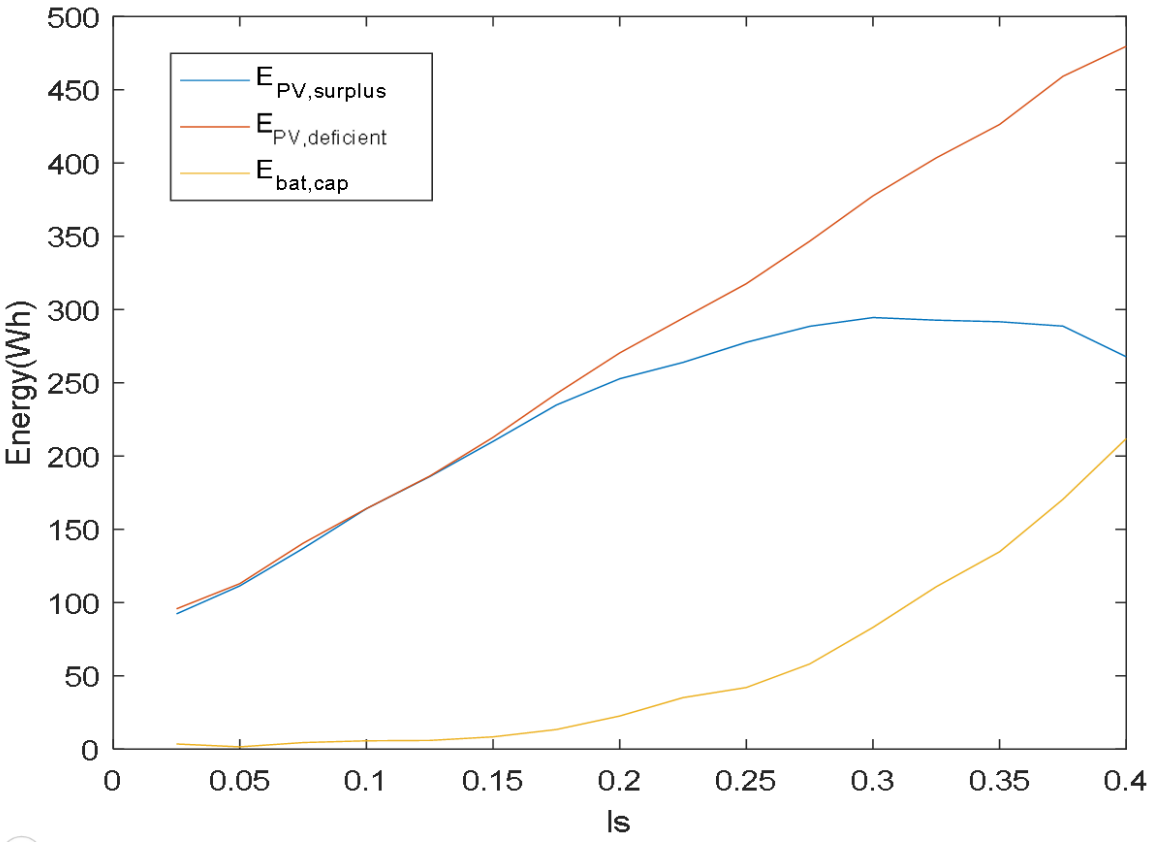

Figure 45: Analysis of PV and usable storage capacities when the system is firmed dynamically.

As shown in Figure 45, the fluctuation factor (*ls*) or the number of power levels (1/ *ls*) has an obvious effect on the energy capacity of the storage. The relationship of the surplus PV energy ($E_{PV,surplus}$) and the deficient PV energy ($E_{PV,deficient}$) to the *ls* seems linear until the *ls* is equal to about 0.15, or there are about 7 comparable power levels. Thus, the usable storage capacity ($E_{bat,cap}$) would have similar proportionality. Once the number of power levels decreases, or the *ls* increases after that point, the $E_{PV,surplus}$ starts decreasing gradually with respect to the *ls* while

the $E_{PV,deficient}$ continues increasing linearly. Therefore, the $E_{bat,cap}$ will be enlarged since the PV energy is becoming much less sufficient. However, although decreasing the fluctuation factor (ls) (increasing the number of power levels) minimizes the storage capacity, it affects the smoothness negatively. As a result of this analysis, the storage capacity size can range from below 50Wh to above 200Wh (100Wh to 400Wh - nominal capacity value).

Figure 46 and Figure 47 illustrate the power waveforms for the example shown in Figure 44. Here, the fluctuation rate is decreased by increasing the fluctuation factor (ls). So, the conclusion is that the *ls* makes a trade-off between the fluctuation rates and the storage capacity sizing.

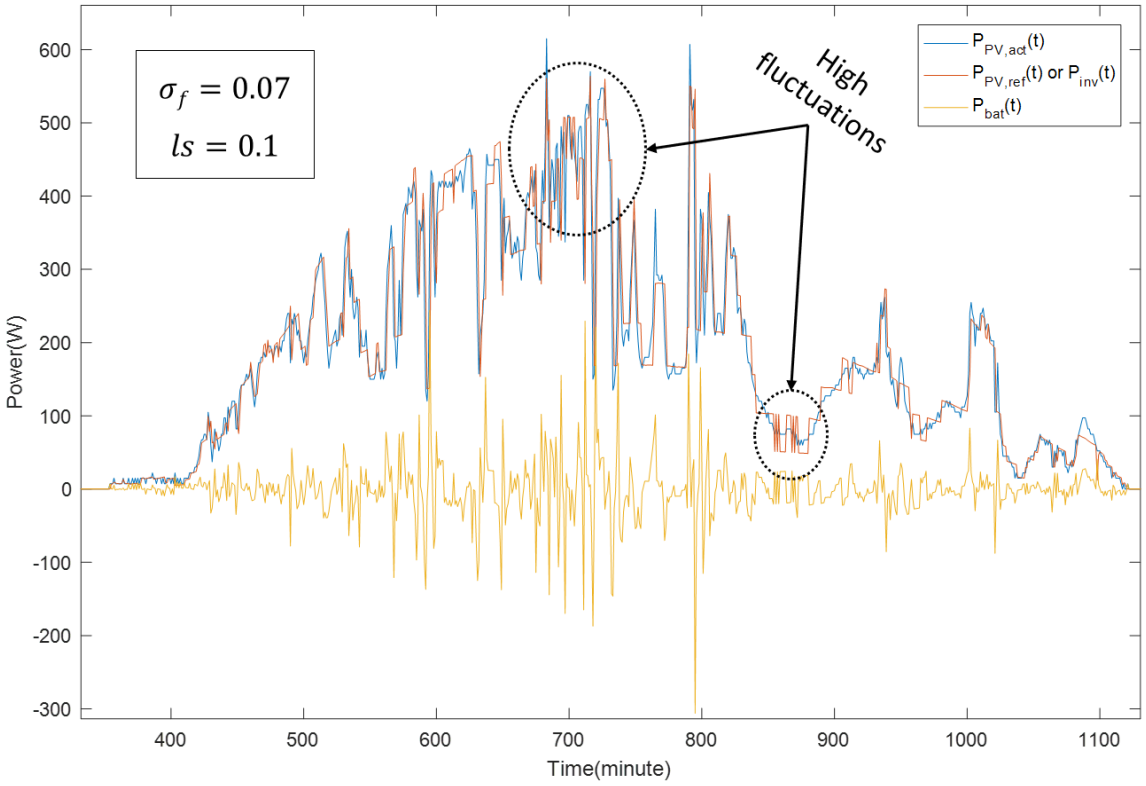

Figure 46: Power waveforms for same example shown in Figure 44 but with different fluctuation factor (*ls*=0.1).

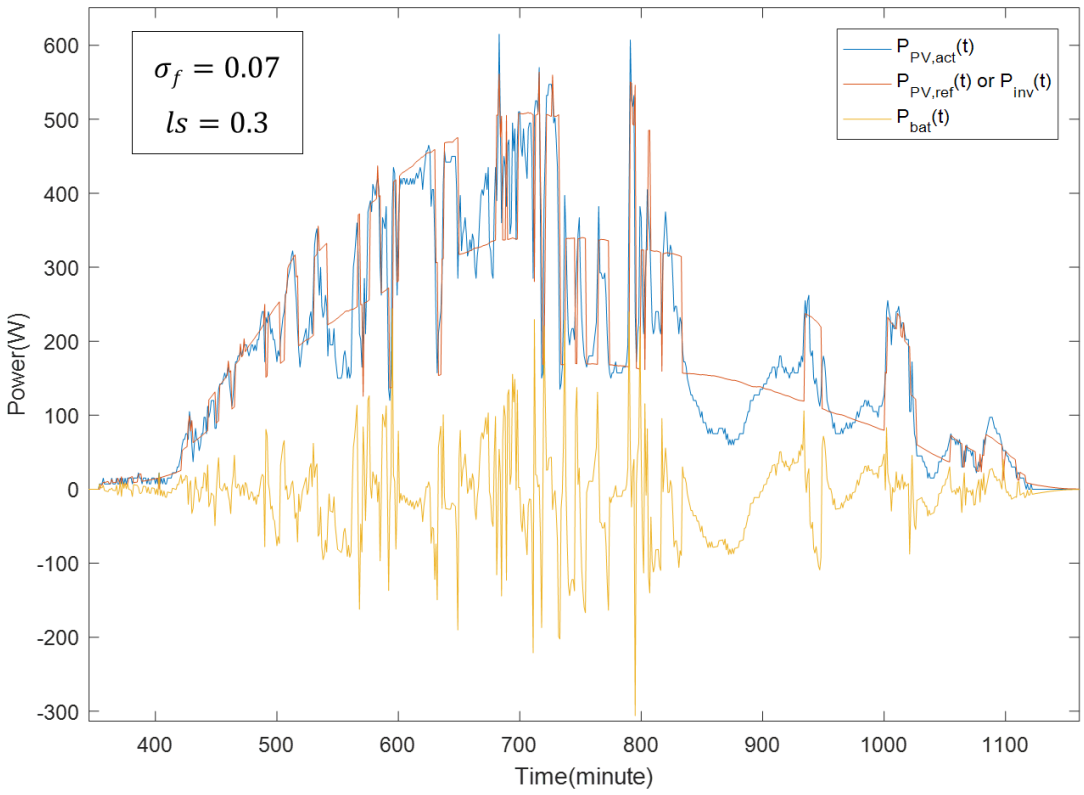

c

Figure 47: Power waveforms for same example shown in Figure 28 but with different fluctuation factor (*ls*=0.3)).

4.6 Conclusions

Algorithms and analysis for a dynamic PV firming microsystem are proposed using a three-port microinverter topology in this chapter. Batteries are seamlessly integrated with the flyback converter and H-bridge inverter as a third port in the microinverter. According to the analysis results for storage capacity sizing when the static algorithm is applied, the value of this novel dynamic PV reference generation algorithm for PV firming is supported. As a first step, a static

PV maximum reference power is generated by the proposed method in chapter 3. Then, from that reference, several power levels are assumed to generate final dynamic PV reference. This results in an output power profile that can demonstrates minimal ramp-rate and reduced storage capacity. In the final step of PV firming, the output of the dynamic PV reference generation algorithm becomes an input of the charging/discharging algorithm to control the battery power. A PV firmed power profile is generated first in MATLAB/ SIMULINK using the proposed algorithms which are also validated experimentally. The experimental results show that the PV firming system can operate in charging and discharging modes while firming output power. The experimental results have some errors compared to the simulation results. The error is based on the power rates. It ranges between about 4.5% (around 200W power rate) and 13.7% (around 12W power rate). The DC-link (battery) voltage and current, and the inverter output current and voltage are as expected. Finally, the sizing of the storage capacity is analyzed for the system when it depends on dynamic PV reference for firming. This results in a nominal storage capacity changing form about 100Wh to 400Wh for 600W system.

CHAPTER 5: DUAL OPTIMIZATION FOR THE INVERTION STAGE

5.1 Introduction

The H-bridge sinusoidal pulse-width modulation (SPWM) inverter is immensely used in numerous applications such as grid-tied PV inverters [61], [61], [62], [62], and [63], uninterruptible power supplies (UPS) [64], motor drives [65], [66], and active filters [67]. There are strict standards of the permissible amount of harmonics that an inverter is allowed to generate in many of these applications [68], [69]. Also, the high frequency SPWM is currently the most vastly used technique to control the switches of the H-bridge inverter. The switching frequencies that are employed in the SPWM must be well above the fundamental frequency. Although the switching loss in the inverter is proportional to switching frequency, inductor DC loss and devices conduction losses are proportional to the load power [70], [71].

The efficiency and the power quality of the SPWM full-bridge inverter can be improved without modifying any component in the hardware. Varying the switching frequency over the fundamental cycle is one way to increase the efficiency and optimize the power quality. A hysteresis current controller for inverters is one such scheme of variable switching frequency methods that can decrease the switching loss of the high current ripple area [72]. In [73], a variable switching frequency scheme within a fundamental period is implemented to minimize the switching loss while meeting the requirements of the total harmonic distortion (THD). Another method involves doubling the switching frequency during the time when the ripple has increased [74]. Several

techniques of frequency tracking have been implemented in [75], [76], and [77] to optimize the efficiency for different power conversion systems.

In this chapter, two algorithms to optimize the efficiency and the current THD for a conventional, hard-switching H-bridge SPWM microinverter are proposed. Two different approaches are discussed; dual tracking of optimum efficiency and THD algorithm, and perturbing and observing the switching frequency while maintaining the minimum current THD for different loads. An optimal switching frequency is proposed based on analysis of averaged loss power and THD over a fundamental period for several loads. Section 5.2 presents an analysis of averaged total loss modeling and calculation for the H-bridge SPWM microinverter. In Section 5.3, the proposed algorithms for tracking the optimum switching frequency are presented. Section 5.4 shows the experimental verifications followed by conclusions in Section 5.5.

5.2 Loss Modeling and Calculation

To accurately calculate the efficiency, all losses of both active and passive devices must be calculated. As shown in Figure 48, there are eight active devices and three passive components where each switch is driven by a single device. The left-side leg of the H-bridge microinverter, which consists of Q1, Q3, D1, D2, D3, and D4, operates at high switching frequency (f_s). The right-side leg, which consists of Q2 and Q4, operates at frequencies as low as the fundamental frequency (f).

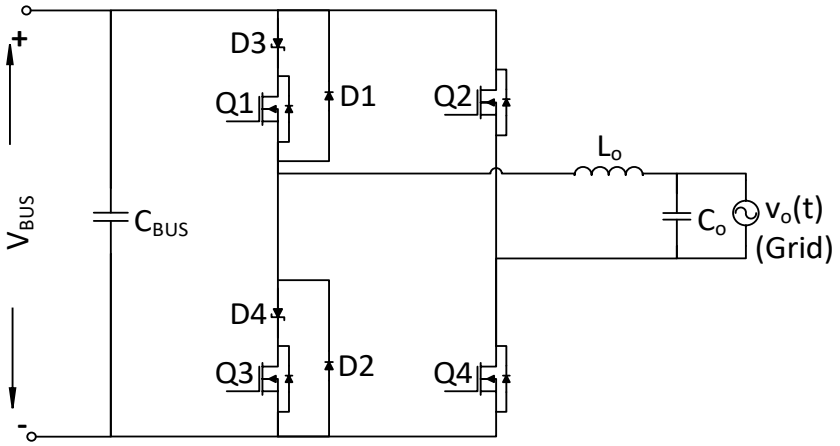

Figure 48: H-bridge microinverter topology.

Because the objective is to analyze the switching frequency, the only passive component that will be considered in the calculation is the output filter inductor (L_o). According to the modes of operation for the H-bridge inverter shown in Figure 49, both positive and negative half cycles have same losses since they run using the same type and number of devices and components.

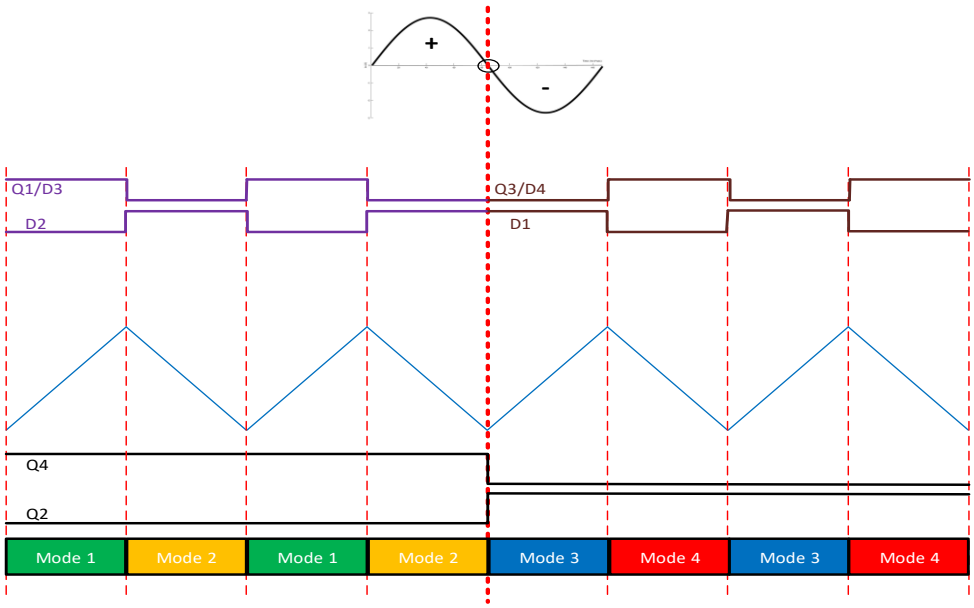
+
-
Q1/D3
D2
Q3/D4
D1
Q4
Q2
Mode 1
Mode 2
Mode 1
Mode 2
Mode 3
Mode 4
Mode 3
Mode 4

(a)

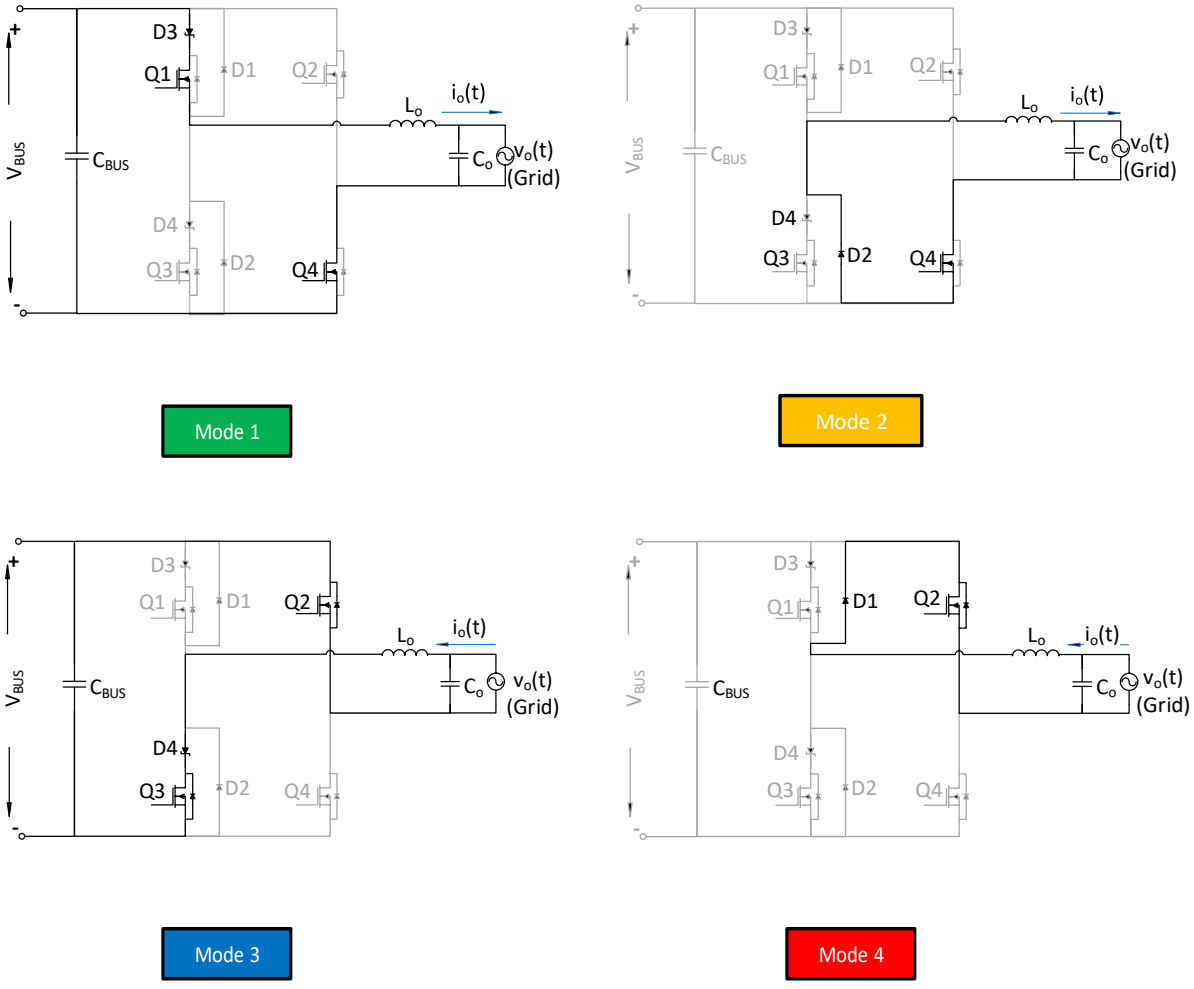

(b)

Figure 49: (a) Modes of operation waveforms. (b) Modes of operation circuits diagram.

So, calculating the losses during the positive half cycle only will provide adequate results. Equation (35) represents the total instantaneous loss ($P_{loss_{total}}$) as a function of time. According

to (36), there are three types of losses, namely: inductor losses, conduction losses, and switching losses. $P_{L_{DC}}$ and $P_{L_{core}}$ are defined as inductor DC and core losses, respectively. The conduction losses are distributed among the two operation modes of the SPWM topology, where $P_{Q1_{con}}$ and $P_{D3_{con}}$ are when pair Q1/D3 devices are conducting and $P'_{D2_{con}}$ and $P'_{Q4_{con}}$ are when pair Q4/D2 devices are conducting. $P_{Q1_{sw}}$and $P_{Q4_{sw}}$ are defined as the switching losses for Q1 and Q4, respectively. Power losses equations and details are discussed in Appendix C.

$$P_{loss_{total}}(t) = P_{L_{DC}}(t) + P_{L_{core}} + P_{Q1_{con}}(t) + P_{D3_{con}}(t) + P'_{D2_{con}}(t)$$

$$+P'_{Q4_{con}}(t) + P_{Q1_{sw}}(t) + P_{Q4_{sw}}(t) \quad (36)$$

The instantaneous and averaged efficiencies are given in (37) and (38), respectively, where P_o is the average output power.

$$\eta(t) = \frac{P_o - P_{loss_{total}}(t)}{P_o} \times 100\% \quad (37)$$

$$\boldsymbol{\eta} = \frac{2}{T}\int_0^{T/2} \eta(t)\, dt \quad (38)$$

Figure 50 presents the results for the power losses in percentage for the microinverter when the switching frequency is 20kHz. The total switching loss percentage for this value of switching frequency is 32%. This supports the need for proposing switching frequency tracking algorithm.

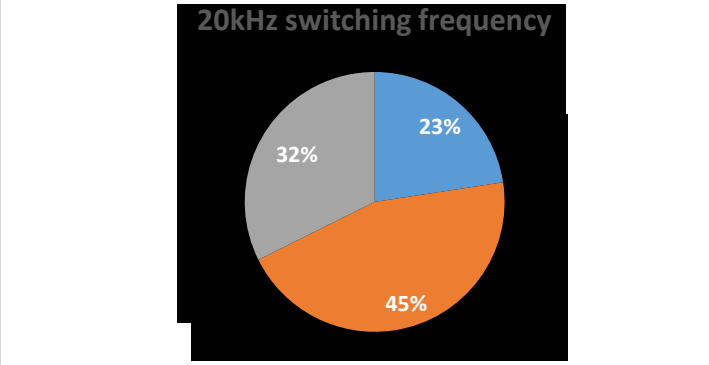

Figure 50: Power losses in percentage for the microinverter when the switching frequency is 20kHz.

5.3 Optimal Switching Frequency Tracking Algorithms

Both the THD and the efficiency are calculated by the microcontroller in order to implement the proposed algorithms. There are two different approaches to optimize the H-bridge microinverter used for the PV microinverter. One approach is to track the optimal switching frequency for maximum efficiency under a certain THD. The other approach is to optimize the power quality of the H-bridge microinverter by tracking the THD as a function of switching frequency.

5.3.1 THD and Efficiency

THD is a commonly used parameter for evaluating the power quality and performance of many power conversion systems, such as uninterruptable power supply (UPS), grid-tied inverters, etc. For a system that has a THD-based control strategy, low complexity and continuous measurement of THD is required without interrupting the main operation of the microcontroller. A common method of measuring the THD is by using the quasi-synchronous sampling algorithm [78]. The periodic current signal can be expressed as trigonometric Fourier series as in (39), where (40) and (41) are the Fourier coefficients, and the n^{th} harmonic term and the phase angle of each term (fundamental and other harmonics) are expressed in (42) and (43).

$$i(t) = \frac{I_{a0}}{2} + \sum_{n=1}^{\infty}(i_{an}\cos(n\omega t) + i_{bn}\sin(n\omega t)) \quad (39)$$

$$i_{an} = \sqrt{2}I_n \sin\varphi_{in} \quad (40)$$

$$i_{bn} = \sqrt{2}I_n \cos\varphi_{in} \quad (41)$$

$$I_n = \frac{1}{\sqrt{2}}i_{cn} = \sqrt{\frac{i_{an}^2 + i_{bn}^2}{2}} \quad (42)$$

$$\varphi_{in} = \tan^{-1}\frac{i_{an}}{i_{bn}} \quad (43)$$

So, the fundamental current and current of other harmonics can be expressed as:

$$I_n(t) = i_{cn}\sin(n\omega t + \varphi_{in}) = i_{an}\cos(n\omega t) + i_{bn}\sin(n\omega t) \quad (44)$$

The total harmonic distortion is defined as:

$$THD_i = \frac{\sqrt{\sum_{n=2}^{N} I_n^2}}{I_1} \times 100\% \quad (45)$$

The efficiency is measured by averaging the input and the output power of the H-bridge microinverter by monitoring the sampled signals for input and output currents and voltages. The averaged sampled power over one line period is expressed in (46).

$$\bar{P} = \frac{1}{T}\sum_{t=0}^{T} i(t) \cdot v(t) \quad (46)$$

where

$$\begin{cases} i(t) = I_{pk}\sin\omega t \\ v(t) = V_{pk}\sin\omega t \end{cases} \quad (47)$$

So, the efficiency is expressed as

$$\eta = \frac{\overline{P_o}}{\overline{P_{in}}} \times 100\% \quad (48)$$

where $\overline{P_o}$ and $\overline{P_{in}}$ are the averaged sampled output and input powers over one line period, respectively.

5.3.2 Approach 1: Dual Tracking of Optimum Efficiency and THD Algorithm

The optimal switching frequency is tracked using the search algorithm shown in Figure 51. This algorithm optimizes the power quality and the efficiency of the H-bridge microinverter for switching frequencies between 10 kHz and 100 kHz. The algorithm starts by setting the initial switching frequency at 10 kHz for the current line cycle ($f_{s,k}$), and setting the first step value of the switching frequency (f_{step}) at 1 kHz, and the line cycle step (k) at zero. Next, the maximum required value for the percentage THD (α), which varies with different applications, is set at a certain value (for example, α=2%). By monitoring the input and output voltages and currents, the THD and efficiency (η) are calculated using the microcontroller, and the switching frequency is incremented every one complete cycle with a predetermined step size (μ).

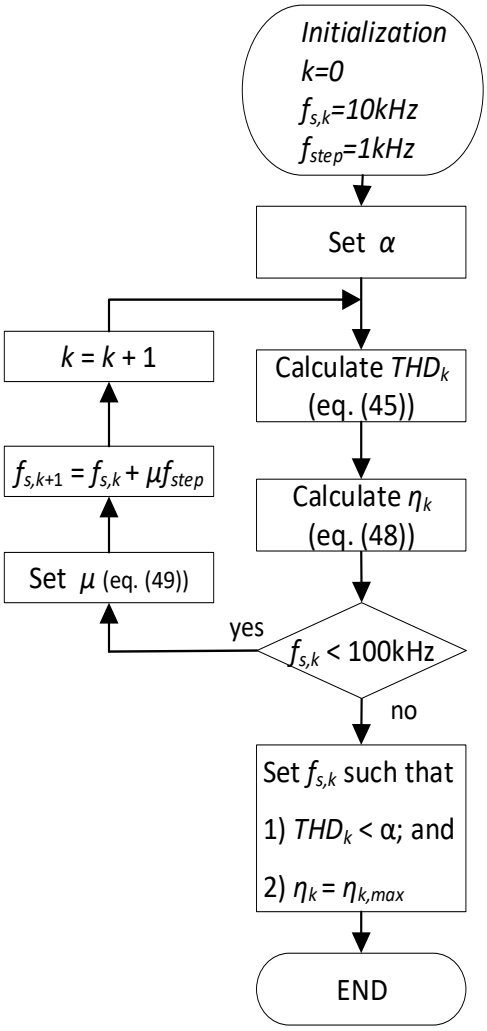

Figure 51: Proposed algorithm for dual tracking of optimum efficiency and THD values for the H-bridge SPWM inverter (Approach 1).

The step size (μ) determines the incrementing value of the switching frequency and the convergence speed. For example, if μ=2, the algorithm will need 46 iterations to calculate the THD and efficiency (10kHz, 12kHz, 14kHz, …, 100kHz). Here, two different values of μ are chosen

for two different zones according to the THD analysis. These two values are given in (49). A small μ is chosen for zone 1 where the rate of change between the THD and the switching frequency is large, while in zone 2 the rate of change is low and hence a large μ is chosen, as shown in Figure 52.

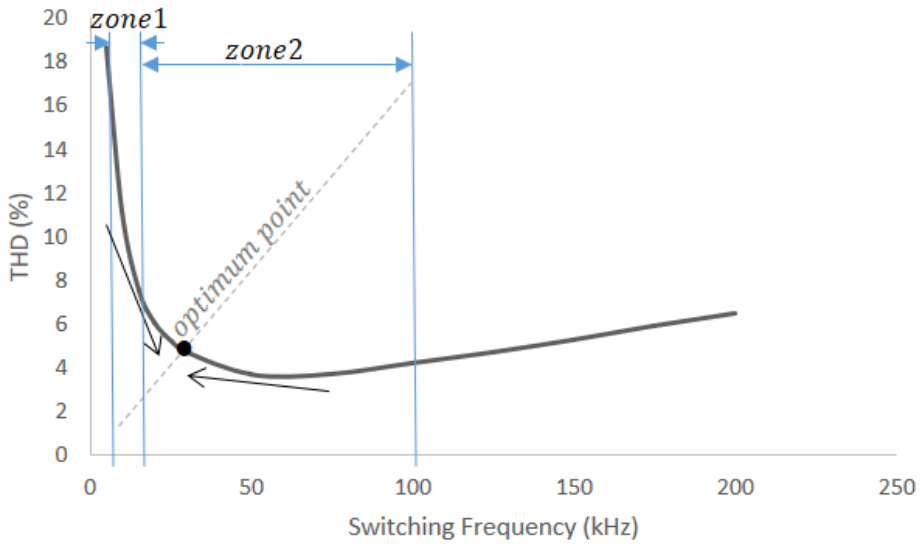

Figure 52: Switching frequency zones and optimum THD point.

$$\begin{cases} 10kHz \leq f_{s,k} < 20kHz, \Longrightarrow \mu = 2.5 & (zone1) \\ 20kHz \leq f_{s,k} < 100kHz, \Longrightarrow \mu = 5 & (zone2) \end{cases} \quad (49)$$

5.3.3 Approach 2; Minimum THD Point Tracking Algorithm

The minimum THD point tracking, i.e. $THD_{min} = \alpha_{min}$, is an algorithm implemented in the inverter to continuously adjust the impedance seen by the microinverter output filter to keep the microinverter output current delivering with, or close to, the minimum THD point under varying loads. Figure 53 illustrates the algorithm flowchart.

This algorithm perturbs the switching frequency to ensure that the system operates at minimum THD point (optimum point) on the THD curve, as shown in Figure 52.

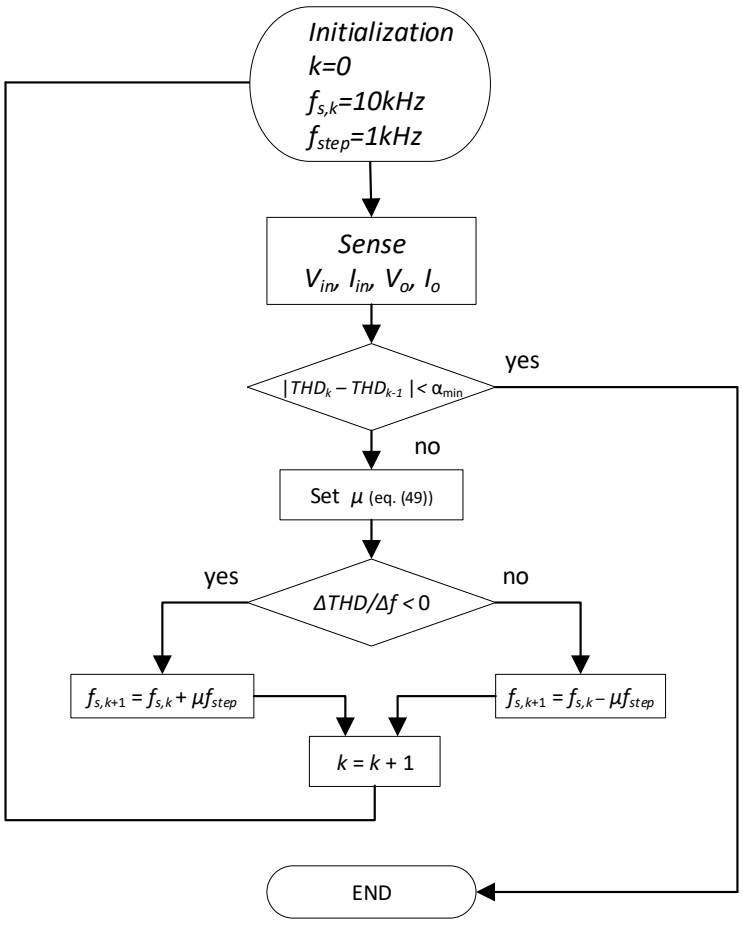

Figure 53: Minimum THD point tracking algorithm (Approach 2).

In Figure 53, the algorithm starts by initializing the switching frequency and sensing the input/output voltage and current to calculate the THD. If the absolute value of the change in the THD between two successive iterations is below a minimum predefined value α_{min}, e.g. α_{min}=1%, the algorithm terminates and the THD is considered minimum at that switching frequency. If the absolute value of the change is above α_{min}, a value of μ is selected in a similar fashion as in the algorithm in Figure 51. Based on the slope sign of the THD-switching frequency curve, the

frequency is incremented or decremented. The process only terminates if the variation in the THD becomes below α_{min}. One remark on the approach is that by increasing the frequency resolution, i.e. decreasing the step size, the value of α_{min} can be decreased and hence the algorithm becomes more accurate. However, increasing the frequency resolution will reduce the speed of the algorithm. For the frequency resolution in this research, which is 2.5 kHz (zone 1) or 5 kHz (zone 2), a value of 1% for α_{min} is found to be adequate.

5.4 Experimental Results

The DC/AC inverter stage (H-bridge) of the same prototype (200 W microinverter) used previously for the PV-firming algorithms is used to validate the proposed techniques experimentally, where the prototype specifications are shown in Table 5. Both efficiency and power quality (THD) were measured as functions of both switching frequency and power rate. Figure 54 illustrates the efficiency in terms of switching frequency for different power rates. Noticeably, at high frequency, the efficiency is inversely proportional to the switching frequency due to the high switching losses. Figure 55 illustrates the dependence of the THD on the switching frequency at different power rates. The THD seems to have exponential relationship with the switching frequency. Noticeably, the relationship between the efficiency as a function of switching frequency and the load value shown (Figure 54) is nonlinear. Also, despite the linear relationship between the THD and the load value at high frequencies (Figure 55), an almost parabolic curve is shown for the THD as a function of switching frequency for a frequency range between 10 kHz

and 200 kHz. Hence, both the efficiency and the THD can be optimized by varying the switching frequency as demonstrated.

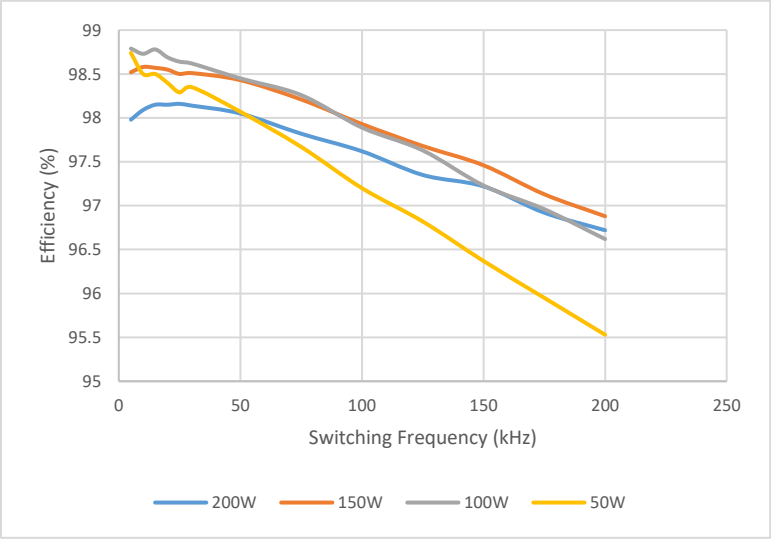

Figure 54: Efficiency versus switching frequency at different loads.

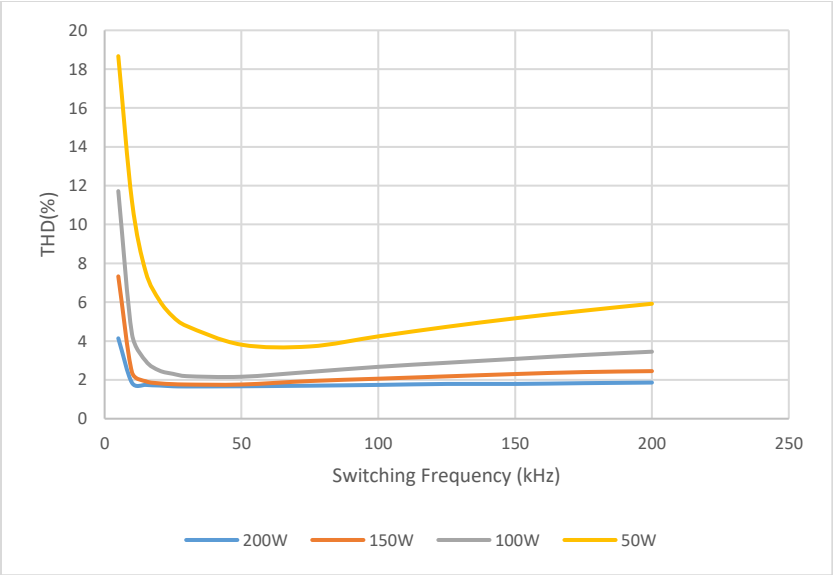

Figure 55: THD versus switching frequency at different loads.

Lastly, Figure 56 presents the results for optimal efficiency and THD values at each tested load obtained using the algorithm of dual tracking described in Figure 51 (Approach 1). The efficiency is maintained to maximum while the THD is limited to 4%. As for Approach 2 where the algorithm tracks the minimum THD point tracking (Figure 53), the results are presented in Figure 57. The THD is maintained to minimum (highest power quality) regardless of the efficiency.

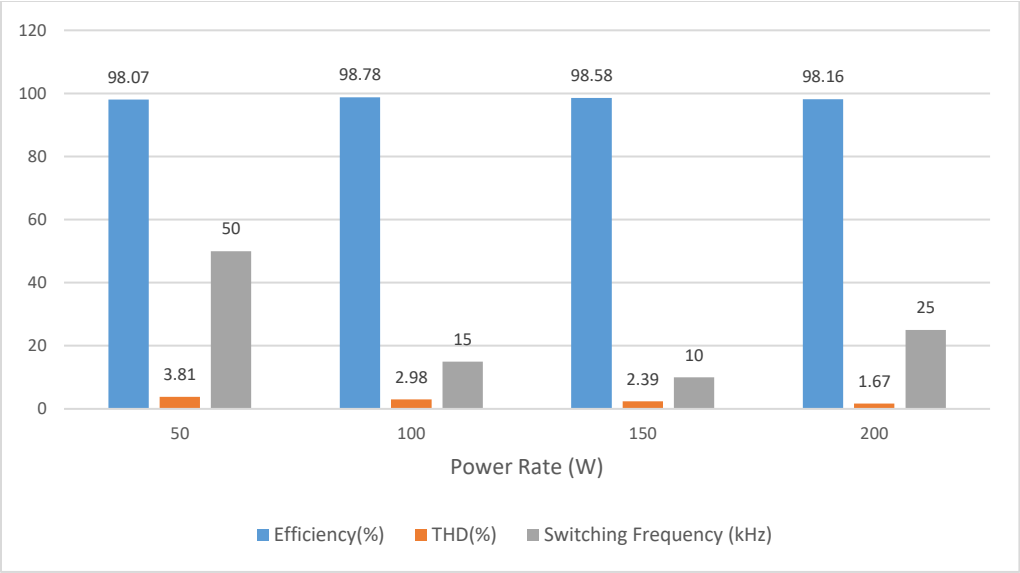

Figure 56: Optimum switching frequencies for maximum efficiency and THD below 4% (Approach 1).

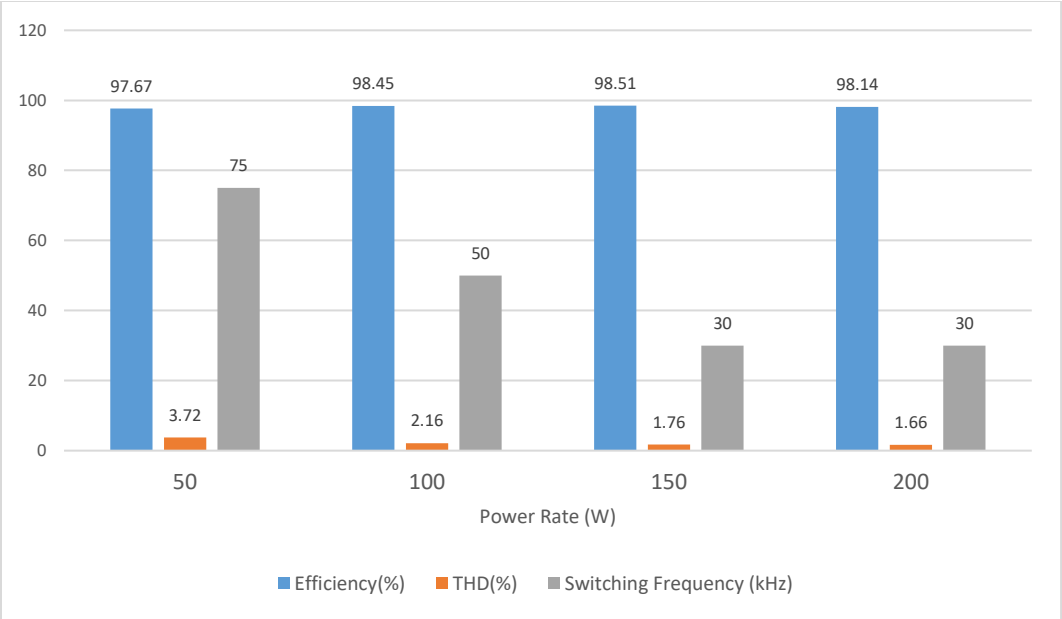

Figure 57: Optimum switching frequencies for highest power quality at minimum THD (Approach 2).

5.5 Conclusions

This chapter proposed two new algorithms to achieve dual optimization for an H-bridge SPWM microinverter by an optimal switching frequency tracking technique. the first is dual tracking of optimum efficiency and THD algorithm which tracks the optimal frequency for maximum efficiency under certain percentage of THD, while the second is THD point tracking algorithm which optimizes the power quality of the H-bridge microinverter by tracking the THD as a function of switching frequency to maintain its optimum value.

Using the proposed first technique (Approach 1), the power quality is improved by 60.1% for a 50 W load compared with a 20 kHz constant switching frequency inverter, while the efficiency is maintained above 98%. As for the second technique (Approach 2), the achieved power quality improvement is up to 63.9% compared to 20 kHz constant switching frequency inverter while the efficiency is maintained very close to 98%.

CHAPTER 6: SUMMARY AND FUTUTRE WORKS

6.1 Summary

Energy demand is increasing worldwide. In recent decades, researchers have focused on harvesting photovoltaic (PV) energy because it is a natural, clean, renewable source of power. Continuously decreasing costs have made this option even more desirable. However, several challenges still exist which limit its penetration into the grid. One challenge is the variable nature of solar irradiance levels due to such things as passing clouds and storms. These variances lead to fluctuations in the PV output power profile. This research proposes new approaches for smoothing the PV output and increasing its penetration into the grid. It does this by using a panel-level system, which interfaces with the PV, battery and grid. The system inversion stage is optimized by a switching frequency tracking technique.

Chapter 3 presents and explains the topology used for the PV-firming, the implemented controls regardless of the proposed algorithms, the static PV reference generation method, and the battery charging/discharging algorithm. The topology is two-stage power conversion (DC/DC converter (flyback) and DC/AC inverter (H-bridge)) micro-system, which integrates the battery as a third port by a direct connection to the DC-link. It has the ability to transferring the battery energy bidirectionally. Such controls must be implemented in this topology regardless of applying the proposed PV firming algorithms. The MPPT (Maximum Power Point Tracking) control, implemented in the DC/DC stage, ensures maximum power delivery by the PV. The phase locked

loop (PLL) control synchronizes the microinverter output with the grid waveforms. The DC-link voltage regulation control (DCVR) balances the DC/DC output power and the DC/AC input power, and sets the DC-link voltage. The output current regulation control (OCR) manages the output current of the DC/AC stage. PLL, DCVR, and OCR are implemented throughout the DC/AC stage. A static PV reference generation method is proposed for firming the output power of the PV micro-system. The static reference is based on real-time data collected for PV intermittency from two 300W PV modular systems including PV panels and a grid-tied microinverter located in a specific region in East Florida. The generated static PV reference is applied to an algorithm that controls the battery charge/discharge. The algorithm controls the output inverter current, which controls the battery current. However, while this algorithm of the battery charging/discharging control is being applied, the DC-link voltage regulation control (DCVR) is disabled, where the voltage across the DC-link is fixed and equal to the battery voltage. If the battery charging/discharging control is not applied, the battery will be disconnected and the DCVR is enabled. Simulation and experimental results are presented to validate the approach of the static PV firming algorithm. Finally, the storage capacity sizing for the system using the static PV firming algorithm is determined and analyzed. The determination of the usable storage capacity lies in calculating the average, maximum, and minimum energy for the PV. The surplus and deficient energy are compared to the static reference. This analysis shows that the average capacity of usable storage integrated to a 600W system is about 1.6kWh, where the nominal value is up to 3.2kWh. When PV energy is at a minimum (worst case), the usable storage capacity might reach to 3kWh (about 6kWh nominal value). This supports the need for the dynamic PV firming algorithm proposed in this research.

Chapter 4 discusses the most important contribution in this research, which is the dynamic PV firming algorithm. To dynamically firm the output profile of the PV micro-system, a novel algorithm is proposed to generate a dynamic PV reference power. Unlike conventional methods (e.g. moving average), this algorithm does not require that one-hour previous data of solar irradiance be calculated. In the proposed dynamic algorithm for PV firming, one smooth reference is saved in the memory of the microcontroller. It is the maximum PV reference curve ($P_{ref,max}$), and thus multiple power levels of PV reference are generated. The number of power levels is determined by the fluctuation factor (*ls*), where the number of power levels is equal to 1/ *ls*. The power levels are tracked and compared to the actual PV power ($P_{PV,act}$). Since there are no complicated equations and calculations, the processing and implementation is very quick. Furthermore, the ramp-rate of the actual PV power can be controlled from the abrupt changes by the value of the slew rate factor (σ_f). The relationship between the fluctuation factor (*ls*) or the number of power levels (1/*ls*), and battery sizing is also explored and discussed. The fluctuation factor has effects on the usable storage capacity ($E_{bat,cap}$), the surplus PV energy to be stored in the storage ($E_{PV,surplus}$), and the deficient PV energy ($E_{PV,deficient}$). Generally, the number of power levels is inversely proportional to the usable storage capacity ($E_{bat,cap}$), as well as the deficient PV energy ($E_{PV,deficient}$) even though it has a parabolic relation with the storage ($E_{PV,surplus}$). However, the number of power levels is directly proportional to the smoothness of the output PV profile. In other word, the fluctuation rate is decreased by increasing the fluctuation factor (*ls*). As a result, the *ls* makes a trade-off between the fluctuation rates and the storage capacity sizing. Once the dynamic PV reference is generated, another algorithm is used to control the battery current and its charging or discharging status. This is the same as for the static method

discussed in chapter 3. Similarly, for the DCVR scenarios, it is disabled while the charging/ discharging control is being applied and enabled when the battery is disconnected. The charging/ discharging control for the dynamic PV firming approach is verified in simulation and experimentally.

In chapter 5, two new approaches are proposed for optimizing an H-bridge SPWM microinverter for PV modular level application without any hardware modification. The author begins by creating a mathematical model for calculating the H-bridge losses. The results show that frequency changing has a nonlinear relationship with different power rate efficiencies. Meanwhile, the switching frequency makes trade-offs between the efficiency and the power quality. Implementing the calculation of the total harmonic distortions (THD) and efficiency is discussed in section 5.3.1. Using a tracking technique for an optimal switching frequency, dual optimization is achieved which includes power efficiency and THD as a power quality factor. The first approach is based on a tracking optimal switching frequency algorithm. It achieves dual optimization of maximum efficiency and under a certain percentage of THD. The second approach optimizes the power quality of the H-bridge microinverter using the proposed minimum THD point tracking algorithm which is a function of the switching frequency. Both techniques are verified experimentally. Under the first technique (Approach 1), the power quality for a 50 W load improved by 60.1% compared to using a constant switching frequency of 20kHz at over 98% efficiency. The second technique (Approach 2) achieved up to 63.9% improvement as compared to an inverter using a conventional constant switching frequency of 20 kHz, while the power efficiency is maintained around 98%.

6.2 Future Works

Unique approaches for designing and implementing PV-firming algorithms and microinverter power quality optimization were presented and studied analytically and experimentally in this dissertation. More research can be done to optimize: the presented three-port topology; the algorithms for the PV-firming and storage capacity sizing; and the approaches to the H-bridge SPWM microinverter power efficiency and quality.

For the proposed topology, the battery is interfaced throughout the DC-link which has the advantage of eliminating an additional stage for battery charging/ discharging conversion. However, in this situation, the battery voltage must be as high as the DC-link voltage, which is an uncommon voltage level for these types of applications. Furthermore, the DC/DC stage is a flyback topology which is still a transformer-based topology that need to be optimized for higher efficiency.

To further improve the performance of the PV-firming algorithms, several research points should be considered. In this dissertation, there are some high ramp-rate fluctuations which in some cases need to be filtered. Another research point is to find the optimal storage capacity based on the proposed PV-firming algorithm for this specific 200W panel-level system or even for different power level. For the battery charging/ discharging algorithm, an additional factor would be considered in order to have a balanced case for charging/ discharging. In other words, the energy consumed while the battery is being discharged should be equivalent to that energy acquired while the battery is being charged.

For the H-bridge SPWM microinverter optimization in this dissertation, every line period has fixed switching frequency and is tracked by two different algorithms. To further improve this technique of switching frequency tracking, the scheme should be changed to have variable switching frequency in every line period.

APPENDIX A: FSEC DATA SOURCE

A.1 What is FSEC?

Florida Solar Energy Center (FSEC) is a research institute of the University of Central Florida (UCF) for researching and developing energy technologies that enhance the economy and environment for the state of Florida and the nation. It was established in 1975 by the Florida Legislature. It serves officially as research institute of the state's energy. Several tasks that are done by the center; research conducting, solar systems testing and certifying, developing education programs for the public, students, and practitioners on the results of the research.

A.2 Data Collected for Modular PV System

FSEC has huge databases that collect data for several renewable energy technologies. One of the databases that is used for this dissertation is for modular Photovoltaic (PV) system.

Data is collected from two 310W (measured at 304 and 305W) PV panels connected to microinverters starting from Feb. 7th, 2016. The solar panels were in 5-degree tilt on roof. The measurement of the system output energy is by a 1-minute resolution continental controls wattnode power meter with pulse output (switch closure) using a calibration of 0.125 Wh/pulse. The channel for the output power in Watt (W) is calculated as output energy (Wh) multiplied by 60.

A.3 Case Study-Data from FSEC

In the following figures examples for data collected by FSEC on April 11th, 2016. First figure represents the PV energy measured as described in section A.2. The other figure is the PV power collected on same day, where the power is resulted in multiplying the energy by 60 seconds as explained in section A.2.

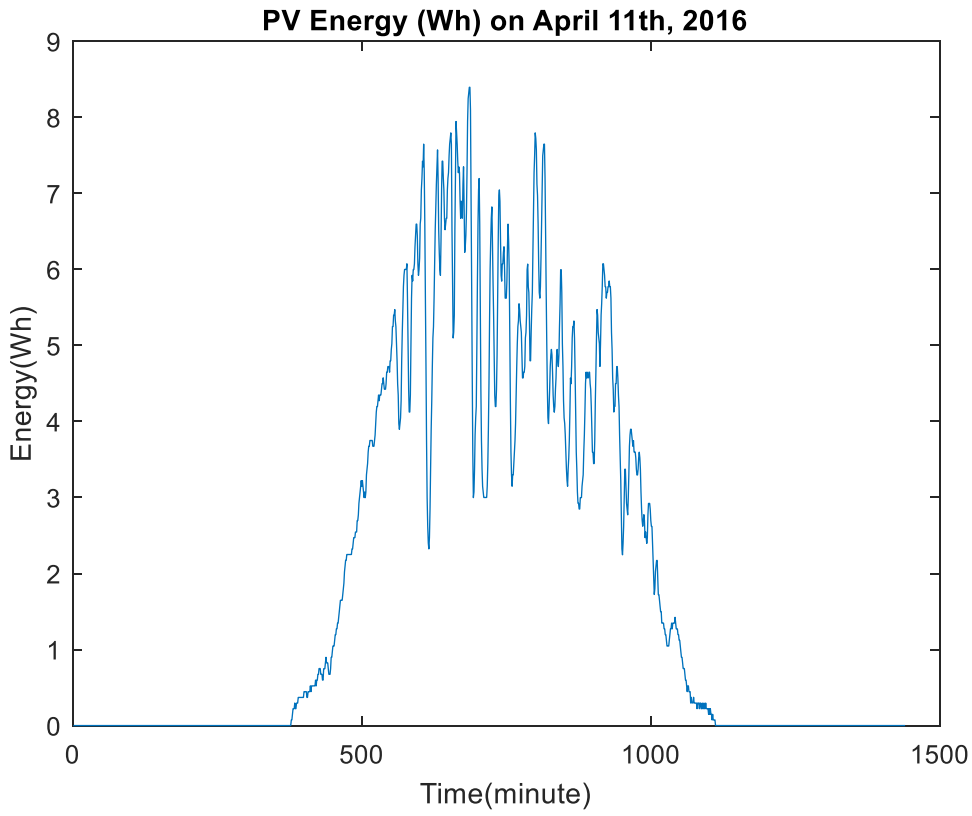

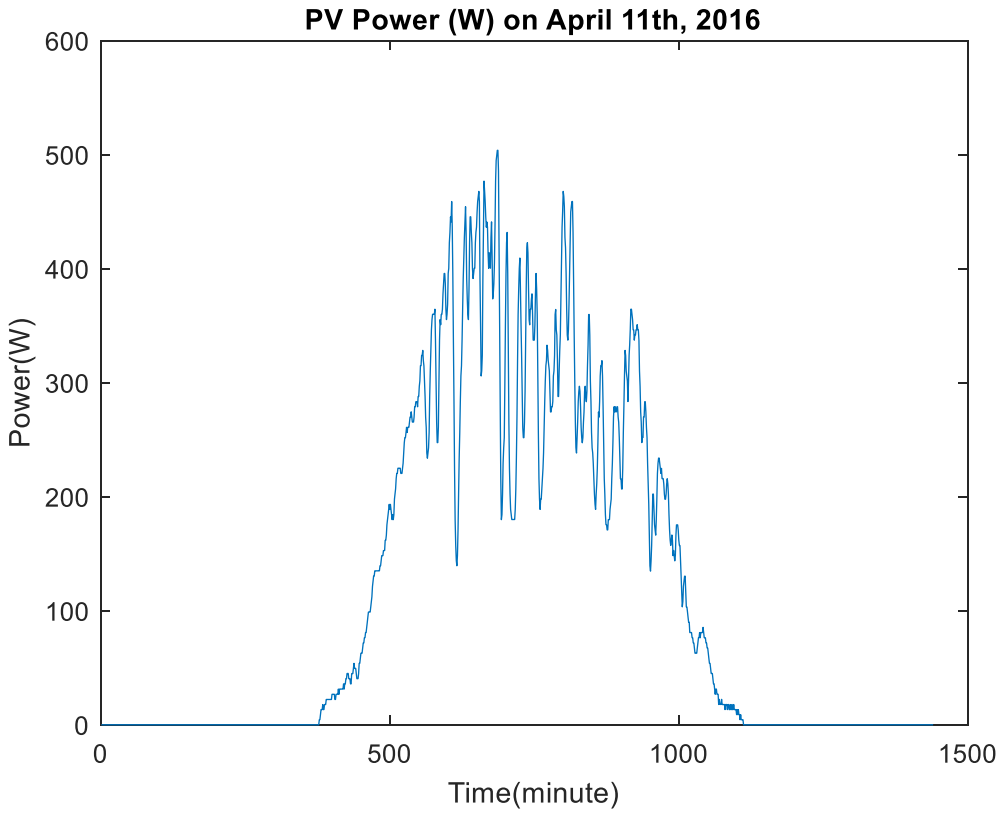
PV Power (W) on April 11th, 2016
600
500
400
300
200
100
0
Power(W)
0
500
1000
1500
Time(minute)

APPENDIX B: PV ENERGY PLOTS FOR TWELVE MONTHS

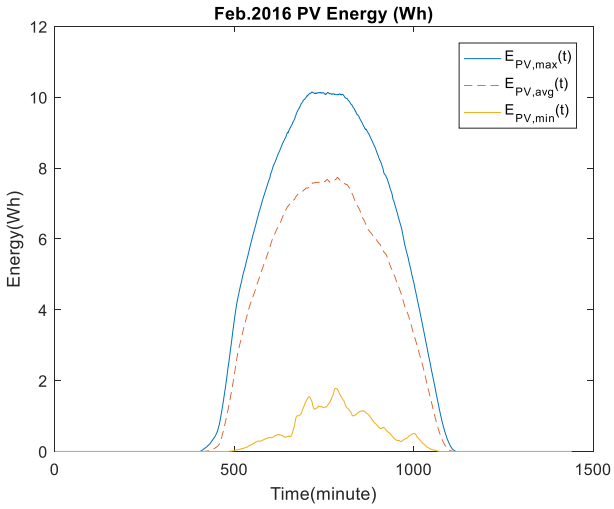
Feb.2016 PV Energy (Wh)
Energy(Wh)
Time(minute)
E_PV,max(t)
E_PV,avg(t)
E_PV,min(t)
0
2
4
6
8
10
12
0
500
1000
1500

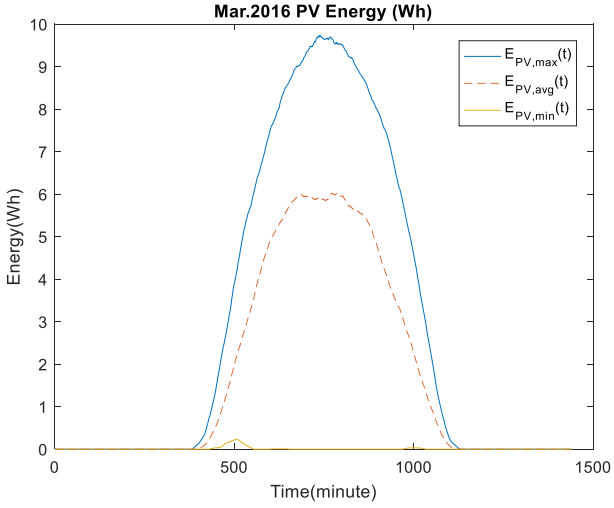
Mar.2016 PV Energy (Wh)
Energy(Wh)
Time(minute)
E_PV,max(t)
E_PV,avg(t)
E_PV,min(t)
0
1
2
3
4
5
6
7
8
9
10
0
500
1000
1500

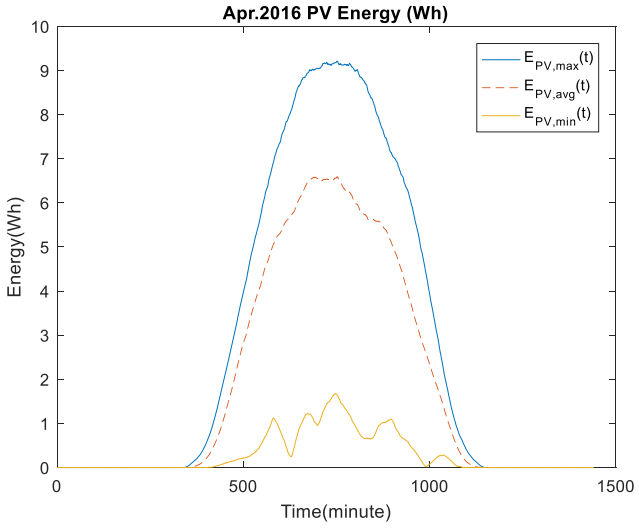
Apr.2016 PV Energy (Wh)
Energy(Wh)
Time(minute)
$E_{PV,max}(t)$
$E_{PV,avg}(t)$
$E_{PV,min}(t)$

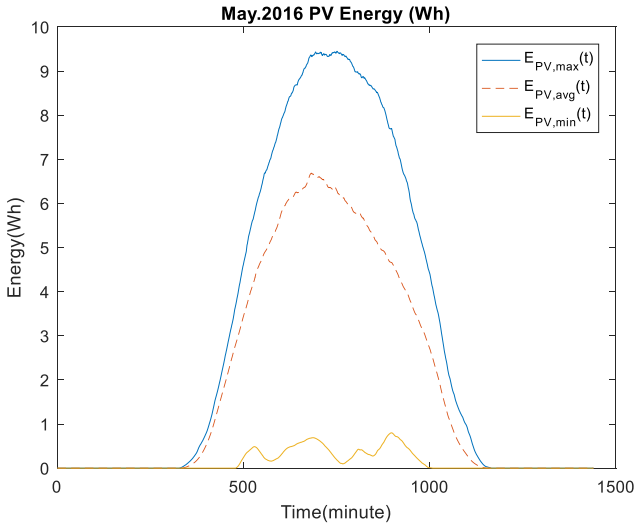
May.2016 PV Energy (Wh)
Energy(Wh)
Time(minute)
$E_{PV,max}(t)$
$E_{PV,avg}(t)$
$E_{PV,min}(t)$

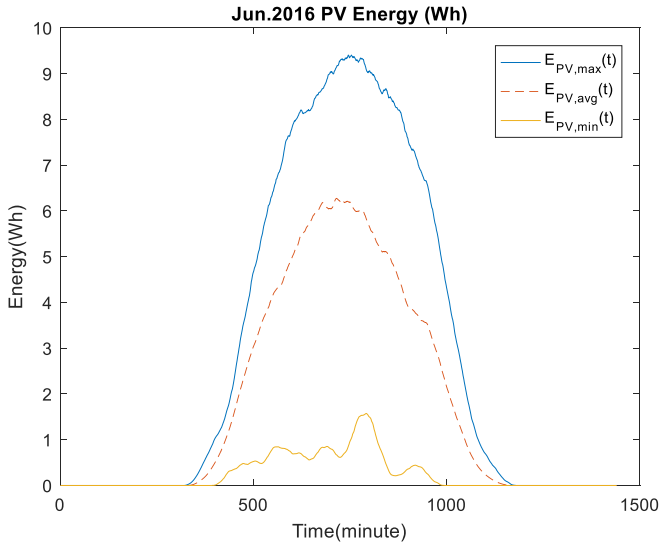
Jun.2016 PV Energy (Wh)
Energy(Wh)
Time(minute)
$E_{PV,max}(t)$
$E_{PV,avg}(t)$
$E_{PV,min}(t)$
0
1
2
3
4
5
6
7
8
9
10
0
500
1000
1500

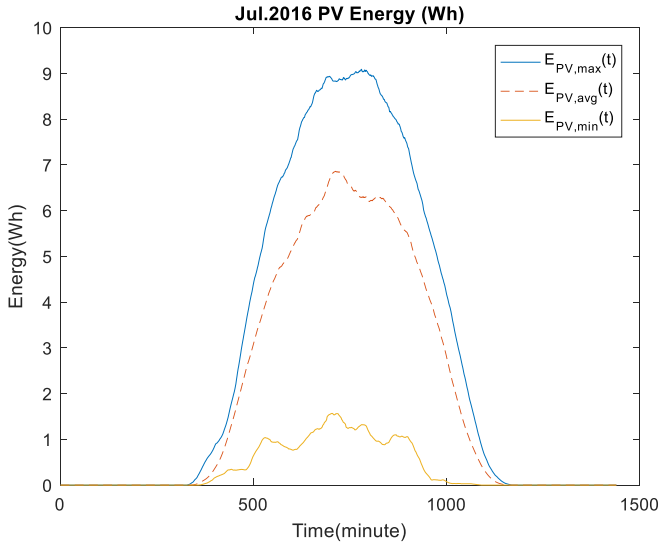
Jul.2016 PV Energy (Wh)
Energy(Wh)
Time(minute)
$E_{PV,max}(t)$
$E_{PV,avg}(t)$
$E_{PV,min}(t)$
0
1
2
3
4
5
6
7
8
9
10
0
500
1000
1500

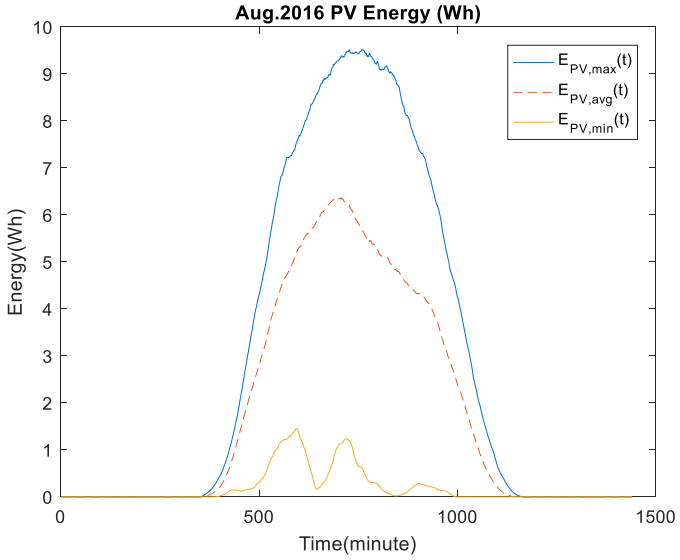
Aug.2016 PV Energy (Wh)
Energy(Wh)
Time(minute)
$E_{PV,max}(t)$
$E_{PV,avg}(t)$
$E_{PV,min}(t)$
0
1
2
3
4
5
6
7
8
9
10
0
500
1000
1500

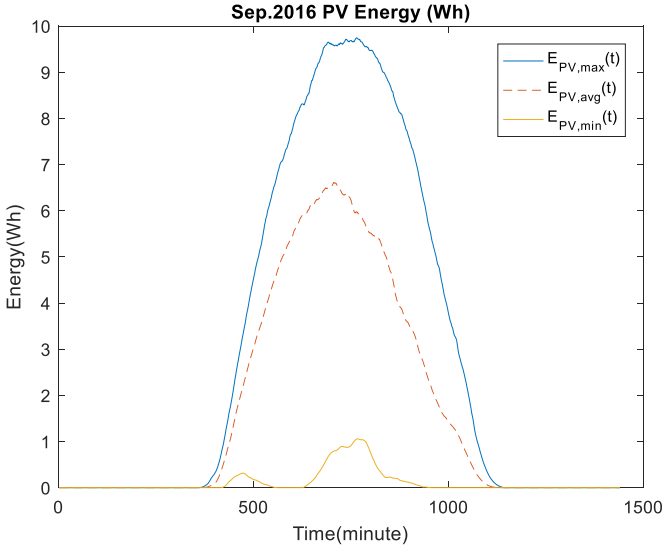
Sep.2016 PV Energy (Wh)
Energy(Wh)
Time(minute)
$E_{PV,max}(t)$
$E_{PV,avg}(t)$
$E_{PV,min}(t)$
0
1
2
3
4
5
6
7
8
9
10
0
500
1000
1500

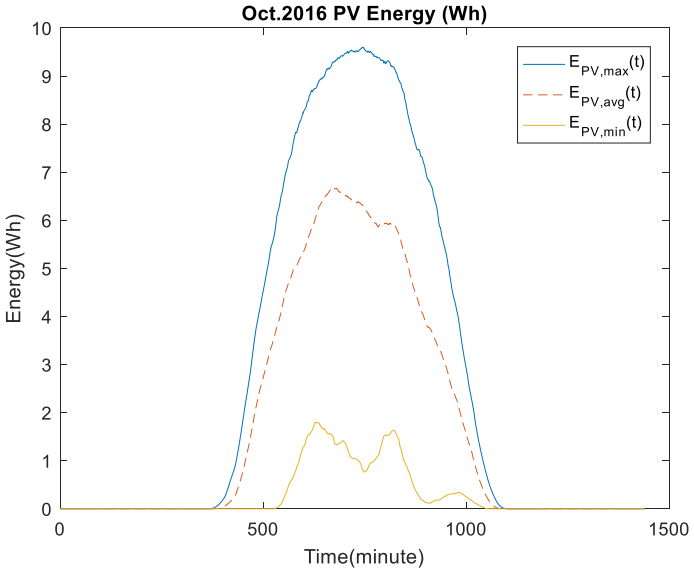
Oct.2016 PV Energy (Wh)
Energy(Wh)
Time(minute)
$E_{PV,max}(t)$
$E_{PV,avg}(t)$
$E_{PV,min}(t)$
0
1
2
3
4
5
6
7
8
9
10
0
500
1000
1500

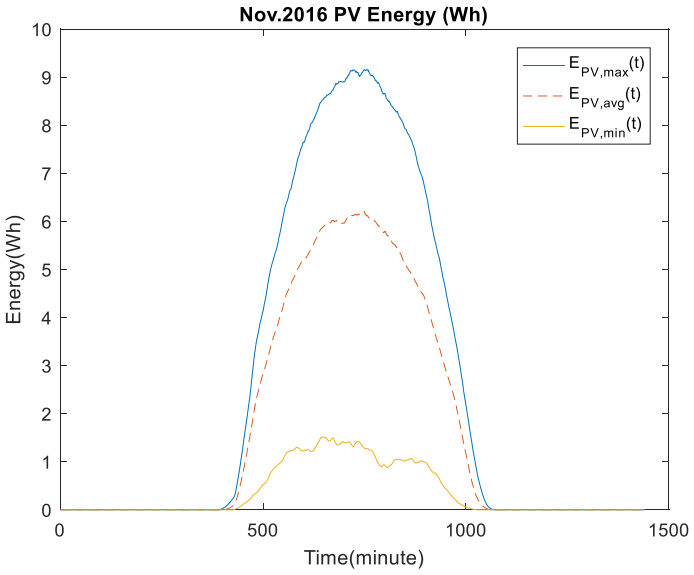
Nov.2016 PV Energy (Wh)
Energy(Wh)
Time(minute)
$E_{PV,max}(t)$
$E_{PV,avg}(t)$
$E_{PV,min}(t)$
0
1
2
3
4
5
6
7
8
9
10
0
500
1000
1500

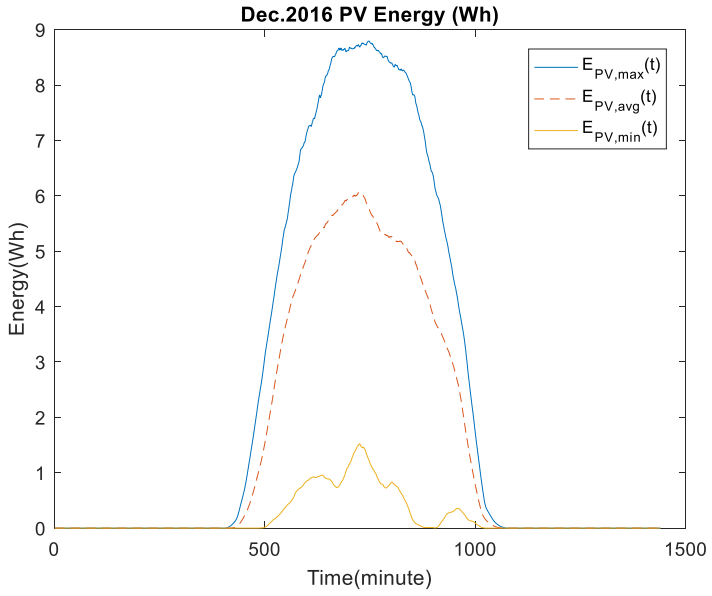
Dec.2016 PV Energy (Wh)
Energy(Wh)
Time(minute)
E_PV,max(t)
E_PV,avg(t)
E_PV,min(t)
0
1
2
3
4
5
6
7
8
9
0
500
1000
1500

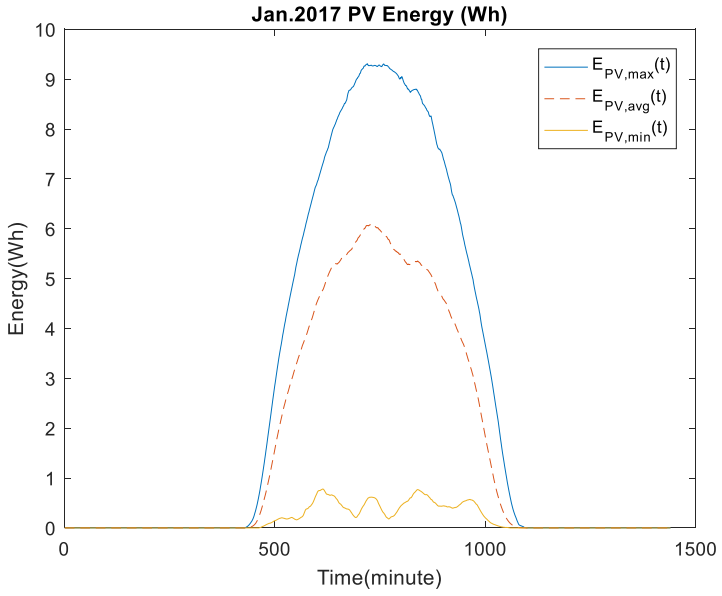
Jan.2017 PV Energy (Wh)
Energy(Wh)
Time(minute)
E_PV,max(t)
E_PV,avg(t)
E_PV,min(t)
0
1
2
3
4
5
6
7
8
9
10
0
500
1000
1500

APPENDIX C: EQUATIONS OF THE INVERTER POWER LOSSES

According to (35), represents the total instantaneous loss ($P_{loss_{total}}$) as a function of time, there are three types of losses, namely: inductor losses, conduction losses, and switching losses.

The inductor losses include DC and core losses, $P_{L_{DC}}$ and $P_{L_{core}}$, respectively, and are given in (45) and (48).

$$P_{L_{DC}}(t) = I_{L\_rms}^2 R_{L\_DC} \quad (50)$$

$$I_{L_{rms}}^2(t) = i_o^2(t) + \frac{\Delta i_{pp}^2}{12} \quad (51)$$

$$\Delta i_{pp}(t) = \frac{V_{BUS} T_s m_a \sin(\omega t)(1 - m_a \sin(\omega t))}{L_o} \quad (52)$$

where,

- R_{L_DC}: inductor DC resistance.
- Δi_{pp}: current ripple [79].
- $T_s = \frac{1}{f_s}$; switching period.
- f_s: switching frequency.
- $m_a = \frac{V_{o\_peak}}{V_{BUS}}$; modulation index [80].

$$P_{L\_core} = P_v V_e \quad (53)$$

$$P_v = \frac{C_m f_s^x B^y (C_{t2} T^2 - C_{t1} T + C_t)}{1000} \quad (54)$$

where

- P_v: core loss in mW/cm^3 as in [81][82].
- V_e: core effective volume [83].

The conduction losses are divided into two different modes. During mode 1, there are Q1, D3, and Q4 conduction losses, $P_{Q1_{con}}$, $P_{D3_{con}}$, and $P_{Q4_{con}}$, respectively, and are given in (50), (51), and (52). During mode 2, there are D2 and Q4' conduction losses, $P'_{D2_{con}}$ and $P_{Q4_{con}}$, respectively, and are given in (53) and (54).

$$P_{Q1_{con}}(t) = \frac{v_o(t)}{V_{BUS}} I_{L\_rms}^2 R_{Q1\_DSon} \quad (55)$$

$$P_{D3_{con}}(t) = \frac{v_o(t)}{V_{BUS}} (0.23 i_o(t) + 0.021 I_{L_{rms}}^2) \quad (56)$$

$$P_{Q4_{con}}(t) = P_{Q1_{con}}(t) \quad (57)$$

$$P'_{D2_{con}}(t) = \left(1 - \frac{v_o(t)}{V_{BUS}}\right) I_{L\_rms} V_{D2\_f} \quad (58)$$

$$P'_{Q4_{con}}(t) = \left(1 - \frac{v_o(t)}{V_{BUS}}\right) I_{L_{rms}}^2 R_{Q4_{DSon}} \quad (59)$$

where,

- P_{D3_con} is according to [84].
- $R_{Q1\_DSon} = R_{Q4\_DSon}$; drain to source on resistance [85].
- V_{D2_f}: forward voltage as in [86].

The switching losses are based on the MOSFETs [87], Q1 and Q4, which are $P_{Q1_{sw}}$ and $P_{Q4_{sw}}$, respectively, and given in (55) and (56).

$$P_{Q1_{sw}}(t) = 0.5 V_{BUS} i_o(t) f_s \left(t_{Q1\_LH} + t_{Q1\_HL}\right) \quad (60)$$

$$P_{Q4_{sw}}(t) = 0.5 V_{BUS} i_o(t) f \left(t_{Q4\_LH} + t_{Q4\_HL}\right) \quad (61)$$

where,

- t_{Q1_LH}/t_{Q4_LH}: pull-up switching time.
- t_{Q1_HL}/t_{Q4_HL}: pull-down switching time.

LIST OF REFERENCES

[1] NREL, "Geospatial Data Science; Solar Maps," *National Renewable Energy Laboratory (NREL)*. [Online]. Available: https://www.nrel.gov/gis/solar.html.

[2] "PV Intermittency Data," *Florida Solar Energy Center, University of Central Florida*. [Online]. Available: http://www.fsec.ucf.edu/en/.

[3] W. Jewell and R. Ramakumar, "The Effects of Moving Clouds on Electric Utilities with Dispersed Photovoltaic Generation," *IEEE Trans. Energy Convers.*, vol. EC-2, no. 4, pp. 570–576, 1987.

[4] E. C. Kern and E. M. Gulachenski, "Cloud Effects on Distributed Photovoltaic Generation: Slow Transients at the Gardner, Massachusetts Photovoltaic Experiment," *IEEE Trans. Energy Convers.*, vol. 4, no. 2, pp. 184–190, 1989.

[5] A. Woyte, V. Van Thong, R. Belmans, and J. Nijs, "Voltage fluctuations on distribution level introduced by photovoltaic systems," *IEEE Trans. Energy Convers.*, vol. 21, no. 1, pp. 202–209, 2006.

[6] D. L. Garrett and S. M. Jeter, "A Photovoltaic Voltage Regulation Impact Investigation Technique: Part I - Model Development," *IEEE Trans. Energy Convers.*, vol. 4, no. 1, pp. 47–53, 1989.

[7] S. A. Zabalawi, G. Mandic, and A. Nasiri, "Utilizing Energy Storage with PV for

Residential and Commercial Use," in *2008 34th Annual Conference of IEEE Industrial Electronics (IECON), Orlando, FL*, 2008, pp. 1045–1050.

[8] C. Trueblood *et al.*, "PV Measures Up for Fleet Duty: Data From A Tennessee Plant Are Used to Illustrate Metrics That Characterize Plant Performance," *IEEE Power Energy Mag.*, vol. 11, no. 2, pp. 33–44, 2013.

[9] M. J. E. Alam, K. M. Muttaqi, and D. Sutanto, "Mitigation of Rapid Voltage Variations Caused by Passing Clouds in Distribution Networks with Solar PV Using Energy Storage," in *8th International Conference on Electrical and Computer Engineering: Advancing Technology for a Better Tomorrow, ICECE 2014*, 2014, no. 1, pp. 305–308.

[10] J. Jolmson, B. Schenkman, A. Ellis, J. Quiroz, and C. Lenox, "Initial Operating Experience of the 1.2-MW La Ola Photovoltaic System," in *2012 IEEE 38th Photovoltaic Specialists Conference (PVSC) PART 2*, 2012, pp. 1–6.

[11] NREL, "1-Second Global Horizontal Irradiance, Oahu, Hawaii." [Online]. Available: https://midcdmz.nrel.gov/oahu_archive/.

[12] S. Abdollahy, A. Mammoli, F. Cheng, A. Ellis, and J. Johnson, "Distributed Compensation of A Large Intermittent Energy Resource in A Distribution Feeder," in *2013 IEEE PES Innovative Smart Grid Technologies Conference, ISGT 2013*, 2013, pp. 1–6.

[13] D. Sayeef, Saad; Heslop, Simon; Cornforth, David; Moore, Tim; Percy, Steven; Ward, John;

Berry, Adam; Rowe, “Solar intermittency: Australia’s clean energy challenge. Characterising the effect of high penetration solar intermittency on Australian electricity networks,” CSIRO, Newcastle, 2012.

[14] H. Sugihara, K. Yokoyama, O. Saeki, K. Tsuji, and T. Funaki, “Economic and Efficient Voltage Management Using Customer-Owned Energy Storage Systems in A Distribution Network with High Penetration of Photovoltaic Systems,” *IEEE Trans. Power Syst.*, vol. 28, no. 1, pp. 102–111, 2013.

[15] L. Bird, M. Milligan, D. Lew, L. Bird, M. Milligan, and D. Lew, “Integrating Variable Renewable Energy : Challenges and Solutions Integrating Variable Renewable Energy : Challenges and Solutions,” *National Renewable Energy Laboratory (NREL)*, 2013.

[16] L. Chang, W. Zhang, S. Xu, and K. Spence, “Review on Distributed Energy Storage Systems for Utility Applications,” *CPSS Trans. POWER Electron. Appl.*, vol. 2, no. 4, pp. 267–276, 2017.

[17] H. Chen, T. Ngoc, W. Yang, C. Tan, and Y. Li, “Progress in electrical energy storage system : A critical review,” *Prog. Nat. Sci.*, vol. 19, no. 3, pp. 291–312, 2009.

[18] and A. S. D. O. M. Toledo, D. O. Filho, “Distributed photovoltaic generation and energy storage systems: A review,” *Renew. Sustain. Energy Rev.*, vol. 14, no. 1, pp. 506–511, 2010.

[19] S. Vazquez, S. M. Lukic, E. Galvan, L. G. Franquelo, and J. M. Carrasco, “Energy Storage

Systems for Transport and Grid Applications," *IEEE Trans. Ind. Electron.*, vol. 57, no. 12, pp. 3881–3895, 2010.

[20] H. Zhao, Q. Wu, S. Hu, H. Xu, and C. N. Rasmussen, "Review of energy storage system for wind power integration support," *Appl. Energy*, vol. 137, no. 1, pp. 545–553, 2015.

[21] M. Yilmaz and P. T. Krein, "Review of Battery Charger Topologies , Charging Power Levels , and Infrastructure for Plug-In Electric and Hybrid Vehicles," *IEEE Trans. Power Electron.*, vol. 28, no. 5, pp. 2151–2169, 2013.

[22] W. Choi *et al.*, "Reviews on Grid-Connected Inverter , Utility-Scaled Battery Energy Storage System , and Vehicle-to-Grid Application – Challenges and Opportunities," in *2017 IEEE Transportation Electrification Conference and Expo (ITEC)*, 2017, pp. 203–210.

[23] X. Luo, J. Wang, M. Dooner, and J. Clarke, "Overview of current development in electrical energy storage technologies and the application potential in power system operation," *Appl. Energy*, vol. 137, no. 1, pp. 511–536, 2015.

[24] D. O. Akinyele and R. K. Rayudu, "Review of energy storage technologies for sustainable power networks," *Sustain. Energy Technol. Assessments*, vol. 8, no. 12, pp. 74–91, 2014.

[25] E. Barbour, I. G. Wilson, J. Radeliffe, Y. Ding, and Y. Li, "A review of pumped hydro energy storage development in significant international electricity markets," *Renew. Sustain. Energy Rev.*, vol. 61, no. 8, pp. 421–432, 2016.

[26] S. Briola, P. D. Marco, R. Gabbrielli, and J. Riccardi, “A novel mathematical model for the performance assessment of diabatic compressed air energy storage systems including the turbomachinery characteristic curves,” *Appl. Energy*, vol. 178, no. 9, pp. 758–772, 2016.

[27] S. F. Tie and C. W. Tan, “A review of energy sources and energy management system in electric vehicles,” *Renew. Sustain. Energy Rev.*, vol. 20, no. 4, pp. 82–102, 2013.

[28] M. J. E. Alam, K. M. Muttaqi, and D. Sutanto, “Mitigation of Rooftop Solar PV Impacts and Evening Peak Support by Managing Available Capacity of Distributed Energy Storage Systems,” *IEEE Trans. Power Syst.*, vol. 28, no. 4, pp. 3874–3884, 2013.

[29] M. Bortolini, M. Gamberi, and A. Graziani, “Technical and Economic Design of Photovoltaic and Battery Energy Storage System,” *Energy Convers. Manag.*, vol. 86, pp. 81–92, 2014.

[30] X. Han, T. Ji, Z. Zhao, and H. Zhang, “Economic Evaluation of Batteries Planning in Energy Storage Power Stations for Load Shifting,” *Renew. Energy*, vol. 78, pp. 643–647, 2015.

[31] Y. Zhang, A. Lundblad, P. E. Campana, and J. Yan, “Employing Battery Storage to Increase Photovoltaic Self-sufficiency in a Residential Building of Sweden,” *Energy Procedia*, vol. 88, pp. 455–461, 2016.

[32] V. Fthenakis, J. E. Mason, and K. Zweibel, “The technical , geographical , and economic feasibility for solar energy to supply the energy needs of the US,” *Energy Policy*, vol. 37,

pp. 387–399, 2009.

[33] F. Cucchiella, I. D. Adamo, and M. Gastaldi, “Photovoltaic Energy Systems with Battery Storage for Residential Areas : An Economic Analysis International Panel on Climate Change,” *J. Clean. Prod.*, vol. 131, pp. 460–474, 2016.

[34] A. A. Solomon, D. Faiman, and G. Meron, “Appropriate Storage for High-Penetration Grid-Connected Photovoltaic Plants,” *Energy Policy*, vol. 40, no. 1, pp. 335–344, 2012.

[35] D. Hart and A. Sarkissian, “Deployment of Grid-Scale Batteries in the United States,” 2016.

[36] T. D. Hund, S. Gonzalez, and K. Barrett, “Grid-Tied PV System Energy Smoothing,” in *2010 35th IEEE Photovoltaic Specialists Conference*, 2010, pp. 002762–002766.

[37] J. Traube *et al.*, “Mitigation of Solar Irradiance Intermittency in Photovoltaic Power Systems with Integrated Electric-Vehicle Charging Functionality,” *IEEE Trans. Power Electron.*, vol. 28, no. 6, pp. 3058–3067, 2013.

[38] S. Rahman and K. S. S. Tam, “A Feasibility Study of Photovoltaic Fuel Cell Hybrid Energy System,” *IEEE Trans. Energy Convers.*, vol. 3, no. 1, pp. 50–55, 1988.

[39] K. S. Tam, P. Kumar, and M. Foreman, “Enhancing the Utilization of Photovoltaic Power Generation by Superconductive Magnetic Energy Storage,” *IEEE Trans. Energy Convers.*, vol. 4, no. 3, pp. 314–321, 1989.

[40] N. Kakimoto, H. Satoh, S. Takayama, and K. Nakamura, “Ramp-rate control of photovoltaic generator with electric double-layer capacitor,” *IEEE Trans. Energy Convers.*, vol. 24, no. 2, pp. 465–473, 2009.

[41] T. Monai, I. Takano, H. Nishikawa, and Y. Sawada, “A Collaborative Operation Method Between New Energy-Type Dispersed Power Supply and EDLC,” *IEEE Trans. Energy Convers.*, vol. 19, no. 3, pp. 590–598, 2004.

[42] X. Li, D. Hui, and X. Lai, “Battery Energy Storage Station (BESS)-Based Smoothing Control of Photovoltaic (PV) and Wind Power Generation Fluctuations,” *IEEE Trans. Sustain. Energy*, vol. 4, no. 2, pp. 464–473, 2013.

[43] M. J. E. Alam, S. Member, K. M. Muttaqi, S. Member, D. Sutanto, and S. Member, “A Novel Approach for Ramp-Rate Control of Solar PV Using Energy Storage to Mitigate Output Fluctuations Caused by Cloud Passing,” *IEEE Trans. Energy Convers.*, vol. 29, no. 2, pp. 507–518, 2014.

[44] S. Abdelrazek and S. Kamalasadan, “A Weather-Based Optimal Storage Management Algorithm for PV Capacity Firming,” *IEEE Trans. Ind. Appl.*, vol. 52, no. 6, pp. 5175–5184, 2016.

[45] S. A. S. Kamalasadan, “Integrated PV Capacity Firming and Energy Time Shift Battery Energy Storage Management Using Energy Oriented Optimization,” *IEEE Trans. Ind. Appl.*, vol. PP, no. 99, p. 1, 2016.

[46] S. G. Tesfahunegn, Ø. Ulleberg, P. J. S. Vie, and T. M. Undeland, "Energy Procedia PV Fluctuation Balancing Using Hydrogen Storage — a Smoothing Method for Integration of PV Generation into the Utility Grid," *Energy Procedia*, vol. 12, no. 1876, pp. 1015–1022, 2011.

[47] G. Buticchi, D. Barater, S. Member, E. Lorenzani, C. Concari, and G. Franceschini, "A Nine-Level Grid-Connected Converter Topology for Single-Phase Transformerless PV Systems," *IEEE Trans. Ind. Electron.*, vol. 61, no. 8, pp. 3951–3960, 2014.

[48] M. Chithra and S. G. B. Dasan, "Analysis of Cascaded H Bridge Multilevel Inverters with Photovoltaic Arrays," in *2011 International Conference on Emerging Trends in Electrical and Computer Technology*, 2011, pp. 442–447.

[49] D. Sun, B. Ge, W. Liang, H. Abu-rub, and S. Member, "An Energy Stored Quasi-Z-Source Cascade Multilevel Inverter-Based Photovoltaic," *IEEE Trans. Ind. Electron.*, vol. 62, no. 9, pp. 5458–5467, 2015.

[50] G. R. Walker and P. C. Sernia, "Cascaded DC – DC Converter Connection of Photovoltaic Modules," *IEEE Trans. Power Electron.*, vol. 19, no. 4, pp. 1130–1139, 2004.

[51] Y. Zhou, L. Liu, and H. Li, "A High-Performance Photovoltaic Module-Integrated Converter (MIC) Based on Cascaded Quasi-Z-Source," *IEEE Trans. Power Electron.*, vol. 28, no. 6, pp. 2727–2738, 2013.

[52] W. Jiang and B. Fahimi, “Multi-port Power Electric Interface for renewable energy sources,” *Conf. Proc. - IEEE Appl. Power Electron. Conf. Expo. - APEC*, pp. 347–352, 2009.

[53] M. McDonough, “Integration of Inductively Coupled Power Transfer and Hybrid Energy Storage System: A Multiport Power Electronics Interface for Battery-Powered Electric Vehicles,” *IEEE Trans. Power Electron.*, vol. 30, no. 11, pp. 6423–6433, 2015.

[54] Z. Qian, O. Abdel-Rahman, H. Hu, and I. Batarseh, “An Integrated Three-Port Inverter for Stand-Alone PV Applications,” *2010 IEEE Energy Convers. Congr. Expo. ECCE 2010 - Proc.*, pp. 1471–1478, 2010.

[55] M. Amirabadi, H. A. Toliyat, and W. C. Alexander, “A Multiport AC Link PV Inverter with Reduced Size and Weight for Stand-Alone Application,” *IEEE Trans. Ind. Appl.*, vol. 49, no. 5, pp. 2217–2228, 2013.

[56] H. Hu, S. Harb, N. H. Kutkut, Z. J. Shen, and I. Batarseh, “A Single-Stage Microinverter Without Using Eletrolytic Capacitors,” *IEEE Trans. Power Electron.*, vol. 28, no. 6, pp. 2677–2687, 2013.

[57] T. Shimizu, K. Wada, and N. Nakamura, “A Flyback-Type Single Phase Utility Interactive Inverter with Low-Frequency Ripple Current Reduction on the DC Input for an AC Photovoltaic Module System,” *2002 IEEE 33rd Annu. IEEE Power Electron. Spec. Conf. Proc. (Cat. No.02CH37289)*, vol. 3, no. 5, pp. 1483–1488, 2002.

[58] J. Zeng, W. Qiao, C. Wei, and L. Qu, “A Soft-Switched Three-Port Single-Stage Inverter for Photovoltaic-Battery Systems,” *2015 IEEE Energy Convers. Congr. Expo. ECCE 2015*, pp. 4568–4573, 2015.

[59] S. B. Kjær, *Design and Control of an Inverter for Photovoltaic Applications*. Institut for Energiteknik, Aalborg Universitet, 2005.

[60] “PV Intermittency Data,” *Florida Solar Energy Center, University of Central Florida*. .

[61] S. B. Kjaer, J. K. Pedersen, and F. Blaabjerg, “A Review of Single-Phase Grid-Connected Inverters for Photovoltaic Modules,” *IEEE Trans. Ind. Appl.*, vol. 41, no. 5, pp. 1292–1306, 2005.

[62] Q. Li and P. Wolfs, “A Review of the Single Phase Photovoltaic Module Integrated Converter Topologies with Three Different DC Link Configurations,” *IEEE Trans. Power Electron.*, vol. 23, no. 3, pp. 1320–1333, 2008.

[63] Y. Chen, S. Member, Y. Liu, S. Hung, and C. Cheng, “Multi-Input Inverter for Grid-Connected Hybrid PV / Wind Power System,” *IEEE Trans. Power Electron.*, vol. 22, no. 3, pp. 1070–1077, 2007.

[64] N. Vázquez, J. Villegas-saucillo, C. Hernández, E. Rodríguez, and J. Arau, “Two-Stage Uninterruptible Power Supply With High Power Factor,” *IEEE Trans. Ind. Appl.*, vol. 55, no. 8, pp. 2954–2962, 2008.

[65] K. Thiyagarajah, V. T. Ranganathan, and B. S. Ramakrishna Iyengar, “A High Switching Frequency IGBT PWM Rectifier/Inverter System for AC Motor Drives Operating from Single Phase Supply,” *IEEE Trans. Power Electron.*, vol. 6, no. 4, pp. 576–584, 1991.

[66] S. Vaez-Zadeh and S. R. Harooni, “Decoupling Vector Control of Single Phase Induction Motor Drives,” *IEEE 36th Conf. Power Electron. Spec. 2005.*, no. 1, pp. 733–738, 2005.

[67] B. Singh, K. Al-Haddad, and A. Chandra, “A Review of Active Filters for Power Quality Improvement,” *IEEE Trans. Ind. Electron.*, vol. 46, no. 5, pp. 960–971, 1999.

[68] IEEE, *IEEE Recommended Practice for Utility Interface of Photovoltaic (PV) Systems*, vol. 2000. 2000.

[69] IEEE Std 1547-2008 (R2008), “IEEE Standard for Interconnecting Distributed Resources with Electric Power Systems Amendment,” *IEEE Stand.*, vol. 2014, pp. 1–16, 2008.

[70] M. Bhardwaj, “Voltage Source Inverter Reference Design,” *Texas Instruments Incorporated*, 2017. [Online]. Available: http://www.ti.com/lit/ug/tiduay6c/tiduay6c.pdf.

[71] N. Mohan, T. M. Undeland, and W. P. Robbins, *Power Electronics: Converters, Applications and Design, 1995*. John Wiley & Sons, 1997.

[72] H. Mao, X. Yang, Z. Chen, and Z. Wang, “A Hysteresis Current Controller for Single-Phase Three-Level Voltage Source Inverters,” *IEEE Trans. Power Electron.*, vol. 27, no. 7, pp. 3330–3339, 2012.

[73] X. Mao, R. Ayyanar, and H. K. Krishnamurthy, “Optimal Variable Switching Frequency Scheme for Reducing Switching Loss in Single-Phase Inverters Based on Time-Domain Ripple Analysis,” *IEEE Trans. Power Electron.*, vol. 24, no. 4, pp. 991–1001, 2009.

[74] L. Wei and R. A. Lukazewski, “Pulse Width Modulation (PWM) Rectifier with Variable Switching Frequency,” *US Pat. no. US007190143B2*, 2007.

[75] A. A. Hussein, A. A. Fardoun, and S. S. Stephen, “An Ultrafast Maximum Power Point Tracking Technique for Optimal Battery Charging,” *IEEE Trans. Sustain. Energy*, vol. 8, no. 3, pp. 1321–1329, 2017.

[76] A. A. Hussein, A. A. Fardoun, and S. S. Stephen, “An Online Frequency Tracking Algorithm Using Terminal Voltage Spectroscopy for Battery Optimal Charging,” *IEEE Trans. Sustain. Energy*, vol. 7, no. 1, pp. 32–40, 2016.

[77] J. A. Abu-Qahouq, W. Al-Hoor, W. Mikhael, L. Huang, and I. Batarseh, “Analysis and Design of An Adaptive-Step-Size Digital Controller for Switching Frequency Autotuning,” *IEEE Trans. Circuits Syst. I Regul. Pap.*, vol. 56, no. 12, pp. 2749–2759, 2009.

[78] Microchip Technology Inc., “3-Phase Energy Meter Reference Design,” 2009. [Online]. Available: http://ww1.microchip.com/downloads/en/DeviceDoc/51723a.pdf.

[79] M. Bhardwaj, “TI Designs: TIDM-HV-1PH-DCAC; Voltage Source Inverter Design Guide,” *Texas Instruments Incorporated*, 2017. [Online]. Available:

http://www.ti.com/tool/TIDM-HV-1PH-DCAC.

[80] N. Mohan and T. M. Undeland, *Power Electronics: Converters, Applications, and Design 3rd Edition*, 3rd ed. John Wiley & Sons, 2007.

[81] Ferroxcube, "FXC Power Loss Coefficients," *FERROXCUBE A YAGEO COMPANY*. [Online]. Available: https://www.ferroxcube.com/.

[82] Ferroxcube, "Data sheet 3C81 Material specification," *FERROXCUBE A YAGEO COMPANY*, 2008. [Online]. Available: http://ferroxcube.home.pl/prod/assets/u672714.pdf.

[83] Ferroxcube, "FERROXCUBE P42/29, datasheet," *FERROXCUBE A YAGEO COMPANY*, 2008. [Online]. Available: http://ferroxcube.home.pl/prod/assets/p4229.pdf.

[84] STMicroelectronics, "STPS8L30 Low drop power Schottky rectifier, Datasheet - production data," *STMicroelectronics*, 2016. [Online]. Available: http://www.st.com/en/diodes-and-rectifiers/stps8l30.html.

[85] Fairchild Semiconductor Corporation, "FDB28N30 N-Channel MOSFET," *Fairchild Semiconductor Corporation*, 2007. [Online]. Available: 8 www.fairchildsemi.com.

[86] I. Cree, "C3D06060G Silicon Carbide Schottky Diode Z-Rec® Rectifier," *Cree, Inc.*, 2016. [Online]. Available: www.cree.com/power.

[87] Fairchild Semiconductor Corporation, "AN-6005 Synchronous buck MOSFET loss

calculations with Excel model," *Fairchild Semiconductor Corporation*, 2014. [Online]. Available: www.fairchildsemi.com.